

RUNX2 Inhibition Disrupts a PAX3::FOXO1-RUNX2 Feed-Forward Loop and Dismantles
Oncogenic Gene Programs in Fusion-Positive Rhabdomyosarcoma

by

Elizabeth Almerinda Mendes

Department of Pharmacology and Cancer Biology
Duke University

Defense Date: September 24, 2025

Approved:

Corinne M Linardic, Advisor

Kris C Wood, Chair

Angela N Koehler

Ann Marie Pendergast

Yarui Diao

Dissertation submitted in partial fulfillment of the requirements for the degree of Doctor
of Philosophy in the Department of Pharmacology & Cancer Biology in The Graduate School of
Duke University
2025

ABSTRACT

RUNX2 Inhibition Disrupts a PAX3::FOXO1-RUNX2 Feed-Forward Loop and Dismantles
Oncogenic Gene Programs in Fusion-Positive Rhabdomyosarcoma

by

Elizabeth Almerinda Mendes

Department of Pharmacology and Cancer Biology
Duke University

Defense Date: September 24, 2025

Approved:

Corinne M Linardic, Advisor

Kris C Wood, Chair

Angela N Koehler

Ann Marie Pendergast

Yarui Diao

An abstract of a dissertation submitted in partial fulfillment of the requirements for the degree of
Doctor of Philosophy in the Department of Pharmacology and Cancer Biology in The Graduate
School of
Duke University
2025

Copyright by
Elizabeth Almerinda Mendes
2025

Abstract

Globally, hundreds of thousands of children will develop cancer each year, and in the United States, childhood cancer is the leading cause of death by disease. Despite decades of research and the development of cures in specific cancer subtypes, others such as soft tissue sarcomas rely on standard chemotherapy regimens that date back to the mid-twentieth century. Current World Health Organization criteria subclassify childhood sarcomas by histopathologic and molecular features to determine cancer grade and design treatment regimens. Some bone and soft tissue sarcomas are characterized by the presence of a signature transcription-factor based fusion oncogene which is not currently druggable. Alternatively, other non-fusion-driven sarcomas are characterized by the presence or absence of point mutations, many of which have led to the development of novel therapies for children. To identify novel druggable proteins in fusion-driven sarcomas, we must rigorously characterize patient tumors and cell lines to better understand the relationship between fusion drivers and the genomes that they govern.

Rhabdomyosarcoma (RMS) is the most common soft tissue sarcoma of childhood and adolescence, characterized by the expression of skeletal muscle markers. RMS is subclassified into four types based on histopathologic features: embryonal RMS (ERMS), alveolar RMS (ARMS), spindle cell/sclerosing RMS (SCRMS), and pleomorphic RMS (PRMS). ERMS and ARMS are the most common, and now classified molecularly based on the absence (fusion-negative RMS; FN-RMS) or the presence (fusion-positive RMS; FP-RMS) of the *PAX3/7::FOXO1* fusion oncogene. FP-RMS represents a disproportionately high percentage of high-risk RMS cases. Despite its role as an oncogenic driver, the PAX3::FOXO1 oncoprotein is refractory to therapeutic targeting due to its lack of catalytic activity, and its intrinsically disordered structure, which leaves few pockets to bind small molecules. However, the network of transcriptional programs driven by PAX3::FOXO1 may yield alternate therapeutic targets. In this study, we take a broad view of RMS and FP-RMS to nominate additional members of this

network that may be more amenable to clinical targeting. We identify a PAX3::FOXO1 feed-forward loop whereby RUNX2 and PAX3::FOXO1 reciprocally regulate one another to drive transcription of downstream PAX3::FOXO1 targets, indicating that RUNX2 is a promising FP-RMS therapeutic target.

Using messenger (mRNA) sequencing data of primary patient tumor tissue, we compared the four histopathologic types of RMS. With the DepMap resource we prioritized the transcription factors participating in this network. At the top of our list emerged RUNX2, a transcription factor previously identified as a PAX3::FOXO1 downstream target and part of the PAX3::FOXO1 interactome, but which has not been evaluated as a therapeutic target in FP-RMS. We investigated the phenotypic consequences of RUNX2 inhibition in FP-RMS, the mechanism by which RUNX2 promotes downstream PAX3::FOXO1 signaling, and evaluated the consequences of RUNX2 inhibition *in vivo*. Using both genetic and pharmacological inhibition of RUNX2 *in vitro* and *in vivo*, we found that RUNX2 is essential to maintaining a proliferative FP-RMS cell state, while preventing apoptosis and terminal myogenic differentiation.

Using chromatin immunoprecipitation (ChIP) sequencing data whereby *PAX3::FOXO1* was inhibited with RNAi, we found that PAX3::FOXO1 binds a *RUNX2* enhancer to upregulate gene expression alongside MYOD1 and p300. Follow-up RNAi experiments inhibiting *RUNX2* expression followed by mRNA sequencing and protein-based studies found that RUNX2 supports the expression of PAX3::FOXO1-associated enhancer networks, myogenic signatures, and PAX3::FOXO1 itself at the mRNA and protein level.

In summary, our findings suggest that directly inhibiting RUNX2 phenocopies PAX3::FOXO1 suppression and highlight its role as a legitimate druggable driver of oncogenic phenotypes in FP-RMS. Future studies to degrade RUNX2 protein paired with HiBiT drug screening will identify additional compounds capable of eliminating this newly characterized FP-RMS driver.

Dedication

This work is dedicated to my mother, Michelle Suzanne Day, who selflessly cared for me and my siblings and propelled us out of poverty and into a brighter future. She fearlessly fought two battles with cancer, but on December 29, 2023, with her hand in mine, she took her last breath.

In one of our final text messages on December 17, 2023, I told my mother that I loved her more than she could imagine, to which she replied, “*Dido*” (This was my mother’s way of spelling the word “Ditto”). I went on to say what I wished I could say to her now, that I am going to make her proud and live out the legacy she paved the way for. In her final reply my mother said, “*I’m sure you will*”.

—

Wherever she is now, I hope that she knows that her Lizzie-Pooh loves her to the moon and back.

—

This is for **you**, Mommy.

Contents

Abstract.....	iv
List of Tables.....	xi
List of Figures.....	xii
List of Supplemental Files.....	xiv
Acknowledgements.....	xv
1. Introduction	1
1.1 Rhabdomyosarcoma.....	1
1.1.1 Subtypes of RMS	2
1.1.2 Fusion-negative RMS	6
1.1.3 Fusion-positive RMS	7
1.2 The PAX3::FOXO1 regulatory network.....	9
1.2.1 The Hippo pathway.....	10
1.2.2 The Hippo pathway in RMS	12
1.2.3 The RUNX family of transcription factors	14
1.3 RUNX2	18
1.3.1 RUNX2-controlled programs.....	19
1.3.2 RUNX2 in cancer.....	25
1.3.3 Pharmacological approaches to RUNX2 inhibition.....	32
1.4 Interactions between the RUNX family of transcription factors and the Hippo pathway	33
2. Identifying a link between the Hippo pathway and RUNX2 in FP-RMS	36
2.1 Introduction.....	36
2.2 Methods.....	40
2.2.1 Generation of cell lines and constructs	40
2.2.2 Immunoblotting.....	40

2.2.3 <i>In vivo</i> xenograft assays.....	41
2.2.4 Hematoxylin and Eosin.....	41
2.2.5 Phosphoproteomics	41
2.2.6 ATAC-seq.....	43
2.2.7 Quantitative real time PCR	46
2.2.8 Statistics	46
2.3 Results	46
2.3.1 HSMM ^{P3F+DN} tumors exhibit decreased latency compared to HSMM ^{P3F+EV}	46
2.3.2 Phosphoproteomics approach to identify cellular circuits altered by MST1 loss-of-function	49
2.3.3 <i>RUNX2</i> motifs are enriched when MST1 activity is inhibited in HSMM ^{P3F+DN} cells expressing P3F, hTERT, MYCN, and MST1K59R.....	50
2.4 Discussion	52
2. Acknowledgements.....	53
3. <i>RUNX2</i> inhibition disrupts a PAX3::FOXO1- <i>RUNX2</i> feed-forward loop and dismantles oncogenic gene programs in FP-RMS.....	54
3.1 Significance.....	54
3.2 Introduction.....	54
3.3 Materials and methods	56
3.3.1 Patient samples.....	56
3.3.2 RNA-seq and bioinformatics of patient samples	60
3.3.5 RNA-seq of FP-RMS cells.....	61
3.3.6 Generation of cell lines and constructs	61
3.3.7 Quantitative real time PCR	64
3.3.8 Pharmacologic agents	64
3.3.9 ApoTox-Glo triplex assay	65
3.3.10 Immunoblotting.....	65
3.3.11 Colony formation assay	66

3.3.12 MF20 staining	66
3.3.13 Growth curves	66
3.3.14 <i>In vivo</i> xenograft assays	67
3.3.15 Hematoxylin and Eosin	67
3.3.16 Immunohistochemistry	68
3.3.17 Statistical analysis	70
3.3.18 Data availability	71
3.4 Results	71
3.4.1 <i>RUNX2</i> is highly expressed in RMS primary tumor tissue	71
3.4.2 <i>RUNX2</i> dependency is specific to pediatric sarcomas including RMS	76
3.4.3 <i>In vitro</i> KD of <i>RUNX2</i> in FP-RMS cell lines impairs oncogenic phenotypes	80
3.4.4. Bulk transcriptome analysis of <i>RUNX2</i> KD validates phenotypic findings and suggests impaired PAX3::FOXO1 activity	84
3.4.5 Conditional genetic <i>RUNX2</i> KD decreases PAX3::FOXO1 expression <i>in vitro</i> and impairs tumor growth <i>in vivo</i>	87
3.4.6 Identification of a feed-forward loop between PAX3::FOXO1 and <i>RUNX2</i>	92
3.4.7 Pharmacologic inhibition of <i>RUNX2</i> via the small molecule <i>RUNX2</i> inhibitor CADD522 impairs FP-RMS tumor xenograft formation	96
3.4.8 microRNA mediated regulation of <i>RUNX2</i> in ARMS patient samples	100
3.5 Discussion	101
3.6 Conflict of interest statement	106
3.7 Acknowledgements	106
4. Laying the foundations for future interrogation of <i>RUNX2</i> -Hippo pathway protein interactions	108
4.1 Introduction	108
4.2 Methods	109
4.2.1 Generation of cell lines and constructs	109
4.2.2 mRNA-seq of Rh30 and Rh4 cells	109

4.2.3 Co-immunoprecipitation	109
4.2.3 Immunoblotting.....	109
4.2.4 Statistics	110
4.3 Results and discussion points.....	110
4.3.1 <i>In vitro</i> and <i>in vivo</i> KD of <i>RUNX2</i> in FP-RMS cell lines impairs Hippo signaling ...	110
4.3.2 <i>RUNX2</i> , <i>PAX3::FOXO1</i> , and <i>TAZ</i> directly bind one another in FP-RMS	113
4.3.3 <i>In vitro</i> and <i>in vivo</i> KD of <i>YAPI</i> and <i>WWTR1/TAZ</i> in FP-RMS cell lines impairs <i>RUNX</i> signaling.....	117
4.3.4 Discussion	118
5. Discussion.....	120
5.1 Overview	120
5.2 Implications and future directions.....	121
5.2.1 <i>RUNX2</i> and beyond: pharmacologically targeting the relationships within FP-RMS core regulatory circuitry.....	122
5.2.2 Continued drug discovery	123
References.....	125
Biography	143

List of Tables

Table 1: Current Children’s Oncology Group RMS Stratification.....	2
Table 2: Histological Subtypes and Molecularly Defined Features in RMS.....	5
Table 3: RUNX Activity and Stability.	18
Table 4: RUNX2 Transcriptional Regulation in Development and Disease.....	24
Table 5 Patient Sample Demographics and Histological Interpretations.	58
Table 6: RNAi and Primer Sequences.	63
Table 7: Co-IP Antibodies: RUNX2-TAZ-PAX3::FOXO1 Interaction Studies.....	109
Table 8: NESs and FDRs of YAP/TAZ target gene signature for genes that are dependent on BRD4.	113

List of Figures

Figure 1: FP-RMS fusion oncoprotein frequencies and structures.....	8
Figure 2: Schematic representation of the mammalian Hippo signaling cascade.	11
Figure 3: PAX3::FOXO1 mediates noncanonical Hippo signaling.	13
Figure 4: Mammalian RUNX1, RUNX2, and RUNX3 genomic and protein structures and shared sequence homology.....	15
Figure 5: RUNX transcription factors orchestrate MSC differentiation.	20
Figure 6: Overview of models of RUNX2-mediated multi-layered gene regulatory mechanisms in skeletal cells.....	21
Figure 7: Tissue specific effect of the Runx2 transcription factor and its associations with various signaling pathways and target genes.....	23
Figure 8: Post-translational histone modifications at the <i>RUNX2</i> enhancer region in myoblasts reprogram C2C12 cells.....	23
Figure 9: The RUNX/CBF β complex and downstream functions in breast cancer.	26
Figure 10: Representative scheme of RUNX2's modulations to hallmarks of cancer.	27
Figure 11: RUNX2-targeting compound CADD522 molecular structure.....	33
Figure 12: Conserved domains of human RUNX proteins and their interactions with Hippo associated proteins.....	35
Figure 13: An unbiased approach to study MST1 inhibition in an isogenic HSMM model of FP-RMS.....	39
Figure 14: HSMM ^{P3F+EV} and HSMM ^{P3F+DN} cell line derivation.	47
Figure 15: Characterization of isogenic primary human myoblast cells harboring MST1 loss-of-function.	48
Figure 16: Top proteins hits exhibiting changes in phosphorylation in response to MST1 loss following TiO2 enrichment and mass spectrometry.....	49
Figure 17: Feasibility of using a phosphoproteomics approach to identify cellular circuits altered by MST1 loss-of-function.....	50
Figure 18: Bulk ATAC-seq of HSMM ^{P3F+DN} versus HSMM ^{P3F+EV}	52
Figure 19: mRNA-seq performed on archival fresh frozen RMS tissues classified according to their histological interpretation.....	75
Figure 20: Expression and survival analysis of <i>RUNX2</i> in FP-RMS and FN-RMS.....	77

Figure 21: <i>RUNX2</i> dependency analysis and characterization in RMS.	79
Figure 22: Expression and survival analysis of <i>RUNX1</i> in FP-RMS and FN-RMS.....	80
Figure 23: <i>RUNX2</i> knockdown in human FP-RMS cells (Rh30) impairs classical oncogenic phenotypes <i>in vitro</i>	82
Figure 24: <i>RUNX2</i> knockdown in human FP-RMS cells (Rh4) impairs classical oncogenic phenotypes <i>in vitro</i>	83
Figure 25: Transcriptomic alterations following <i>RUNX2</i> stable knockdown <i>in vitro</i>	85
Figure 26: Gene set enrichment analysis (GSEA) following <i>RUNX2</i> stable knockdown <i>in vitro</i>	87
Figure 27: Doxycycline inducible <i>RUNX2</i> knockdown in Rh30 FP-RMS cells.....	90
Figure 28: Additional <i>in vivo</i> experiments and expanded analyses.....	91
Figure 29: PAX3::FOXO1 and <i>RUNX2</i> reciprocally regulate one another in FP-RMS.	94
Figure 30: Rh30 cells treated with the <i>RUNX2</i> small molecule inhibitor CADD522 <i>in vitro</i>	97
Figure 31: Rh30 cells treated with the <i>RUNX2</i> small molecule inhibitor CADD522 <i>in vivo</i>	99
Figure 32: PAX3::FOXO1 transcriptionally upregulates <i>RUNX2</i> expression to prevent FP-RMS terminal differentiation and apoptosis via the defined regulatory circuitry.	106
Figure 33: Hippo pathway alterations following <i>RUNX2</i> stable knockdown <i>in vitro</i>	111
Figure 34: <i>WWTR1/TAZ</i> alterations following <i>RUNX2</i> conditional knockdown <i>in vivo</i>	113
Figure 35: TAZ mutant protein domain structures.....	114
Figure 36: Co-IP for flag-tagged TAZ mutants expressed in Rh4 FP-RMS cells.....	115
Figure 37: Co-IP for endogenous P3F and TAZ protein in Rh4 cells expressing an endogenous flag-tagged P3F.....	115
Figure 38: Co-IP for Flag-P3F and HA-TAZ in Rh4 FP-RMS cells.....	116
Figure 39: All <i>RUNX</i> proteins bind Flag-P3F, and HA-TAZ expressed in Rh4 FP-RMS cells..	117
Figure 40: <i>RUNX1</i> and <i>RUNX2</i> expression is decreased following <i>WWTR1/TAZ</i> and <i>YAP</i> RNAi knockdown in Rh4 and Rh28 FP-RMS cells.	118
Figure 41: Hypothesized therapeutic potential within the FP-RMS core regulatory circuitry.....	123

List of Supplemental Files

Supplemental files have been uploaded to Duke T3 and sent to all committee members.

Supplemental files include figures and spreadsheets that cannot be clearly shared in this text document.

Supplemental File 1: Patient mRNA-seq QC

Supplemental File 2: QC and differential expression mRNA, miRNA

Supplemental File 3: UpSet mRNA; miRNA

Supplemental File 4. RMS dependencies

Supplemental File 5. QC mRNA RUNX2 KD

Supplemental File 6. Differential expression mRNA RUNX2 KD

Supplemental File 7. GSEA mRNA RUNX2 KD

Supplemental File 8. Patient miRNA results

Supplemental File 9. Differential expression patient miRNA

Acknowledgements

It has been an honor and privilege to work with my mentor, Corinne M. Linardic for the past four and a half years, thank you for your guidance and wisdom, I am grateful for all that I have learned. As a member of the lab, I have had the opportunity to learn new techniques, mentor students, collaborate with others, and conduct science. I am grateful for the support of my thesis committee members, Kris Wood, Angela Koehler, Ann Marie Pendergast, and Yarui Diao.

I have grown personally and professionally throughout my doctoral training in part because of the mentors in my life. I would like to thank the Benjamin Alman, Laurie Graves, Michael Deel, Tammara Watts, Gerry Blobe, Stephen Skapek, Yarui Diao, Javed Khan, Darrell Green, Angela Koehler, Purushothama Tata, John Bushweller, Kim Stegmaier, and Everado Macias laboratories for their contributions to scientific discussion, collaborations, and mentorship throughout my time in graduate school. I am grateful for my first research mentors: Cris Hochwender, Noah Gordon, Daniel Chase, and Caroline Dealy, who encouraged me to continue academic research and supported my endeavors. I would like to thank Bill Heath and Sheila Gibson, my mentors and friends who exposed me to the pharmaceutical industry and field of patent law. I am very appreciative of my friends and colleagues from the Linardic laboratory, especially Kristianne Oristian and Marissa Just for their help making me feel at home and for their advice on how to succeed in the lab. Big thanks to my close friends Patrick Prochazka, Katherine Gonzalez, Audrey Chambers, Aanandi Munshi, and Samantha Weitzel for their unconditional support at Duke. This work was made possible with technical support provided by the Cancer Center Isolation Facility, Duke research core facilities, and Elaine Justice.

It has been an experience of a lifetime to complete my doctoral training. I am grateful to the Department of Cellular and Molecular Biology, Department of Pharmacology and Cancer Biology, and Department of Pediatric- Hematology/Oncology for supporting my training and intellectual growth.

Thank you to my ancestors who worked hard to give me the opportunity to study and follow my dream to develop cancer therapies for those who need it most. To my mother and stepfather who recently lost their lives to cancer but believed in me until the end. To my siblings and closest friends, thank you for supporting me throughout the crazy ride that graduate school is; you always listened to me and loved me, even if you didn't understand what I was talking about. Last but not least, thank you to Rebecca Timmons for your kindness, love, compassion, and support as an incredible scientist and my wife.

1. Introduction

1.1 Rhabdomyosarcoma

Globally, approximately 160,000 children and adolescents will develop cancer each year (1). In the United States, childhood cancer is the leading cause of death by disease after infancy (1), but more than 80% of children with access to modern multidisciplinary treatments in developed countries are cured (2). Despite decades of research and the development of curative therapies in specific cancers such as acute lymphoblastic leukemia (ALL), the most common childhood cancer with a 5-year survival rate of 92.3% (3), other cancers such as soft tissue sarcomas (STSs) rely on standard chemotherapy regimens that date back to the mid-twentieth century (4,5). STSs are a heterogeneous group of malignancies and represent more than 50 histologically and molecularly distinct subtypes (6). STS account for 1% of malignant tumors in adults and 8% of all malignant tumors in adolescents and young adults (7). The most common STS of childhood and adolescence is rhabdomyosarcoma (RMS).

RMS is comprised of a heterogeneous group of high-grade malignant neoplasms and characterized by the expression of skeletal muscle markers (8,9). In the United States, RMS accounts for 40% of STS in children and 3% of all childhood cancer diagnoses (10,11). Survival rates range from 6% to 100% depending on risk factors (12). RMS patients are assigned to a risk group based on clinicopathologic features such as the type of RMS, tumor location, tumor size, surgery outcomes, gene fusion status, and metastasis (10,12). Risk stratification dictates recommended treatments such as chemotherapy, surgery, and/or radiation therapy which permits local control of the primary tumor (12). Table 1 is a compiled overview of RMS risk stratification, generated from information contained in Haduong et al. and Heske et al (12,13).

Table 1: Current Children’s Oncology Group RMS Stratification.

***Clinical groups: (I) localized disease, completely resected, (II) localized disease, gross totally resection with microscopic positive margins and/or evidence of regional spread, (III) localized disease, incomplete resection with gross residual disease or biopsy only, (IV) distant metastatic disease present at onset. Adapted with permission under Creative Commons Attribution License from Haduong JH, Heske CM, Allen-Rhoades W, Xue W, Teot LA, Rodeberg DA, Donaldson SS, Weiss A, Hawkins DS, Venkatramani R. An update on rhabdomyosarcoma risk stratification and the rationale for current and future Children's Oncology Group clinical trials. *Pediatr Blood Cancer*. 2022 Apr;69(4):e29511. doi: 10.1002/pbc.29511. Epub 2022 Feb 7. PMID: 35129294; PMCID: PMC8976559.**

Risk Group	Stage	Clinical Group*	Age	Fusion Status
Low	1	I, II, III (orbit only)	Any	<i>FOXO1</i> –
	2	I, II		
Intermediate	1	III (non-orbit)	Any	<i>FOXO1</i> –
	1, 2, 3	I, II, III		<i>FOXO1</i> +
	2, 3	III		<i>FOXO1</i> –
	3	I, II		<i>FOXO1</i> –
	4	IV		<10 years
High	4	IV	>10 years	<i>FOXO1</i> –
			Any	<i>FOXO1</i> +

Overall survival for low-risk RMS patients is greater than 90%, but survival for high-risk cases is less than 20-30%, and less than 8% when metastatic (10,12,13). The standard chemotherapy protocol for RMS remains vincristine, actinomycin D, and an alkylator such as cyclophosphamide or ifosfamide, drug combinations discovered in the 1970s (14,15). This regimen is effective at treating low and intermediate-risk patients, but not high-risk patients such as those with metastatic and/or recurrent disease. New therapies are desperately needed.

1.1.1 Subtypes of RMS

Current World Health Organization criteria subclassify RMS into four histopathologic types that arise in children and adolescents: embryonal RMS (ERMS), alveolar RMS (ARMS), spindle cell/sclerosing RMS (SCRMS), and pleomorphic RMS (PRMS) (16). Descriptions of the morphologies associated with each histopathologic type can be found in Table 2, which was

generated from information contained in the following references(10,16-22). PRMS accounts for approximately 10% of cases and historically low incidence in children (23,24). SCRMS accounts for roughly 5%-10% of all adult and pediatric RMS cases, and apart from those with *MYOD1* mutations or *VGLL2* and *NCOA2* containing fusion oncogenes, outcomes have been historically excellent (25). The predominant histological variants of RMS, ERMS and ARMS have distinct outcomes. ERMS is most frequently associated with an intermediate risk stratification, but the 5-year survival of ARMS is less than 30% (26).

RMS histopathologic types, originally characterized based on light microscopy features, are driven by vastly different molecular mechanisms and are now classified molecularly based on the absence (fusion-negative RMS; FN-RMS) or the presence (fusion-positive RMS; FP-RMS) of a driver fusion oncogene. Fusion oncoproteins such as *PAX3::FOXO1* are not currently pharmacologically tractable. Non-fusion-driven sarcomas are largely characterized by the presence or absence of point mutations and/or other genetic aberrations in the RTK-RAS pathway, many of which have led to the development of novel therapies for children.

“Approximately 80% of ARMS cases are genetically driven by a paired box (*PAX*) gene-associated chromosomal translocation” (19). The majority of ARMS cases are divided into three groups; “in 60% of ARMS cases, the *PAX3* DNA-binding domain on chromosome 2 is fused to the forkhead box O1 (*FOXO1*) transactivation domain on chromosome 13 (*PAX3::FOXO1*); in 20% of ARMS cases, the *PAX7* gene on chromosome 1 is fused to the *FOXO1* gene on chromosome 13 (*PAX7::FOXO1*); and in 20% of ARMS cases, there is no association with the *PAX3/7::FOXO1* fusion oncogene nor with a different arrangement” (19). Other identified fusions oncogenes and molecular characteristics identified across histological types and in RMS can be found in Table 2. It is of importance to note that while ~80% of the time ARMS cases are ‘fusion positive’, 18-20% of the time ARMS cases do not express a fusion oncogene (27). Before implementing stricter histologic and cytologic criteria for ARMS, this number was up to 37%.

Clinically, pathologists only report on PAX3/7::FOXO1 fusion status and not any other RMS fusions. Consequently fusion-positive ERMS and ARMS cases are missed in clinical reporting. As histologic and cytologic criteria evolve, it is possible that the prevalence of ‘fusion- negative’ ARMS and ‘fusion-positive’ ERMS cases may change. In a study of a small cohort comprised of low-risk fusion-negative ARMS patients had better outcomes compared to fusion-positive ARMS patients (27). Given the inconsistencies between histologic classification and fusion status, it remains critical that physicians and researchers consider both when treating patients and conducting research to improve risk stratifications and outcomes.

Table 2: Histological Subtypes and Molecularly Defined Features in RMS.

Adapted with permission under Creative Commons Attribution License from Hettmer S, Linardic CM, Kelsey A, Rudzinski ER, Vokuhl C, Selfe J, Ruhen O, Shern JF, Khan J, Kovach AR, Lupo PJ, Gatz SA, Schäfer BW, Volchenboum S, Minard-Colin V, Koscielniak E, Hawkins DS, Bisogno G, Sparber-Sauer M, Venkatramani R, Merks JHM, Shipley J. Molecular testing of rhabdomyosarcoma in clinical trials to improve risk stratification and outcome: A consensus view from European paediatric Soft tissue sarcoma Study Group, Children's Oncology Group and Cooperative Weichteilsarkom-Studiengruppe. *Eur J Cancer*. 2022 Sep;172:367-386. doi: 10.1016/j.ejca.2022.05.036. Epub 2022 Jul 12. PMID: 35839732. Adapted with permission under Copyright Clearance Center License No. 6091550613772 from Agaram NP. Update on Myogenic Sarcomas. *Surg Pathol Clin*. 2019 Mar;12(1):51-62. doi: 10.1016/j.path.2018.10.003. Epub 2018 Dec 20. PMID: 30709448. Adapted with permission under Copyright Clearance Center License No. 6091551044130 from Shern JF, Chen L, Chmielecki J, Wei JS, Patidar R, Rosenberg M, Ambrogio L, Auclair D, Wang J, Song YK, Tolman C, Hurd L, Liao H, Zhang S, Bogen D, Brohl AS, Sindiri S, Catchpoole D, Badgett T, Getz G, Mora J, Anderson JR, Skapek SX, Barr FG, Meyerson M, Hawkins DS, Khan J. Comprehensive genomic analysis of rhabdomyosarcoma reveals a landscape of alterations affecting a common genetic axis in fusion-positive and fusion-negative tumors. *Cancer Discov*. 2014 Feb;4(2):216-31. doi: 10.1158/2159-8290.CD-13-0639. Epub 2014 Jan 23. PMID: 24436047; PMCID: PMC4462130.

Cancer Predisposition Genes with Pathogenic/Likely Pathogenic Variants in RMS (10)

TP53, NF1, BRCA2, GBA, MUTYH, ATM, DICER1, ERCC2, HRAS, Mismatch repair genes, SBDS, RECQL4, BLM, CBL, SDHx, TRIM37, ABCB11, BUB1B, CHEK2, COL7A1, SMARCA4, ALK, ATR, BRCA1, CDKN1C, DOCK8, ERCC5, FANCA, FANCC, FGFR4, FH, PTCH1, PTEN, RET, SERPINA1, TRIP13

Histological Subtypes (16)

ERMS	ARMS	SCRMS	PRMS
Primitive to small blue round cells, scattered rhabdomyoblasts, botryoid pattern	Alveolar pattern, sheets of medium sized cells, scattered giant cells	Spindle cell in fascicles; sclerosing 'pseudovascular' pattern	Pleomorphic rhabdomyoblasts

Identified Fusions (10,17,19)

<i>PAX3::NCOA2</i> <i>PAX3::NCOA1</i> <i>MEF2D::NTRK1</i> <i>EWSR1::DUX4</i>	<i>PAX3::FOXO1</i> <i>PAX7::FOXO1</i> <i>PAX3::FOXO4</i> <i>PAX3::NCOA2</i> <i>PAX3::NCOA1</i> <i>PAX3::INO80D</i> <i>PAX3::MAML3</i> <i>PAX3::MYOCD</i>	<i>VGLL2::NCOA2</i> <i>VGLL2::CITED2</i> <i>SRF::NCOA2</i> <i>TEAD1::NCOA2</i> <i>PAX8::PPARG</i> <i>EWSR1::TFCP2</i> <i>FUS::TFCP2</i> <i>MEIS1::NCOA2</i> <i>ZFP64::NCOA2</i> <i>MEIS1::FOXO1</i> <i>TCF12::VGLL3</i> <i>DCTN1::ALK</i>	None
---	---	--	------

		<i>CAVI::MET</i> <i>EP300::VGLL3</i> <i>HMGA2::NEGR1</i>	
Identified Mutations (bold) and Molecular/Copy Number Changes (<u>underlined</u>) (28,29)			
<i>IGF2</i> <i>NRAS</i> <i>KRAS</i> <i>NF1</i> <i>BRAF</i> <i>PTEN</i> <i>MET</i> <i>HRAS</i> <i>PIK3CA</i> <i>FBXW7</i> <i>FGFR4</i> <i>BCOR</i> <i>CTTNB1</i> <i>MYOD1</i> <i>MDM2</i> <i>BUB1B</i> <i>CTNNB1</i> <i>TP53</i> <i>CCND1</i> <u><i>IGF1R</i></u> <u><i>MDM2</i></u> <u><i>MYCN</i></u> <u><i>CDK4</i></u> <u>Aneuploidy</u> <u>Chr2</u> <u>Chr8</u> <u>Chr13</u>	<i>PI3KCA</i> <u><i>IGF2</i></u> <u><i>IGF1R</i></u> <u><i>MDM2</i></u> <u><i>MYCN</i></u> <u><i>CDKN2A</i></u> <u><i>CDK4</i></u> <u><i>BCOR</i></u> <u><i>MIR-17-92</i></u> <u><i>JUN</i></u> <u><i>TP53</i></u> <u>Chr8</u> <u>Chr13</u>	<i>MYOD1</i> <i>PIK3CA</i> <i>CDKN2A</i> <i>CDKN2B</i> <i>IGF1R</i> <i>BRAF</i>	<i>TP53</i> <i>RB1</i> <i>CDKN2A</i>

1.1.2 Fusion-negative RMS

FN-RMS cases account for more than 80% of RMS diagnoses and cases are associated with mutations that alter signal transduction pathways involved with processes such as cell cycle regulation and differentiation rather than a single oncogenic driver as in FP-RMS (30,31).

Genomic instabilities maintain subpopulation heterogeneity which in turn induces the expression of myogenic regulatory factors (MRF), such as MYOD1 and MYOG, as well as other myogenic transcription factors (32). In a study of FN-RMS patient tumor samples, RAS pathway mutations were found in more than 50% of cases (33).

Estimated 5-year survival for children with low-risk FN-RMS is approximately 90%, but the long-term survival without relapse for patients high-grade FN-RMS is less than 30% which exemplifies the heterogeneity of this subtype (34). FN-RMS tumors are commonly found in genitourinary systems and the head and neck, unlike FP-RMS, which often occurs in the extremities. Anatomic tumor location distribution has spurred conversations about whether specific FN-RMS mutations are associated with specific cells of origin and anatomic sites.

1.1.3 Fusion-positive RMS

Approximately 20% of all RMS cases are FP-RMS positive, and 60% of FP-RMS cases harbor the signature oncogenic driver, *PAX3::FOXO1*. The protein structures of all identified FP-RMS drivers are outlined in Figure 1, which was adapted from an illustration made by Assil Fahs, PhD in the Linardic lab to include additional information about fusion frequency with information from the following references (10,16-20,22,28). From this point further, when referring to FP-RMS, I will be referring to *PAX3::FOXO1*-positive ARMS unless otherwise specified. These intermediate and high-risk patients are associated with the worst event-free survival outcomes. *PAX3::FOXO1* is a chimeric transcription factor generated from the stable reciprocal translocation of chromosomes 2 and 13. *PAX3::FOXO1* impairs myogenic differentiation via epigenetic dysregulation that produces myoblast-like cells capable of sustained proliferation but not terminal myogenic differentiation (35,36).

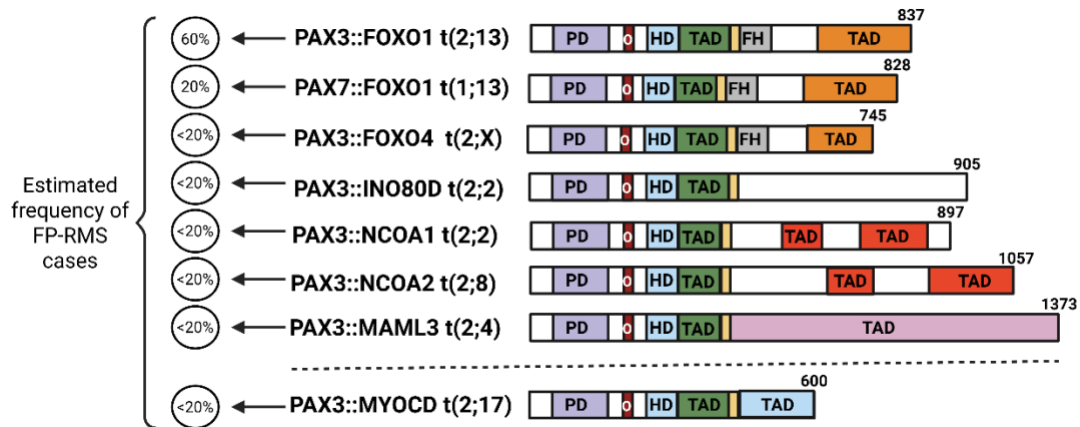


Figure 1: FP-RMS fusion oncoprotein frequencies and structures.

Diagram showing the fusion oncoproteins arising from chromosome translocations occurring in RMS and their estimated frequencies. Yellow indicates the protein fusion sites. PD: paired domain, O: octapeptide domain, HD: homeodomain, FH: fork head DNA-binding domain, and TAD: transcriptional activation domain. Dotted line separates the recently identified PAX3::MYOCD fusion oncogene from the most common (37). More data is needed to establish accurate frequencies of rare fusion oncoproteins. Figure adapted from illustration made by Assil Fahs, PhD in the Linardic Laboratory with additional information from (10,16-20,22,28). Created in BioRender. Mendes, E. (2025) <https://BioRender.com/w3u8mqz>.

FP-RMS tumors exhibit a higher degree of differentiated muscle gene signatures and have cell populations resembling non-terminally differentiated myoblasts and myocytes (9,23). Interestingly, single-cell (scRNA) sequencing data of FP-RMS patient tumors identified a small population of cells that adopted a ‘neuronal-like’ identity (23), but the significance of this is not yet known. Compared to FN-RMS, FP-RMS tumors harbor less genetic mutations and aberrations apart from the fusion driver.

FP-RMS represents a disproportionately high percentage of high-risk RMS cases. The estimated 5-year overall survival of FP-RMS is less than 30% for high-risk disease, and less than 8% when metastatic. Tumors typically arise in the extremities, unlike FN-RMS (32). The *PAX3::FOXO1* fusion gene was first identified in the early 1990s through physical mapping and cloning studies (38) and many advancements have been made to molecularly characterize FP-RMS, but despite decades of research, the standard chemotherapy protocol for RMS remains

vincristine, actinomycin D, and an alkylator such as cyclophosphamide or ifosfamide, drug combinations established in the 1970s (14,15). A better understanding of the PAX3::FOXO1 regulatory network is desperately needed to identify FP-RMS vulnerabilities and develop new therapies for patients.

1.2 The PAX3::FOXO1 regulatory network

Despite its role as an oncogenic driver, PAX3::FOXO1 is refractory to therapeutic targeting due to its lack of catalytic activity, and its intrinsically disordered structure, which leaves few pockets to bind small molecules (35,39,40). However, the transcriptional programs driven by PAX3::FOXO1 may yield alternate therapeutic targets. To identify novel druggable proteins in fusion-driven sarcomas, we must rigorously characterize patient tumors and cell lines to better understand the relationship between fusion drivers and the genomes which they govern. For example, prior work identified a PAX3::FOXO1 activated myogenic super-enhancer landscape that maintains the myoblastic state (41,42) including *MYCN* and *MYOD1* (41-44) and the involved proteins are being evaluated as drug targets (45,46).

During embryogenesis, core regulatory transcription factors, such as those found in FP-RMS, establish enhancers to better regulate developmental pathways, many of which are dysregulated in cancer (41,42,47). FP-RMS is largely driven by a translocated *FOXO1* super-enhancer downstream of the fusion oncogene and is typically restricted to a late stage of myogenesis (47). Core regulatory transcription factors activate ‘super-enhancers’ which are characterized by the presence of large deposits of active histone marks such as H3K27ac, H3K9ac, and H3K4me (41,47,48). Thus, in cancers like FP-RMS, chromosomal rearrangements allow super-enhancers to drive oncogene expression and guide developmental processes (47).

Hijacking super-enhancers bound by core regulatory transcription factors, especially those involved in mesenchymal stem cell and muscle differentiation, allows for the continued expression of FP-RMS fusion drivers (47). These enhancers and core regulatory loops marked by

CTCF boundaries insulate the gene neighborhood around PAX3::FOXO1 (47) to disrupt normal myogenic enhancer logic and maintain an oncogenic cell state (41,47). The disruption of core regulatory transcription factors involved in regulating key developmental pathways, such as MYOD1, RUNX1, RUNX2, were identified by chromatin state mapping of a PAX3::FOXO1 active enhancer (41,42,47,49). I hypothesize that inhibiting the transcription and downstream capabilities of these transcription factors and key regulatory pathways that intersect with these transcription factors, such as the Hippo developmental pathway, are viable FP-RMS treatment options. While my thesis is not focused on the Hippo pathway, our laboratory has worked on Hippo signaling in RMS. Given the multiple levels of intersection between RUNX2 and Hippo pathway proteins, and therefore future possible experimental directions, it is helpful to review Hippo signaling below.

1.2.1 The Hippo pathway

The Hippo pathway is a key developmental pathway first discovered in *Drosophila melanogaster*, but I will discuss pathway members with their human-associated nomenclature. The Hippo pathway is evolutionarily conserved across many organisms and regulates many biological processes such as cell growth and fate decisions, organ size, cell motility, and regeneration (50). The Hippo pathway includes key members such as MST1/2, SAV1, LATS1/2, MOB1, YAP, TAZ, and TEAD as shown in Figure 2 (51).

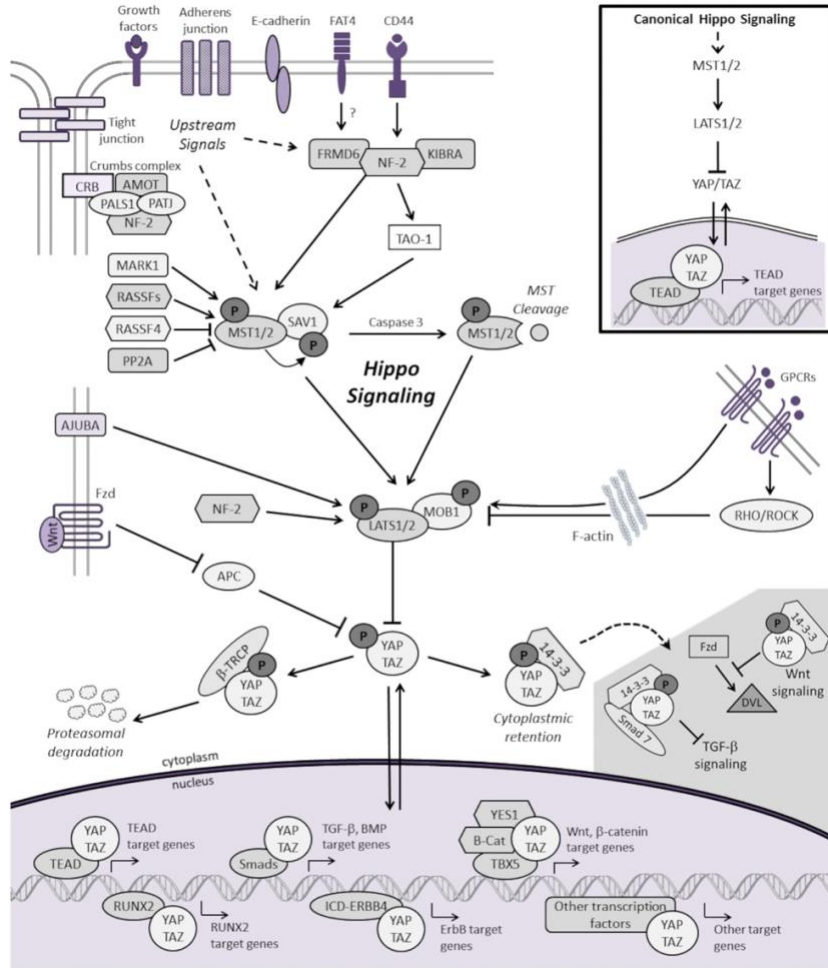


Figure 2: Schematic representation of the mammalian Hippo signaling cascade.

Canonical Hippo transduction involves MST1/2 and LATS1/2 kinases, which, in conjunction with SAV1 and MOB1, phosphorylate, and inhibit the transcriptional co-activators YAP and TAZ (gene name *WWTR1*). Regulation of YAP and TAZ are governed by plasma membrane proteins, cytoskeletal adaptor proteins, regulatory cross-talk from other signaling pathways, and intrinsic and extrinsic mechanical cues with the actin cytoskeleton. For simplicity, not all the known protein–protein interactions and regulators of Hippo signaling are represented. When Hippo signaling is “OFF”, YAP/TAZ translocate to the nucleus to serve as transcriptional co-activators for TEADs as well as other transcription factors (only a few of which are represented here) involved in cellular proliferation, differentiation, self-renewal, and apoptosis. Reprinted with permission under Creative Commons Attribution License from Deel MD, Li JJ, Crose LE, Linardic CM. A Review: Molecular Aberrations within Hippo Signaling in Bone and Soft-Tissue Sarcomas. *Front Oncol.* 2015 Sep 2;5:190. doi: 10.3389/fonc.2015.00190. PMID: 26389076; PMCID: PMC4557106.

When the Hippo pathway is “on” or “active”, MST1/2 and LATS1/2 are phosphorylated thus YAP/TAZ are phosphorylated. The phosphorylation of YAP/TAZ is facilitated by “an interaction between the PPxY (PY) motifs of LATS1/2 and the WW domains of YAP and TAZ” (52); these motifs and domains are critical to supporting, directing, and maintaining relationships with proteins outside of the Hippo pathway such as the Runt-related transcription factor (RUNX) family of proteins (53). When YAP/TAZ are phosphorylated, they are restrained to the cytoplasm and consequently cannot translocate to the nucleus to bind TEAD co-activators, which are responsible for directly binding DNA and driving the transcription of gene programs associated with key processes such as cell proliferation. When active in cancer, the Hippo pathway is considered tumor suppressive or “anti-cancer” due to the restrictions on YAP/TAZ.

When the Hippo pathways is “off” or “inactive”, MST1/2 are not phosphorylated therefore, YAP and TAZ are able to translocate to the nucleus, where they serve as transcriptional co-activators for TEAD proteins and other transcription factors (51,53). For example, TAZ often acts as a co-activator for RUNX2 to influence osteogenic differentiation. The multiple interactions of Hippo pathway members and proteins both inside and outside of canonical Hippo signaling highlight the importance of this pathway in normal biology as well as in disease.

1.2.2 The Hippo pathway in RMS

When I began my PhD, I began studying the Hippo pathway while working with a graduate student, Kristianne Oristian. Prior to my joining the lab, the role of the Hippo pathway was a major area of study in the lab (51,54-58).

In ERMS, prior lab members found that nuclear NOTCH and YAP protein expression are correlated in patient tumors (58). Inducible *YAP* inhibition *in vivo* decreased Notch and stem cell signaling (58). In FN-RMS, prior lab members identified a HES1-YAP1-CDKN1C function interaction from transcriptomic profiling of FN-RMS xenografts expressing a doxycycline-

inducible knockdown (KD) of *HES1*, suggesting that further investigation of *HES1* as a FN-RMS therapeutic target is warranted (55).

In FP-RMS, the lab established that PAX3::FOXO1 directly upregulates *RASSF4* transcription, a scaffolding protein, that binds to the c-terminal SARAH domain found in MST1/2 to restrain its tumor suppressor function (54,56). Downstream of suppressed MST1/2 signaling to MOB1 is altered; not canonical signaling to LATS1/2, YAP/TAZ, or TEAD (Figure 3) (56).

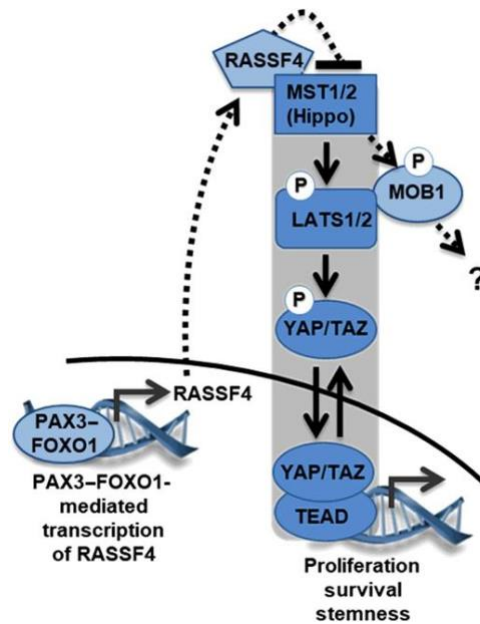


Figure 3: PAX3::FOXO1 mediates noncanonical Hippo signaling.

Canonical Hippo signaling (grey box) controls the localization of the transcriptional coactivators YAP1 and WWTR1. When active, YAP1/WWTR1 are phosphorylated and remain in the cytoplasm; when inactive, YAP1/WWTR1 move to the nucleus and coactivate TEAD transcription factors to support oncogenic phenotypes. Inhibition of MST1/2 by PAX3::FOXO1 through mediator, RASSF4, alters MOB1 expression (dashed line) and not canonical Hippo signaling (solid line). Reprinted with permission under Copyright Clearance Center License No. 6082061140052 from Oristian KM, Crose LES, Kuprasertkul N, Bentley RC, Lin YT, Williams N, Kirsch DG, Lincardic CM. Loss of MST/Hippo Signaling in a Genetically Engineered Mouse Model of Fusion-Positive Rhabdomyosarcoma Accelerates Tumorigenesis. *Cancer Res.* 2018 Oct 1;78(19):5513-5520. doi: 10.1158/0008-5472.CAN-17-3912. Epub 2018 Aug 9. PMID: 30093562; PMCID: PMC6459603.

Even though the bulk of my work is not centered around the Hippo pathway, many of my early experiments were focused on identifying therapeutic targets downstream of the inhibition of MST1. Throughout my PhD I have revisited the Hippo pathway through collaborations with the Deel lab; I will include these experiments and contributions throughout this document.

1.2.3 The RUNX family of transcription factors

The *RUNX* genes are a family of transcription factors capable of binding DNA and named after the 1989 discovery of the gene *runt* in *Drosophila melanogaster* which serves many roles in early embryogenesis (59,60). In mammals, the family includes three RUNX proteins, RUNX1, -2, and -3, and 2 homologues in *Drosophila melanogaster* (61). RUNX family members regulate the expression of genes by serving as transcriptional activators and repressors in a variety of processes including but not limited to cellular differentiation, cell cycle progression, cell lineage specification, DNA damage repair, and gene silencing/activation. RUNX1, -2, and -3 serve as “pioneer” transcription factors and are capable of binding DNA even when in its heterochromatic, condensed state, by scanning and binding target sites on nucleosomes to open chromatin and displace linker histones and chromatin remodelers; furthermore, they facilitate the recruitment of other transcription regulators (60,62).

1.2.3.1 RUNX genomic structures

The RUNX1, -2, and -3 genes share a dual promoter structure that is highly conserved throughout evolution (Figure 4) (60). Differential promoter expression is highly dependent on location, developmental stage, and disease process. Alternative splicing events lead to the generation of many RUNX transcript isoforms, and the predominant transcript expressed is context-dependent (63,64). While several genomic features, such as the Runt homology domain and transactivation domain sequences are conserved across the family, P1 versus P2 promoter expression may result in differing lengths of the 5' and 3' untranslated regions (UTRs); UTR specific sequences are further altered by microRNAs such as miR-27a (60,65).

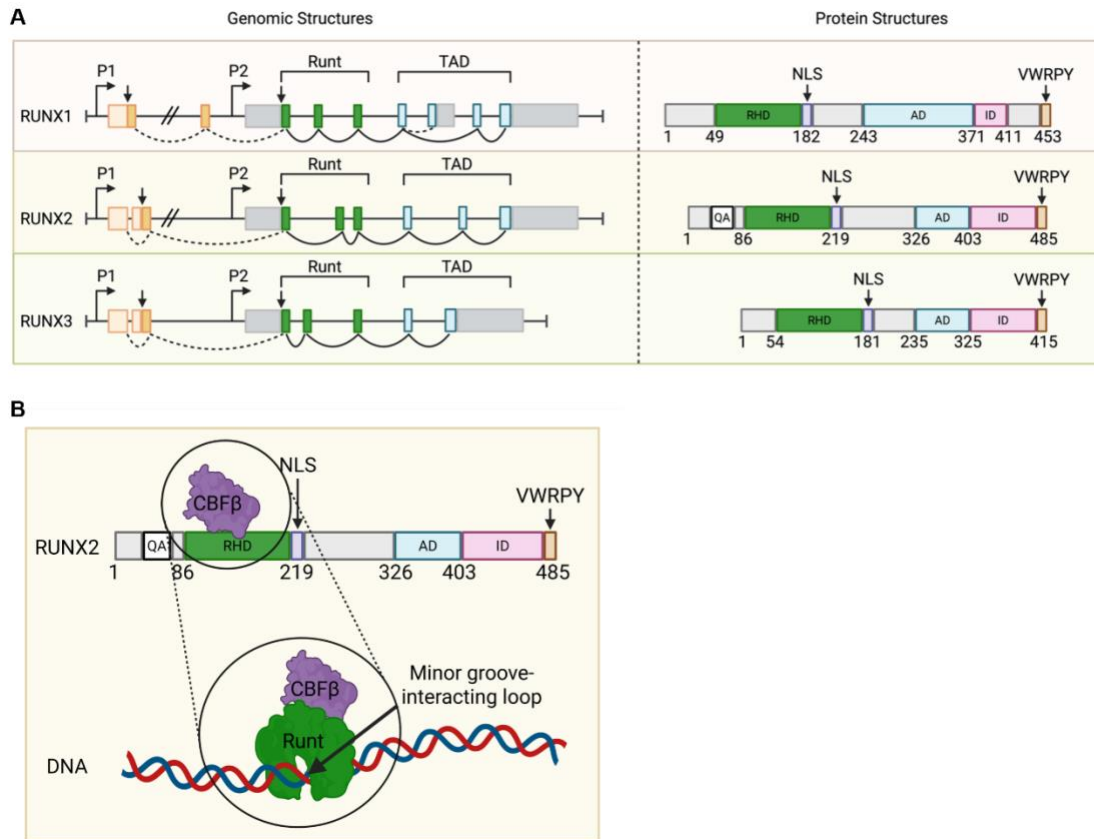


Figure 4: Mammalian RUNX1, RUNX2, and RUNX3 genomic and protein structures and shared sequence homology.

A, Left: Conserved genomic structure of human RUNX1 (Entrez Gene ID: 861), RUNX2 (Entrez Gene ID: 860) and RUNX3 (Entrez Gene ID: 864). The initiator ATG codons of P1- and P2-derived transcripts are indicated by downward pointing arrows. Exons coding for Runt and transactivation domains (TAD) are shown in dark and light blue, respectively, and UTRs are in white. Dominant splicing is indicated by a continuous line, and some alternative splicing is shown by a dashed line. **Right:** Schematic of human RUNX1 (NP_001001890), RUNX2 (NP_001265407) and RUNX3 (NP_004341) predominant protein structures and domains, including the conserved Runt homology domain (RHD), nuclear localization signal (NLS), transactivation (AD) and inhibitory (ID) domains, C-terminal Groucho/TLE binding site (VWRPY), and the RUNX2-specific glutamine/alanine-rich (QA) sequence. Adapted with permission under Creative Commons Attribution License from Mevel R, Draper JE, Lie-A-Ling M, Kouskoff V, Lacaud G. RUNX transcription factors: orchestrators of development. *Development*. 2019 Sep 5;146(17):dev148296. doi: 10.1242/dev.148296. PMID: 31488508. Adaptation created in BioRender. Mendes, E. (2025) <https://BioRender.com/3nmg9iv>. **B,** Graphic of RUNX2 protein structure and focused view of RHD binding to DNA and to CBF β . Graphic is based on the RHD-CBF β bound crystal structure first generated by Tahirov et al., Adapted with permission under Copyright Clearance Center License No. 6091490074285 from Tahirov TH, Inoue-Bungo T, Morii H, Fujikawa A, Sasaki M, Kimura K, Shiina M, Sato K, Kumasaka T, Yamamoto M, Ishii S, Ogata K. Structural analyses of DNA recognition by the AML1/Runx-1 Runt domain and its allosteric control by CBFbeta. *Cell*. 2001 Mar 9;104(5):755-67. doi: 10.1016/s0092-

8674(01)00271-9. Erratum in: Cell 2001 Apr 20;105(2):291. PMID: 11257229. Adaptation created in BioRender. Mendes, E. (2025) <https://BioRender.com/3nmg9iv>.

1.2.3.2 RUNX protein structures

There are shared features and mechanisms of action between all three RUNX family members, but each “exhibit distinct tissue specific expression patterns” and are implicated in different diseases (66). In humans, RUNX1 is expressed in all tissues except the brain and heart and is implicated in many hematological malignancies such as acute myeloid leukemia (AML). In humans, RUNX2 is specifically expressed in osteoblast lineage cells, osteoblasts, chondrocytes, and mesenchymal stem cells (MSCs) to regulate osteogenic differentiation; recent studies report that RUNX2 protein expression has been identified in mammary glands and thymocytes, but these reports are less appreciated (67). RUNX2 is considered a pan-cancer relevant biomarker and highly expressed in many cancers such as pancreatic and breast cancer (68). In humans, RUNX3 is closely associated with gastrointestinal cancers and expressed in the thymus, spleen, and gastrointestinal tract (69). Subcellularly, RUNX1 protein is exclusively expressed in the nucleus, while RUNX2 and RUNX3 are expressed in the nucleus and cytoplasm, though RUNX2’s cytoplasmic presence is poorly documented (70,71).

At the N-terminus, the Runt head domain (RHD) binds DNA at the consensus RUNX motif ‘PyGPyGGTPy’ (PY) and facilitates protein-protein interactions and is found in all family members (Figure 4). The nuclear localization signal/sequence (NLS) maintains RUNX nuclear localization, though RUNX2 and RUNX3 have limited reports of cytoplasmic localization (60). The proteins’ C-terminus is less conserved across RUNX1, -2, and -3, but they do share an activation domain, inhibitory domain, and PY/VWRPY motifs, which serve as recruitment signals for co-repressors and bind a variety of other proteins such as YAP and TAZ (53,60). Unlike RUNX1 and RUNX3, RUNX2 has a variable poly-glutamine (Q) (polyQ), poly-alanine (A) (polyA) tandem (QA) repeat domain which is believed to act as a ‘tuning knob’ and can influence protein-protein interactions, but its full function is poorly understood (72).

1.2.3.2 RUNX mechanisms of action

Each member of the RUNX2 family of transcription factors are part of a “heterodimeric complex formed by dimerization between the α subunit, RUNX, and its primarily binding partner and coactivator, core binding factor subunit β (CBF β)” (60). CBF β is a regulatory element that does not bind DNA. Instead, CBF β allosterically increases the DNA-binding affinity and stability of the RUNX-CBF β complex (60). Also, CBF β protects RUNX proteins from phosphorylation and proteasomal degradation. RUNX proteins bind CBF β directly at the RHD (Figure 4) (60). RUNX proteins are capable of binding other coactivators such as CBP/p300 (73), SMADs (74), BRD2/4 (66), TAZ (75), and others.

RUNX proteins are also capable of binding DNA independently of a coactivator (66,76) and can serve non-transcriptional roles such as serving as an epigenetic ‘bookmark’ when it is retained on mitotic chromosome to preserve cell fate (77). Finally, it is important to note that the activity and stability of RUNX proteins is dependent on post-translational modifications, which can modify RUNX activation, repression, and stability (Table 3) (60). In many instances, crosstalk between RUNX factors has been described; for example, in MCF10CA1a breast cancer cells, *RUNX1* decrease resulted in *RUNX2* increase within the murine mammary fat pad microenvironment (78). RUNX1, -2, and -3 can also play redundant roles, where loss of *Runx1* in mice is rescued by *Runx2*, but the full extent of these relationships in mice and humans is unknown (60).

Table 3: RUNX Activity and Stability.

RUNX factors can act as transcriptional activators or repressors depending on binding partners and post-translational modifications. A summary of RUNX associated post-translational modifications is outlined below. Adapted with permission under Creative Commons Attribution License from Mevel R, Draper JE, Lie-A-Ling M, Kouskoff V, Lacaud G. RUNX transcription factors: orchestrators of development. *Development*. 2019 Sep 5;146(17):dev148296. doi: 10.1242/dev.148296. PMID: 31488508.

Activation	Repression	Stability
Acetylation	Deacetylation	Ubiquitylation
Methylation	Phosphorylation (Y)	SUMOylation
Phosphorylation (S/T)	Methylation	

1.3 RUNX2

From this point further I will primarily focus on RUNX2 except for in section 1.4.

RUNX2 is best known for its essential role in the differentiation of MSCs into osteoblast and chondrocyte lineages. The human *RUNX2* gene is located on chromosome 6 (6p21) (79) and has 2 functional isoforms (type I and type II) under the control of 2 alternate promoters P1 and P2. RUNX2-I is 513 amino acids and RUNX2-II, the ‘canonical’ isoform, is 528 amino acids due to its inclusion of exon 1 which encodes the ‘QA’ domain (Figure 4) (80). Both isoforms share the same C-terminus and differ in their N-terminus. RUNX2-I plays a larger role in the commitment of cells to the osteoblast lineage and is implicated in early thymocyte development, and RUNX2-II has a more prominent role in later stages of osteoblast differentiation (80). RUNX2-I is translated from the P2 promoter and RUNX2-II is translated from the P1 promoter (81). In many normal cell types, RUNX2-I is the predominant isoform (81). In cancer the predominant isoform varies; for example, in oral squamous cell carcinoma, RUNX2-II was found to be the predominant isoform (82), but RUNX2-I is the predominant isoform in papillary thyroid carcinomas (83). Both isoforms are expressed in many normal cell and cancer types, but their expression is largely regulated by enhancers, which remain to be elucidated (84,85). At present, there are no commercially available antibodies to distinguish between isoforms therefore, going forward I do not differentiate between each.

RUNX2 is a master regulator and organizer, working in tandem alongside other transcription factors and co-factors (86). RUNX2 also has roles in the differentiation of bipotent MSCs into myotubes and osteogenic cells (87), but these roles are less well understood. In mice, functional deficiency of RUNX2 in osteoblasts does not result in failed embryonic skeletogenesis but disrupts postnatal bone formation (88). *RUNX2* knockout mice display a wide range of other phenotypic abnormalities such as T-cell defects, T-cell lymphomas, and megakaryocyte defects (89). In humans, *RUNX2* mutations are linked to cleidocranial dysplasia syndrome (CCD), an autosomal skeletal disorder (79); additionally, aberrant gene and protein expression of RUNX2 is closely associated with many cancers and oncogenic phenotypes (68). Sections 1.3.1 and 1.3.2 will describe additional normal and disease processes that RUNX2 regulates.

1.3.1 RUNX2-controlled programs

RUNX2 mediates the regulatory mechanisms that govern human skeletal development and the differentiation of MSCs into bone and cartilage in processes called osteogenesis and chondrogenesis (Figure 5) (60,90). RUNX2 is critical to the commitment phase that transforms MSCs into osteoblasts in osteogenesis and promotes chondrocyte maturation in chondrogenesis. Common RUNX2 gene targets include, but are not limited to, *vascular endothelial growth factor A (VEGF)*, *osteopontin (OPN)*, *osteocalcin (OC)*, and *metalloproteinases (MMP)* (91).

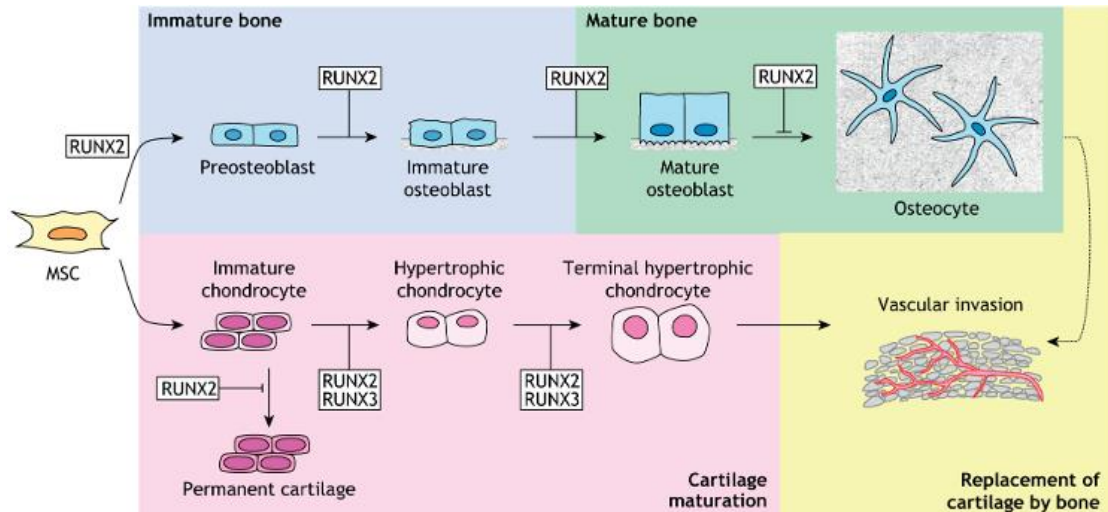


Figure 5: RUNX transcription factors orchestrate MSC differentiation.

Roles of RUNX2 and other RUNX transcription factors in MSC differentiation. Bone is generated through the differentiation of MSCs toward either bone-forming osteoblasts or cartilage-forming chondrocytes. The osteoblast fate choice and the maturation pathway resulting in intramembranous ossification are largely controlled by RUNX2. Cartilage differentiation is regulated by both RUNX2 and RUNX3. Inhibitory roles are indicated by bars. Reprinted with permission under Creative Commons Attribution License from Mevel R, Draper JE, Lie-A-Ling M, Kouskoff V, Lacaud G. RUNX transcription factors: orchestrators of development. *Development*. 2019 Sep 5;146(17):dev148296. doi: 10.1242/dev.148296. PMID: 31488508.

Osteogenesis is balanced between bone formation (osteoblasts) and reabsorption (osteoclasts). Osteogenesis consists of endochondral ossification (cartilage) where MSCs differentiate into chondrocytes to form a cartilage model and intramembranous ossification (bone) where MSCs cluster and differentiate into osteoblasts (bone forming cells) (90). Endochondral ossification often precedes osteogenesis in endochondral ossification, but intramembranous ossification can and does occur independently of endochondral ossification (Figure 5). Gene regulatory programs acting on cis-regulatory elements (CRE) govern osteogenesis to control cell line specification and differentiation alongside other transcription factors (90). An overview of models of RUNX2-mediated multi-layered gene regulatory mechanisms in skeletal cells is outlined in Figure 6.

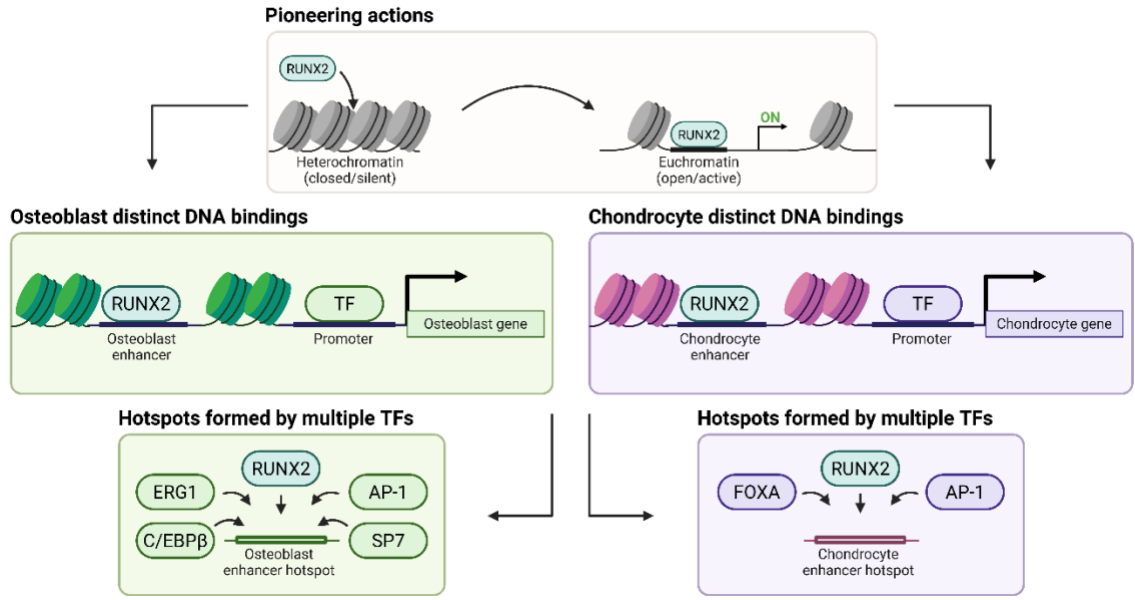


Figure 6: Overview of models of RUNX2-mediated multi-layered gene regulatory mechanisms in skeletal cells.

RUNX2's role as a pioneer transcription factor. Gene expression is controlled by interactions between CRE and trans-regulatory factors such as transcription factors and regulators. Promoters and enhancers represent examples of CRE and are visualized in the yellow, green, and purple panels above. Yellow box: In many cell types, such as osteoblasts and chondrocytes, RUNX2 can 'pop open' condensed heterochromatin to bind enhancers and/or promoters, likely by directly interacting with histones and histone acetyltransferases (HAT) to modify histone tails and loosen DNA through enzymatic reactions (73). In *Runx2* deficient mice, pioneering actions are lost therefore, downstream activation of osteoblast and chondrocyte specified genes are subsequently lost (90). Once CRE are accessible, RUNX2 binds osteoblast (green boxes) and chondrocyte (purple boxes) enhancers of osteoblast and chondrocyte specified genes such as *OSE2* in osteoblasts and *COL10A1* in chondrocytes (92). In many instances, RUNX2 does not act alone but instead facilitates the recruitment of osteoblast (green boxes) and chondrocyte (purple boxes) associated transcription factors (TF) that bind specified promoters or enhancer hotspot regions. Reprinted with permission under Creative Commons Attribution License from Hojo H. Emerging RUNX2-Mediated Gene Regulatory Mechanisms Consisting of Multi-Layered Regulatory Networks in Skeletal Development. *Int J Mol Sci.* 2023 Feb 3;24(3):2979. doi: 10.3390/ijms24032979. PMID: 36769300; PMCID: PMC9917854. Adaptation created in BioRender. Mendes, E. (2025) <https://BioRender.com/dcx6ovp>.

Separate though often linked to osteogenesis, chondrogenesis is the process in which MSCs fully differentiate into cartilage. RUNX2 plays a lesser role in chondrogenesis, but it has been reported that *Twist-1* expression in the perichondrium (a layer of dense, fibrous connective tissue surrounding cartilage (93)) regulates Runx2 function which signals to *Fgf18* to negatively regulate chondrocyte maturation in this context (94).

1.3.1.1 The roles of RUNX2 beyond osteogenic differentiation

Please note that throughout this section I will refer to both mouse ‘Runx2’ and human ‘RUNX2’ depending on the literature available in each system. Not only is Runx2 responsible for the commitment of MSCs into osteoblasts, but it plays various functional roles in various cells and tissues, implying that the mechanisms by which Runx2 exerts its functions (normal and pathologic) also differ (Figure 7) (95). RUNX2 is also responsible for controlling the fate of myogenic precursor cells like myoblasts to stimulate their trans-differentiation into osteoblasts (Figure 8) (87). Additionally, *Runx2* overexpression in adipose-derived stem cells stimulates the induction of osteoblastic differentiation and the formation of mineralized nodules (96), as well as for chondrocytes to transdifferentiate into osteoblasts (97). A recent study in mice reports that embryonic and adult mouse brains exhibited variable expression of *Runx2* (98). Transient overexpression of *Runx2* led to increased transactivation of *MMP13* gene expression without altering the transcription of typical Runx2 gene targets such as *OPN* in astrocytes, which suggests that Runx2 may serve an important role in the brain. Another study found that *Runx2* overexpression is detected following peripheral nerve regeneration but not nerve development (95).

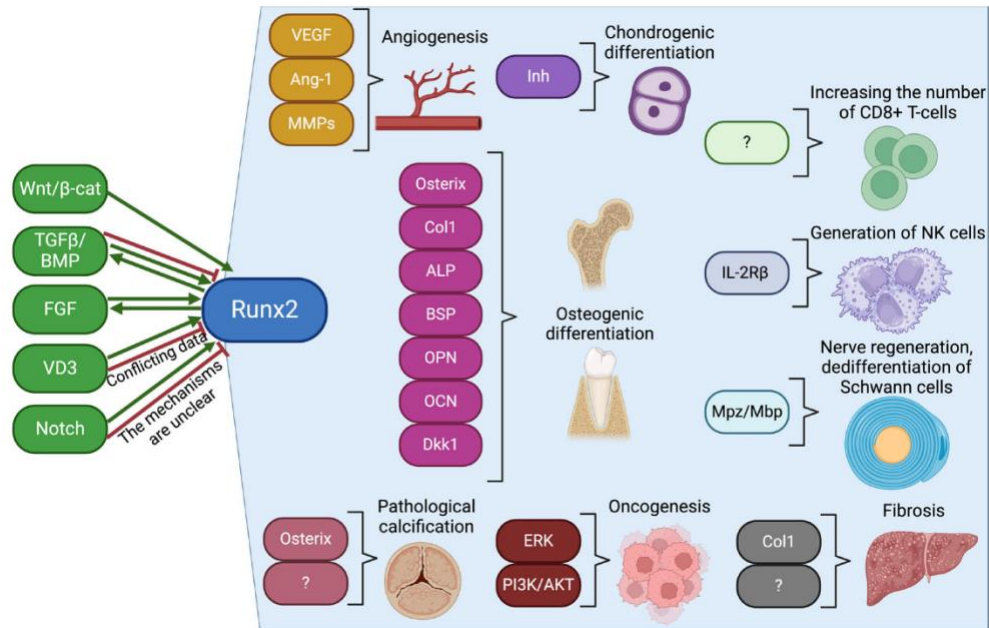


Figure 7: Tissue specific effect of the Runx2 transcription factor and its associations with various signaling pathways and target genes.

The function role of Runx2 differs in various cell lines and tissues, implying that the mechanisms by which Runx2 exerts its functions also differ. Reprinted with permission under Creative Commons Attribution License from Azarkina K, Gromova E, Malashicheva A. "A Friend Among Strangers" or the Ambiguous Roles of Runx2. *Biomolecules*. 2024 Oct 31;14(11):1392. doi: 10.3390/biom14111392. PMID: 39595568; PMCID: PMC11591759.

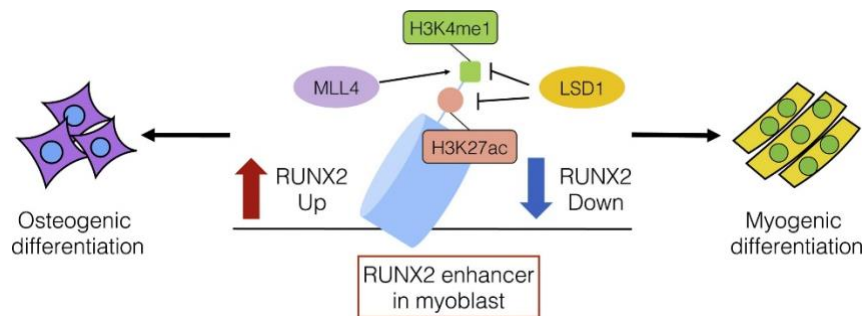


Figure 8: Post-translational histone modifications at the *RUNX2* enhancer region in myoblasts reprogram C2C12 cells.

Histone methylation dynamics play an important role in cellular reprogramming during development. Lysine demethylase, LSD1 is required for myogenic differentiation and MLL4 is required for osteoblast differentiation of C2C12 mouse myoblasts. This finding supports the notion that RUNX2 signaling in myogenic precursors can encourage differentiation down both myogenic and osteogenic lineages. Reprinted with permission under Copyright Clearance Center License No. 608323231005557 from Munehira Y, Yang Z, Gozani O. Systematic Analysis of Known and Candidate Lysine Demethylases in the

Regulation of Myoblast Differentiation. J Mol Biol. 2017 Jun 30;429(13):2055-2065. doi: 10.1016/j.jmb.2016.10.004. Epub 2016 Oct 11. PMID: 27732873; PMCID: PMC5388604.

More work is needed to determine what the role of Runx2/RUNX2 is in the central nervous system (CNS) of mice and humans. Table 4 outlines the diverse roles of RUNX2 in normal biology and in human disease. Even though RUNX2 has traditionally been known as the primary driver of osteogenic differentiation, it is clear that RUNX2 plays a large role in many regulatory processes outside of osteogenesis, and that its dysregulation is implicated in many disease processes such as those involved in cancer (60,67,75,84,85,87,89-91,95).

Table 4: RUNX2 Transcriptional Regulation in Development and Disease.

Adapted with permission under Copyright Clearance Center License No. 6083300378292 from Brusgard, J.L., Passaniti, A. (2014). RUNX2 Transcriptional Regulation in Development and Disease. In: Kumar, R. (eds) Nuclear Signaling Pathways and Targeting Transcription in Cancer. Cancer Drug Discovery and Development. Humana Press, New York, NY. https://doi.org/10.1007/978-1-4614-8039-6_3. Additional sources used are listed on the right-hand side of the table.

Normal function	Source
Osteogenesis	(91)
Angiogenesis	(91) (95)
Chondrogenesis	(90) (95)
Context dependent transdifferentiation of MSC lineages	(87) (96)
Early thymus development	(99)
Peripheral nerve regeneration	(95)
Disease	Source
Fibrous dysplasia	(91)
Fibrosis	(95)
AML	(91)
Thyroid papillary carcinoma	(91)
Pituitary tumors	(91)
Ewing sarcoma	(91)
Giant cell tumor of the bone	(91) (100)
Prostate carcinoma	(91)

Breast carcinoma	(91)
Multiple myeloma	(91)
Glioblastoma multiforme	(91)
Glioblastoma	(101)
Hypothyroidism	(91)
Chondrosarcoma	(91)
Lung carcinoma	(91)
CCD	(91)
Colon carcinoma	(91)
Melanoma	(91) (102)
Pancreatic carcinoma	(91)
Hepatocellular carcinoma	(103)

1.3.2 RUNX2 in cancer

RUNX2 commonly participates in cancer progression and tumorigenesis. While RUNX2 is not a codified ‘cancer biomarker’, it is being considered due to its association with many cancer types (Table 4) (68). Interestingly, in breast cancer the RUNX/CBF β core binding factor complex works alongside many transcription co-activators and co-repressors to regulate cellular pathways, like PAX3::FOXO1 does in FP-RMS (Figure 9) (104). RUNX2 is associated with poor prognosis and functions as a tumor facilitator, frequently collaborating with other signaling pathways such as the TGF- β and Hippo pathways (68,75,105). For the rest of section 1.3.2 I will review the cancer hallmarks that RUNX2 is associated with (Figure 10).

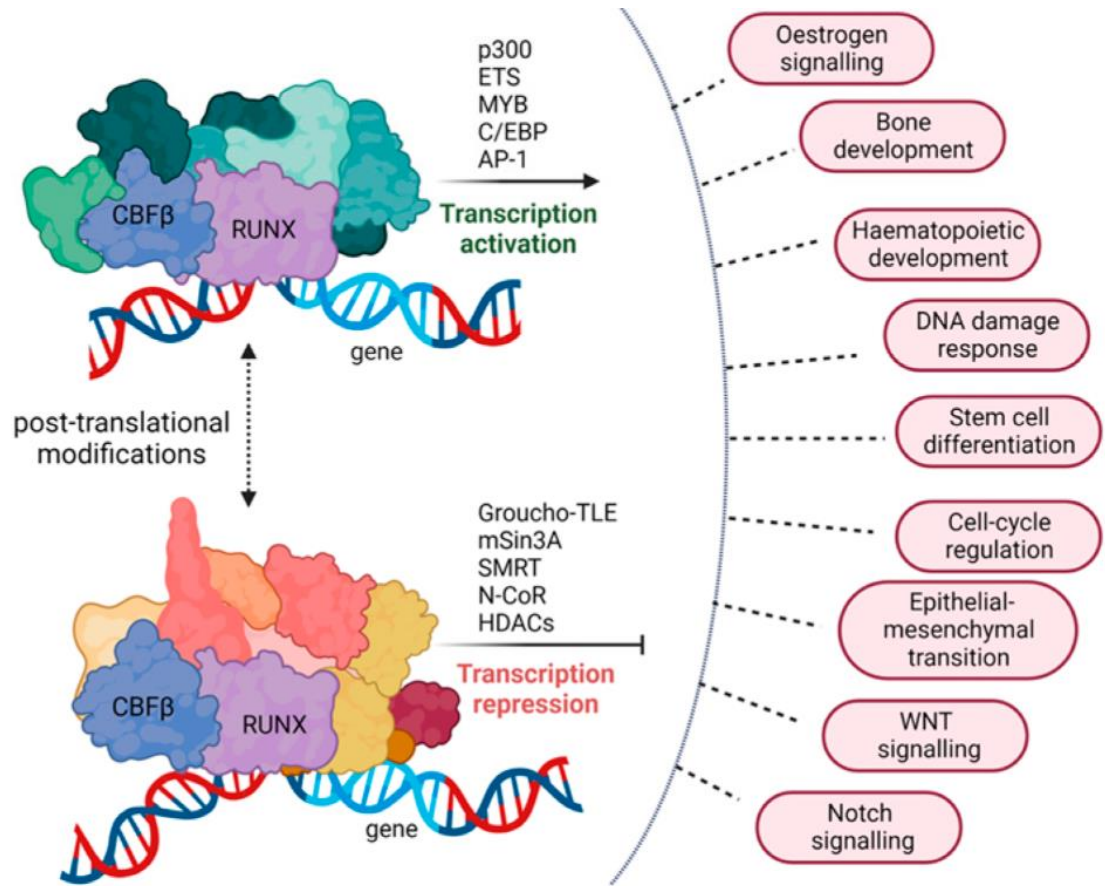


Figure 9: The RUNX/CBFβ complex and downstream functions in breast cancer.

The core binding factor complex works in conjunction with an array of transcription co-activators and co-repressors to regulate crucial cellular pathways. Reprinted with permission under Creative Commons Attribution License from Khan AS, Campbell KJ, Cameron ER, Blyth K. The RUNX/CBFβ Complex in Breast Cancer: A Conundrum of Context. *Cells*. 2023 Feb 16;12(4):641. doi: 10.3390/cells12040641. PMID: 36831308; PMCID: PMC9953914.

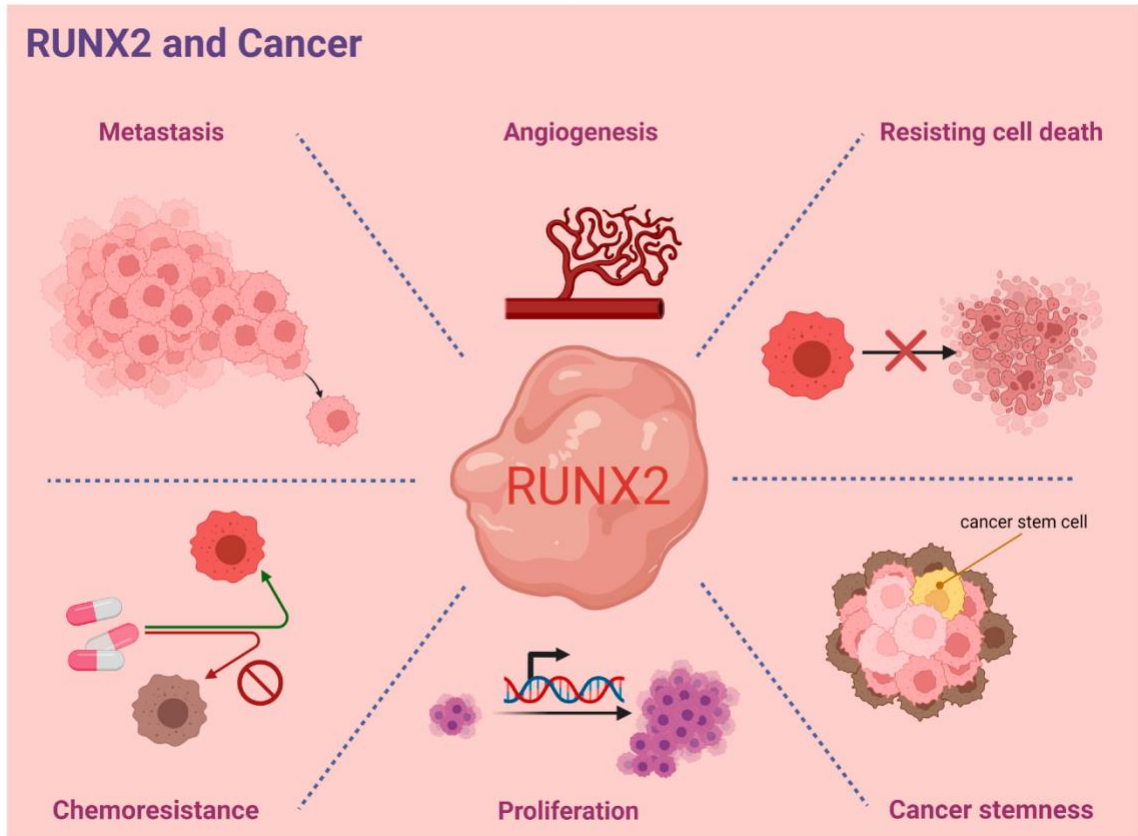


Figure 10: Representative scheme of RUNX2’s modulations to hallmarks of cancer.

Adapted with permission under Creative Commons Attribution License from Lin TC. **RUNX2 and Cancer. Int J Mol Sci. 2023 Apr 10;24(8):7001. doi: 10.3390/ijms24087001. PMID: 37108164; PMCID: PMC10139076.**

1.3.2.1 RUNX2 and angiogenesis

RUNX2 is normally expressed in endothelial and smooth muscle cells during blood vessel development. Angiogenesis and osteogenesis are tightly linked processes; in mesenchymal cells, RUNX2 overexpression “upregulates the expression of hypoxia-inducible factor 1 α and VEGF, which stimulates angiogenesis” (106). In cancer, RUNX2 upregulates *VEGF* expression to promote the malignant transformation and progression of chondrosarcoma (106). In melanoma, Cecconi et al., deleted the Runt domain in A375 melanoma cells, performed proteomics, and validated their findings to discover that the Runt domain sustained neo-angiogenesis (107). These findings suggest that RUNX2 expression in cancer creates a signaling environment capable of driving and sustaining oncogenic phenotypes, such as angiogenesis. Given the connection

between RUNX2 and VEGF, and successes documented using VEGF inhibitors such as bevacizumab to treat cancer (108), RUNX2 inhibition may be a promising therapeutic option for patients with refractory disease.

1.3.2.2 RUNX2 and resisting cell death

RUNX2 plays an important role in preventing cell death in many cancer types. In lung cancer, *RUNX2* overexpression prevented apoptosis through the direct transcriptional regulation of *BCL2* and indirect regulation of *BCL-XL* and *MCL1* (109). Similarly in prostate cancer, *RUNX2* inhibition resulted in increased apoptosis, and RUNX2 was found to directly bind the promoter of many apoptosis-related genes, such as *BCL-2*, *STAT5a*, *TRAIL*, and *PUMA* to create an apoptosis-resistant environment when expressed (110). In pancreatic cancer, *RUNX2* depletion enhanced gemcitabine sensitivity of *p53*-deficient AsPC-1 cells via the activation of the Tap63-mediated cell death pathway, which further highlights the role of RUNX2 in chemoresistance and cell death (111).

1.3.2.3 RUNX2 and cancer stemness

In lung adenocarcinoma cells exposed to cigarette smoke, Sharma et al. found that smoke exposure induces EMT, metastasis, and stemness via the upregulated RUNX2/galectin-3 pathway (112). Tumorsphere assays to study cancer stem cells (CSCs) have shown that expression of *RUNX2* results in increased tumorsphere volume and size. In a breast cancer study using MDA-MD-231 cells (113), *RUNX2* overexpression led to an increase in breast cancer cell tumorsphere volume; additionally, *RUNX2* overexpression in MCF-7 breast cancer cells led to the induction of sphere formation and increased proliferation, migration, and invasion (114). Another study in HER2-positive breast cancer found that *RUNX2* expression increased the size of HER2-mediated tumorsphere size (75). Despite the strong body of literature supporting RUNX2's role in development, more research is needed to determine RUNX2's impact on cancer stemness.

1.3.2.4 RUNX2 and proliferation

During osteoblast differentiation in mice, Runx2 is weakly expressed in uncommitted MSCs and later upregulated in pre-osteoblasts (115). Runx2 reaches its peak expression level in immature osteoblasts and is later downregulated in mature osteoblasts (115). In this process, Runx2 enhances osteoblast progenitor cell proliferation by upregulating *Fgfr2* and *Fgfr3* (115). Given the inherent role of RUNX2 in normal differentiation processes, it is not surprising that RUNX2 can control proliferation programs and the cell cycle in cancer contexts. There are numerous reports of increased RUNX2 expression driving proliferation. Interestingly, in cervical cancer (116), pancreatic cancer (117), and hepatocellular carcinoma (118), RUNX2 expression was inhibited by the overexpression or silencing of non-coding RNAs, which highlights the importance of the epigenome in directing RUNX2-associated oncogenic programs.

1.3.2.5 RUNX2 and chemoresistance

In an epirubicin-resistant cell line of triple-negative breast cancer (TNBC), MDA-MB-231-Re, *RUNX2* KD decreased epirubicin chemoresistance (68). In another TNBC study, RUNX2 affected “chemoresistance by regulating cancer stemness through direct binding to TGF- β , and that TGF- β regulates RUNX2 expression” (119). In osteosarcoma, RUNX2 KD increased sensitivity to cisplatin (68). Mechanistically, a synergistic combination of HDAC4/8 inhibition increased osteosarcoma sensitivity to doxorubicin via the pAKT/RUNX2 pathway (120). Together these findings highlight the therapeutic potential of RUNX2 inhibition, not just as a monotherapy, but to be included in combination drug trials with standard chemotherapeutics.

1.3.2.6 RUNX2 and metastasis

RUNX2 overexpression in breast and prostate cancer has been significantly associated with the promotion of epithelia to mesenchymal (EMT) transition as well as metastasis. In lymph node (LN) negative breast cancer, many patients with breast to bone metastasis are RUNX2

positive. Li et al., found that RUNX2 transcriptionally targets *integrin subunit alpha-5 (ITGA5)*, which plays a role in cancer migration. In an ITGA5-dependent manner, RUNX2 facilitates cancer cell recruitment and colonization in the bone (121). In primary bone cancer, an interaction between RUNX2 and YBX1 sustains a pro-metastatic niche (64,122). In lung adenocarcinoma, it was found that the long non-coding RNA (lncRNA) TEX41 regulates metastasis, which was partially dependent on autophagy (123). RUNX2's involvement in metastasis, a key cancer hallmark related to disease progression and poor outcomes, makes it an attractive target to study given that a broad range of cancers highly express RUNX2.

1.3.2.7 RUNX2 in fusion-driven cancers

RUNX2 has been identified in complex with 15 fusion gene pairs per the FusionGDB2 database hosted at the University of Texas Health Science Center at Houston (<https://compbio.uth.edu/FusionGDB2/index.html>), where fusion genes were validated or predicted from Entrez mRNA sequence libraries and human primary tumor samples of TCGA data from ChiTars 5.0 and ChimerDB 4.0. In osteoblastoma, a rare benign tumor of the bones, a *FOS::RUNX2* fusion gene was identified (124). A single case of squamous cell carcinoma reportedly harbored a *IRF2BP2::RUNX2* gene fusion that represented a keratocystoma, which is a very rare (<20 cases) tumor type (125).

Ewing's sarcoma demonstrates the importance of RUNX2 in fusion-driven cancers even when *RUNX2* is not part of the fusion oncogene. In Ewing's sarcoma, Li et al., found that the *EWSR1::FLI1* fusion protein directly binds Runx2 (126). This interaction is mediated by FLI1 sequences that bind with the Runt domain of Runx2. *EWSR1::FLI1-RUNX2* binding resulted in blocked osteoblast differentiation in a murine multipotent MSC cell line where Runx2 and *EWSR1::FLI1* were expressed. As mentioned in section 1.3.2.2, in primary bone cancer, an interaction between RUNX2 and YBX1 sustains a pro-metastatic niche (64,122). Studies about “YBX1, tRF-Gly^{TCC} and *RUNX2* led to the development of a RUNX2 inhibitor” (122), a

computer aided drug design molecule 522 (CADD522), which I will discuss further in section 1.3.3.

1.3.2.8 RUNX2 in RMS

The literature about RUNX2 in RMS is limited to two studies, one that explicitly mentioned RUNX2 (42) and another where RUNX2 was identified in a dataset in supplementary material (41). Coincidentally while I was working on RUNX2, the manuscript by Zhang et al. found that *RUNX2* is a high confidence gene target of PAX3::FOXO1 in Rh30 FP-RMS cells; furthermore, they identified that PAX3::FOXO1 binds a RUNX2 enhancer alongside known PAX3::FOXO1-associated transcription factors such as CDK8 and PAX3 (42). Using a PAX3::FOXO1 with a biotin ligase moiety fused in-frame, Zhang et al. found that RUNX2 is in the PAX3::FOXO1 protein interactome as well. Following the degradation of PAX3::FOXO1 using a dTAG-47 system, *RUNX2* expression decreased by 50% within 2 hours. When a *RUNX2* PAX3::FOXO1-regulated enhancer was deleted, *RUNX2* expression decreased and when a non-PAX3::FOXO1-regulated *RUNX2* enhancer was deleted, *RUNX2* expression still decreased. This suggests that each *RUNX2* enhancer element may serve independent functions that are necessary for maintaining the expression of *RUNX2* in FP-RMS. In summary, from this publication PAX3::FOXO1 is required to maintain open chromatin structure at the regulated enhancer regions of genes like *RUNX2*. In the second study by Gryder et al., the investigators aimed to identify the myogenic super-enhancers that PAX3::FOXO1 binds. Transcription factors such as MYOG, MYOD, and MYCN were explicitly identified in the text as being part of PAX3::FOXO1's myogenic super-enhancer circuitry (41). Interestingly, in Rh4 FP-RMS cells RUNX2 was also a PAX3::FOXO1 gene target. Despite these findings, no additional data interrogating the role of RUNX2 in FP-RMS has been published, and further investigation on RUNX2 is required to determine if it is indeed a potential FP-RMS therapeutic target.

1.3.3 Pharmacological approaches to RUNX2 inhibition

Transcription factors like RUNX2 have historically been viewed as ‘undruggable’ and ‘risky’ drug targets, but drugs targeting the protein both indirectly and directly are in the preclinical stage.

AI-14-91 was generated by John Bushweller, PhD. AI-14-91 directly binds CBF β rather than RUNX2. This molecule was identified after a study using 2-pyridyl benzimidazole AI-4-57 as a compound that binds to the CBF β portion of the CBF β -SMMHC fusion protein and screened from a library of structural analogs (127). Among the lead candidates, AI-14-91 had one of the lowest FRET IC₅₀ ratios. The concentration at which the FRET signal was cut in half for AI-14-91 was approximately 3 μ M, meaning that AI-14-91 can disrupt CBF β -Runt domain binding more efficiently than other analogs.

C₁₅H₁₃Cl₂NO₃, or CADD522, was screened from 1,1197 compounds aimed to interact with the Runt DNA-binding site identified using computer-aided drug design (CADD) and first tested in DNA binding assays where investigators determined that the EC₅₀ was 10nM (75,128-132). CADD522 was designed as a RUNX2-specific small molecule that has been tested *in vitro* as well as *in vivo*; its chemical structures can be found in Figure 11. Early reports found that CADD522 inhibited RUNX2-DNA binding and glucose uptake, downregulated CBF β , and reduced S451-RUNX2 phosphorylation, which decreases RUNX2’s ability to bind DNA and interact with CBF β (130). Interestingly, a follow-up study found that CADD522 can exert additional off-target effects (129). Kim et al., found that CADD522 interacts with the F1-ATP synthase complex and decreased the mitochondrial oxygen consumptive rate and ATP production in breast cancer (129). Most ATP synthase inhibitors exhibit unacceptable levels of toxicity; *in vitro* CADD522 concentrations up to 100 μ M for 72 hours did not cause cytotoxicity nor significant cell growth inhibition to normal cells (130). *In vivo*, CADD522 prevented tumor growth and metastasis and dosing up to 25 mg/kg five times per week for seven weeks did not

exhibit apparent toxicity (122,129,130). While CADD522 may have limitations due to its off-target effects, it holds therapeutic potential due to its ability to prevent tumor growth and metastasis without toxicity *in vivo*.

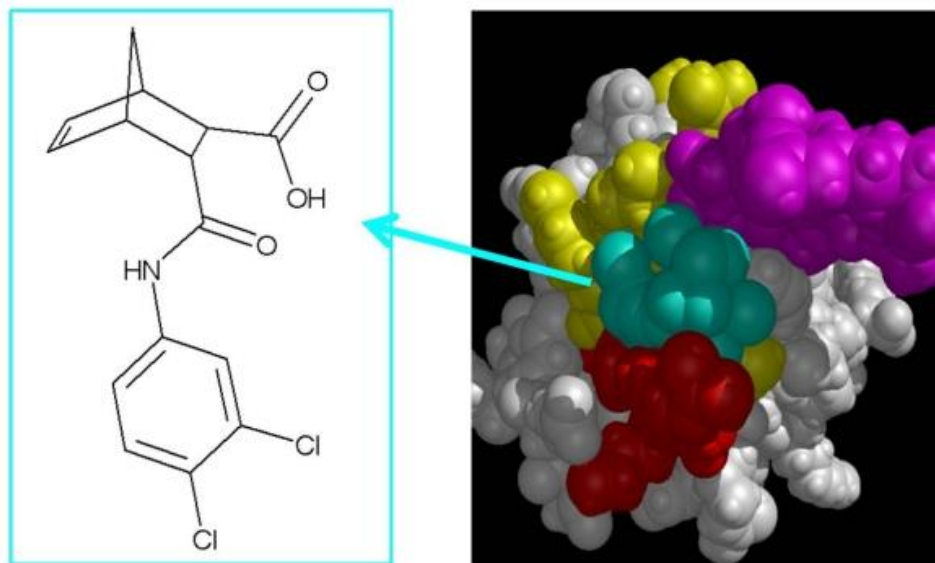


Figure 11: RUNX2-targeting compound CADD522 molecular structure.

The CADD522 compound was identified from a computer-assisted drug design screen of 1×10^6 compounds in its ability to ‘fit’ within the DNA-binding pocket of RUNX2, calculated from the Runt DNA binding domain X-ray crystal structure. CADD522 was validated in DNA binding assays to inhibit RUNX2 binding to its cognate DNA-binding domain. It exhibits an $IC_{50} = 10$ nM in D-ELISA DNA binding assays. In this depiction, Runt protein “tail” residues (purple), “wing” residues (red), and “base” residues (yellow) define a region of the protein that normally interacts with double-stranded DNA. Space-filling spheres (aqua) represent the position of DNA and the putative location of the inhibitor compound. Reprinted with permission under Creative Commons Attribution License from Brusgard JL, Choe M, Chumsri S, Renoud K, MacKerell AD Jr, Sudol M, Passaniti A. RUNX2 and TAZ-dependent signaling pathways regulate soluble E-Cadherin levels and tumorsphere formation in breast cancer cells. *Oncotarget*. 2015 Sep 29;6(29):28132-50. doi: 10.18632/oncotarget.4654. PMID: 26320173; PMCID: PMC4695049. Additional information for figure caption was obtained from (89).

1.4 Interactions between the RUNX family of transcription factors and the Hippo pathway

Both the Hippo pathway and RUNX family of transcription factors play vital roles in many processes such as proliferation, differentiation, apoptosis, tumorigenesis, and cell fate (52,53,133). RUNX1, RUNX2, and RUNX3 are capable of binding Hippo proteins at their

conserved domains (Figure 12). Most notably, RUNX2 is capable of binding YAP and TAZ at the PY motif of RUNX2 and the WW domains of YAP/TAZ (53,68,134). The interaction between RUNX2/YAP/TAZ can promote cell transformation, osteoblast differentiation (135-139), stem cell renewal (134), tumorsphere formation (134), tumorigenesis (136,140), chondrocyte differentiation/maturation (133,141), and EMT (75). Despite the abundance of studies about the Hippo pathway and RUNX2 in many cancers such as gastric cancer (136), breast cancer (75), and osteosarcoma (140), reports have demonstrated that TAZ promotes osteogenic differentiation by activating Runx2, while YAP represses Runx2-mediated transcription (135,142). Other Hippo proteins, such as MST2 and SAV1 are known to transcriptionally inhibit markers of osteogenic differentiation such as *Runx2* in C2C12 mouse myoblasts (138). Multiple reports have established a mechanistic connection between the Hippo pathway and RUNX2 and given the importance of the Hippo pathway in FP-RMS. Additional studies are needed to identify if these relationships are maintained in FP-RMS to determine FP-RMS therapeutic vulnerabilities.

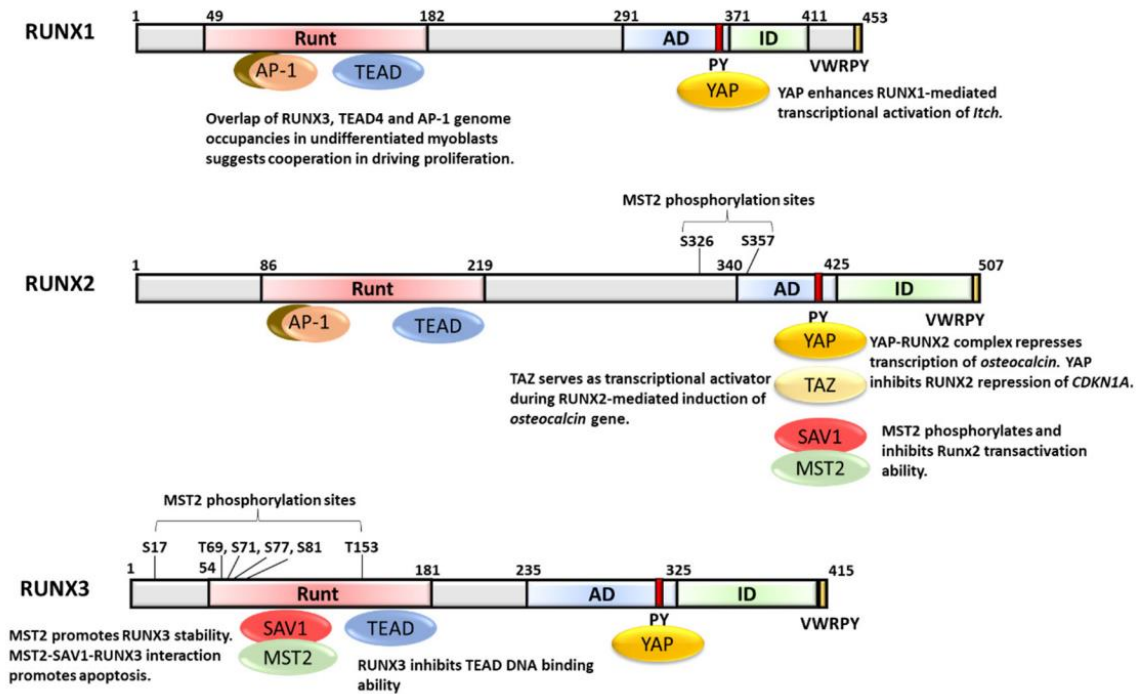


Figure 12: Conserved domains of human RUNX proteins and their interactions with Hippo associated proteins.

The numbers indicate amino acid positions in human RUNX1 (NP_001001890.1), RUNX2 (NP_001356334.1) and RUNX3 (NP_004341.1). For RUNX2, the corresponding MST2 phosphorylation sites in the longer RUNX2 isoform NP_001019801.3 are S347 and S378 (as stated in the text). Runt, AD and ID refer to the DNA binding, activation and inhibitory domains, respectively. Reprinted with permission under Creative Commons Attribution License from Chuang LSH, Ito Y. The Multiple Interactions of RUNX with the Hippo-YAP Pathway. *Cells*. 2021 Oct 28;10(11):2925. doi: 10.3390/cells10112925. PMID: 34831147; PMCID: PMC8616315.

2. Identifying a link between the Hippo pathway and RUNX2 in FP-RMS

When I joined the Linardic Lab, we were interested in studying the Hippo pathway in FP-RMS based on prior findings, as mentioned in Chapter 1. This section discusses my preliminary work and unbiased studies trying to carve out my own research direction in FP-RMS. This work laid the foundation for my primary work product on the role of RUNX2 in FP-RMS and is discussed in Chapter 3. The work presented here has not been published but has been vital to informing my next steps.

Some of the findings that I will share are my analyses of prior lab members' previously unpublished works that are important to conclusions drawn. Prior contributing lab includes Lisa Crose, PhD, Michael Deel, MD, Kristianne M. Oristian, PhD, and Katrina Slemmons, PhD. I would also like to acknowledge Derek Peters, MD PhD, YueYuan Xu, PhD, and Yarui Diao, PhD who assisted with ATAC-seq experiments and analysis.

Moving forward, I plan to adapt this text for a grant application, so that future experiments can be performed. After completing follow-up experiments and addressing gaps, we will submit a manuscript summarizing this work.

2.1 Introduction

To briefly summarize some of the information provided in Chapter 1, fusion-positive rhabdomyosarcoma (FP-RMS) is an aggressive pediatric cancer of skeletal muscle histogenesis and is associated with poor survival (13). Epigenetic dysregulation alters normal developmental networks to produce myoblast-like cells capable of sustained proliferation but not terminal differentiation (143). 60% of alveolar RMS (ARMS) cases express the fusion oncoprotein PAX3::FOXO1 (P3F) (13). Please note that throughout this chapter, I will refer to PAX3::FOXO1 as P3F rather than its full name, to simplify nomenclature. Clinical treatment has not changed since the 1970s and new therapies are desperately needed. Our laboratory has

investigated the role of P3F in FP-RMS to understand how it exerts its cancerous effects. To this end, we have developed models ranging from genetically manipulating human FP-RMS cell lines, developing new genetically engineered mouse models (GEMMs), and engineering normal primary human myoblasts to express oncogenes found in human FP-RMS tumors (9,26,51,54,56-58).

Using human FP-RMS cell lines, our lab found that P3F functions in part by restraining the Hippo tumor suppressor pathway, by binding to an upstream enhancer of *RASSF4* to increase its expression, which scaffolds and inhibits the Hippo (MST) kinase (54). Then, using a GEMM of FP-RMS (GEMM^{P3F}) with homozygous MST1/2 knockout (GEMM^{P3F+KO}), we demonstrated increased penetrance and earlier tumor onset upon MST inhibition (56). The resulting tumor-derived cell lines demonstrated a primitive phenotype, refractory to differentiation.

To better understand the role of MST1 loss-of-function we developed a third FP-RMS model: primary human skeletal muscle myoblasts (HSMM) were engineered to tumorigenic cells by expression of P3F, hTERT, and MYCN as described in (144). Importantly, HSMMs require hTERT and MYCN to be added sequentially following P3F in order for cells to be tumorigenic. We then developed a series of unbiased experiments to study the consequences of MST1 loss-of-function; these experiments included *in vivo* xenograft assays, phosphoproteomics analyses, and bulk ATAC-seq analyses (Figure 13).

The addition of dominant negative kinase-dead MST1K59R to P3F/hTERT/MYCN expressing HSMMs (abbreviated HSMM^{P3F+DN}) increased stemness *in vitro* and, increased tumor volumes paired with decreased latency *in vivo* compared to P3F/hTERT/MYCN cells with the addition of an empty vector (HSMM^{P3F+EV}). MST1 loss yielded tumor cells with an aggressive histologic appearance and increased stemness. Analysis of phosphoproteomics data from the isogenic HSMM model identified a cellular circuit of chromatin modifiers (HMGA1, NCL, LMNA, and TMPO) that were dysregulated due to the loss of MST1 function. Given these

findings, we hypothesized that the PAX3::FOXO1-RASSF4-MST1 signaling axis increased chromatin accessibility to support cancer cell stemness. Since MST1's tumor suppressor normally promotes chromatin condensation (145), we asked whether MST1-loss-of-function in our models supported a stemness state by increasing chromatin accessibility. We therefore performed bulk ATAC-seq. ATAC-seq motif enrichment analysis (MEA) of this model showed downregulation of motifs responsible for driving myogenic differentiation such as *MYOG*, *MYF5*, and *MYOD* and enrichment for *RUNX* motifs, which we hypothesized may be responsible for inhibiting myogenic differentiation in FP-RMS (73). After completing these unbiased screens, we further interrogated the role of *RUNX* transcription factors in FP-RMS, which led us to investigating *RUNX2* as a potential therapeutic target. These data can be found in Chapter 3.

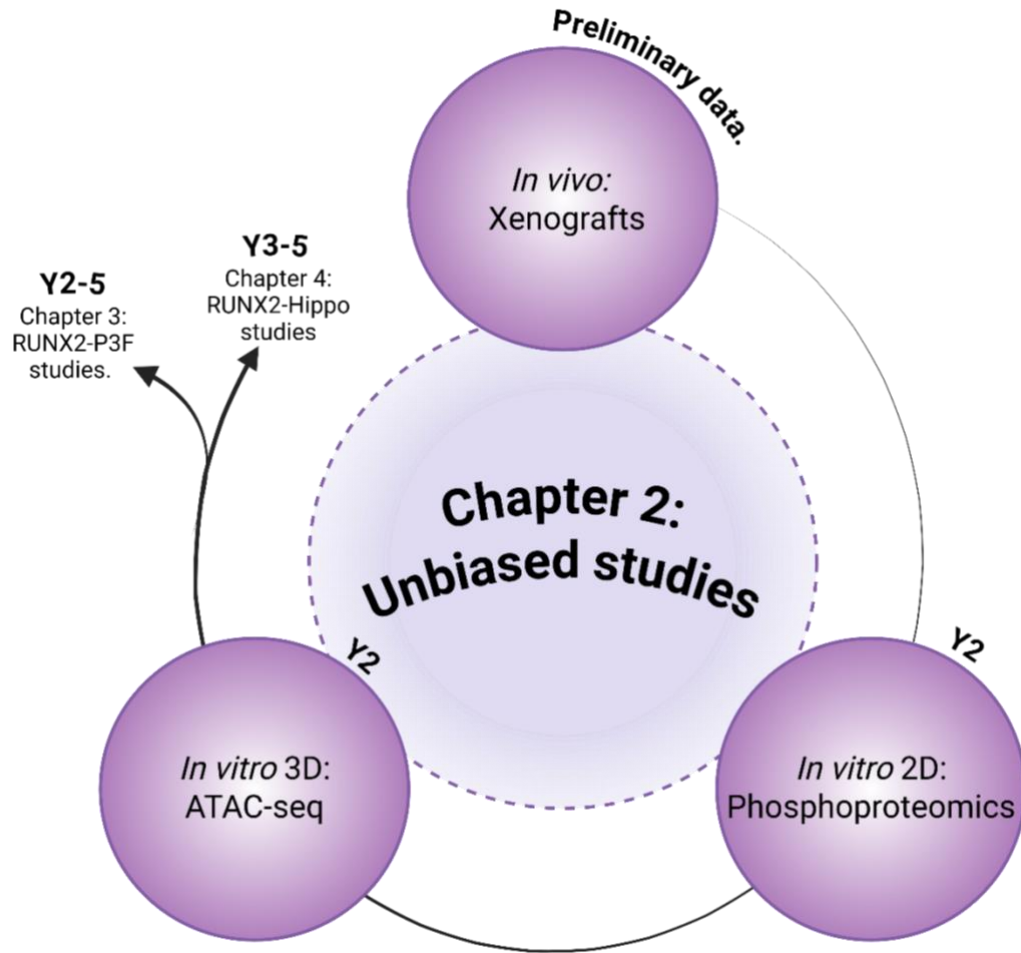


Figure 13: An unbiased approach to study MST1 inhibition in an isogenic HSMM model of FP-RMS.

A, Graphic of initial unbiased studies of the HSMM FP-RMS model cell lines. Preliminary data (Figure 14,15) included *in vivo* characterization of HSMM^{P3F+EV} which contains a constitutively active construct expressing P3F and an empty vector (EV), and HSMM^{P3F+DN} which contains a constitutively active construct expressing P3F and dominant negative MST1K59R (DN). These cell lines were created and validated by Lisa Crose, PhD and are further described in methods 2.2.1 and in (54). Lisa Crose, PhD performed Phosphoproteomics and mass spectrometry on HSMMs grown in normal 2D adherent culture conditions (Figure 16,17). I performed additional data analysis. Finally, I performed bulk ATAC-seq on HSMMs grown in 3D culture to enrich for stemness, harvested, and sequenced (Figure 18). These studies provided a foundation that allowed me to study RUNX2 in FP-RMS (Chapter 3) and begin initial studies on the mechanistic relationship between RUNX2, TAZ and P3F (Chapter 4). Created in BioRender. Mendes, E. (2025) <https://BioRender.com/zdrhdsn>.

2.2 Methods

2.2.1 Generation of cell lines and constructs

The human FP-RMS cell line Rh4 and Rh4-Flag were a gift from Dr. Beat Schaefer (36,146). Rh4-Flag harbors an endogenously tagged PAX3::FOXO1 with the Flag epitope at the C-terminus (36,146). Human FP-RMS cell lines Rh28 and Rh30 were gifts from Tim Triche (Children's Hospital of Los Angeles, Los Angeles, CA). For all studies, cells were imaged on a Leica DMI1 microscope and processed on Leica Application Suite Software. “Low-passage normal HSMMs from a teenage donor (Clonetics Cell Systems, Cambrex Corp., East Rutherford, NJ) were sequentially infected with amphotrophic retroviruses” as in (147); the cells were adapted from the genetically defined FP-RMS model developed by (147); and modified to stably express lentiviral vector (pLKO.1) or an MST1K59R kinase-dead mutant. Adherent 2D HSMMs were maintained with the SkGM-2 Skeletal Muscle Cell Growth Medium-2 BulletKit (Lonza, #CC-3245) per manufacturer’s protocol. Method for culturing 3D rhabdospheres of HSMMs was first described and can be found in (148).

2.2.2 Immunoblotting

Cell pellets were lysed with high detergent RIPA (Cell Signaling Technology, #9806S) and Halt™ protease and phosphatase inhibitor cocktail (Thermo Fisher Scientific, #78442) then passaged through a 21-gauge needle for optimal shearing of DNA. Protein concentration was measured using the protein assay dye reagent concentrate (Bio-Rad, #500006). 4X protein Sample loading buffer (Thermo Fisher Scientific, #LC2570 and #NP0007) was combined with 20% β-mercaptoethanol and then added to protein samples and then lysates were boiled for five min at 95°C. 20 μg of lysate was loaded onto 4%-15% gradient Mini-PROTEAN precast gel (Bio-Rad) and resolved with SDS-PAGE and then transferred to Immobulin-FL polyvinylidene difluoride membrane (Millipore, #IPFL00010). Membranes were immunoblotted with primary monoclonal antibodies P-MOB1 (Cell Signaling Technology, #8699) and anti-β-ACTIN (Cell

Signaling Technology, #4970) and polyclonal antibodies MST1 (Cell Signaling Technology, #3682) and MOB1 (Cell Signaling Technology, #3863). Membranes were reacted with an anti-rabbit secondary antibody and then imaged by enhanced chemiluminescence on the Chemi-Doc (Bio-Rad). Depending upon protein abundance, West Pico PLUS (Thermo Fisher Scientific, #34580) or West Atto Ultimate Sensitivity (Thermo Fisher Scientific, #A38556) substrates were used and imaged at various exposures according to manufacturer protocol.

2.2.3 *In vivo* xenograft assays

Xenograft studies utilized 8×10^6 cells (HSMM^{P3F+EV} and HSMM^{P3F+DN}) resuspended in growth factor replete Matrigel (BD Biosciences, #354234) and implanted subcutaneously into the flanks of immunodeficient SCID/*beige* mice. Tumors were grown for 20 days once palpable. Tumors were measured 3 times weekly using calipers and tumor volume calculated as $[(\text{width} \times \text{length})/2]^3/2$. Institutional Animal Care and Use Committee (IACUC)-defined maximum tumor burden which was established as tumors measuring >15 mm in one direction, >12 mm in two directions, or decline in health rather than at a single timepoint for survival analyses. Portions of tumors were preserved in formalin-fixed and paraffin-embedded (FFPE) for immunohistochemistry or flash frozen in liquid nitrogen for later use.

2.2.4 Hematoxylin and Eosin

For xenograft hematoxylin and eosin (H&E) staining, paraffin-embedded sections were deparaffinized in xylene, rehydrated through graded ethanols, and then submerged into hematoxylin. Next, samples were submerged in water, clearing solution, water, bluing solution, water, eosin, dehydrated through graded ethanols, and xylene.

2.2.5 Phosphoproteomics

Phosphoproteomics experiments were performed by the Proteomics and Metabolomics Core Facility with cells prepared by Lisa Crose, PhD. Results were analyzed by Lisa Crose, PhD and myself, independently.

2.2.5.1 Growing HSMM^{P3F+EV} and HSMM^{P3F+DN} cells in preparation for phosphoproteomics

HSMM^{P3F+EV} and HSMM^{P3F+DN} cells were grown in SkGM-2 media on 15 cm tissue culture plates. 3.25×10^6 cells were used for each replicate. Samples were run in quadruplicate. Pellets were washed in dPBS before proceeding to 2.2.5.2.

2.2.5.2 TiO₂ phosphoproteomics and mass spectrometry

500 μ L of 0.2% Rapigest (Waters) in 50 mM ammonium bicarbonate was added to each cell pellet samples followed by three rounds of probe sonication for cell lysis and protein solubilization. Lysates were subjected to Bradford assays and then 1.2 mg was removed for digestion. Samples were reduced with 5 mM dithiothreitol for 30 min at 70°C and alkylated with 10 mM iodoacetamide for 45 min at room temperature. Proteolytic digestion was accomplished by the addition of 25 μ g sequencing grade trypsin (Promega) with incubation at 37°C for 18 hours. Supernatants were collected following a 2 min centrifugation at 1,000 rpm, acidified to pH 2.5 with TFA and incubated at 60°C for 1 h to hydrolyze remaining Rapigest surfactant. Samples were then lyophilized to dryness and phosphopeptides were enriched using GL Biosciences p10 TiO₂ derivatized tips according to manufacturer protocols. Extracted peptides were lyophilized to dryness and resuspended in 12 μ L of 0.2% formic acid/2% acetonitrile.

Each sample was subjected to chromatographic separation on a Waters NanoAquity UPLC equipped with a 1.7 μ m BEH130 C₁₈ 75 μ m I.D. X 250 mm reversed-phase column. The mobile phase consisted of (A) 0.1% formic acid in water and (B) 0.1% formic acid in acetonitrile. Following a 4 μ L injection, peptides were trapped for 3 min on a 5 μ m Symmetry C₁₈ 180 μ m I.D. X 20 mm column at 5 μ L/min in 99.9% A. The analytical column was then switched in-line and a linear elution gradient of 5% B to 40% B was performed over 90 min at 400 nL/min. The analytical column was connected to a fused silica PicoTip emitter (New Objective, Cambridge, MA) with a 10 μ m tip orifice and coupled to a Waters Synapt HDMS mass spectrometer through an electrospray interface operating in a data-dependent mode of acquisition. The instrument was

set to acquire a precursor MS scan from m/z 375-1675 with MS/MS spectra acquired for the ten most abundant precursor ions. For all experiments, CID energy settings were 27v and a 120 s dynamic exclusion was employed for previously fragmented precursor ions.

2.2.5.3 Phosphoproteomics and mass spectrometry analysis

Raw LC-MS/MS data files were processed in Rosetta Elucidator and then submitted to independent Mascot searches (Matrix Science) against a SwissProt Human database containing both forward and reverse entries of each protein. Search tolerances were 10 ppm for precursor ions and 0.02 Da for-product ions using trypsin specificity with up to two missed cleavages. Carbamidomethylation (+57.0214 Da on C) was set as a fixed modification, whereas oxidation (+15.9949 Da on M), and phosphorylation (+79.99 Da on STY) were considered dynamic mass modifications. Scoring thresholds achieved a 1% FDR. Label free quantitation was performed with Elucidator with a summing function of all independent precursors to the same modified peptide. Phosphopeptides were subjected to a trim mean normalization across all detectable phosphopeptides.

2.2.6 ATAC-seq

ATAC-seq was completed with the help of Derek Peters, MD PhD, Xiaolin Wei, PhD, and Yueyuan Xu, PhD in the lab of Yarui Diao, PhD. The ATAC-seq sample preparation and analysis pipeline were followed according to the Encyclopedia of DNA Elements (ENCODE) standards (<https://www.encodeproject.org/>). Detailed steps are outlined in 2.2.6.1 and 2.2.6.2. Please note that Tn5 purification and transposase assembly methods used for chromatin proximity ligation were as in Wei et al. (149).

2.2.6.1 Growing HSMM^{P3F+EV} and HSMM^{P3F+DN} cells in preparation for bulk ATAC-seq

1. Low population doubling (PD+2) HSMM^{P3F+EV} and HSMM^{P3F+DN} cells were each grown up in 12 x 10 cm plates using SkGM-2 to yield $\sim 1.2 \times 10^8$ million cells.

2. To generate spheres, 5×10^5 cells were plated into each well of ultra-low attachment 6-well plates using rhabdosphere media as described in (148). Each well yielded $\sim 2.5 \times 10^5$ cells in spheres.
3. To generate enough cells for ATAC-seq, seed 8 wells of 2, 6-well plates to generate enough cells of each condition for a $n=3$.
4. Wash cells in dPBS and use fresh or thaw frozen live cells that were previously grown (not recommended for sphere assays).

2.2.6.2 Bulk ATAC-seq protocol (created by the Diao lab).

Nuclei Preparation:

1. Collect fresh cells or thaw frozen cells.
2. Count cells and distribute 2×10^4 cells into 1.7 mL tubes. Use a single tube for each replicate. Count using a hemocytometer.
3. Centrifuge cells at 500xg for 5 min, discard supernatant, retain cell pellet and about 20 μL in each tube.
4. Add 490 μL of nuclei permeabilization buffer (NPB) and 10 μL of 50X protease inhibitor cocktail (EDTA-free). Do not pipet.
5. Rotate at 4°C for 15-20 min.
6. Centrifuge at 1000xg for 5 min at 4°C. Discard supernatant and leave approximately 10 μL of liquid in each tube.
7. Add 40 μL of 1.11X tagmentation buffer (TB) and 10 μL of 2X TB for a total volume of 60 μL . Vortex briefly, do not pipet.
8. Centrifuge cells at 500xg for 5 min, discard supernatant, retain cell pellet and about 20 μL in each tube.

Tagmentation and Library Generation:

9. Add 0.2 μL of Tn5 to each tube.

10. Centrifuge cells at 500xg for 5 min, discard supernatant, retain cell pellet and about 20 μ L in each tube.
11. Vortex for 10 s. Incubate at 37°C 500-900 RPM in the thermomixer for 1 h.
12. Add 300 μ L DNA binding buffer (Zymo, 5X). Optional: OK to store at -20°C before proceeding.

Dissociate Tn5:

13. Purify $\frac{1}{2}$ of the total volume using the Zymo clean and concentrate kit.
 - a. Transfer to Zymo volume. Spin 12,000 RPM for 20 s in benchtop centrifuge. Discard flowthrough.
 - b. Wash with 200 μ L wash buffer, twice. On the last wash spin for 1.5 min as in a.
 - c. Transfer column to 1.7 mL tube. Add 15 μ L of tris 10 mM pH8 directly to the column (warm tris at 55°C for a few minutes before adding).
 - d. Wait for a few minutes before eluting.
 - e. Centrifuge for 1.5 min to elute.

PCR:

14. Set up a PCR reaction. Use a unique combination of Nextera i5/i7 primers (10 μ M) for each sample.
 - a. Template DNA – 7.5 μ L, 5X Q5 buffer – 5 μ L, 10 mM dNTP – 0.5 μ L, i7 – 0.625 μ L, i5 – 0.625 μ L, Q5 polymerase – 0.25 μ L, water – 10.5 μ L for a total of 25 μ L.
15. Run PCR.
 - a. 72°C – 5 min, 98°C – 10 s, (98°C 10 s, 60°C – 30 s, 72°C – 50 s) 13 cycles. May need to do an extra cycle. 72°C 7 min.
16. Check PCR products on a 1.2% flashgel from Lonza. Use 1 μ L of ladder and 1 μ L of PCR products (3 samples and 1 negative control).

17. Gel extract bands using Zymo gel extraction kit. Elute in 20 μ L 10 mM tris pH 8.
18. Measure DNA concentration using Qubit and check 1 μ L of sample on flashgel. Samples can be frozen in DMSO.
19. Samples are then sequenced on the Illumina platform. Approximately 100M reads were mapped per sample, but depth can be as low as 20M in future experiments.

2.2.7 Quantitative real time PCR

RNA was isolated from cell pellets stored at -80°C using a RNeasy Mini Kit (Qiagen, #74106) according to manufacturer specifications. Conversion to cDNA was completed using the Omniscript RT kit (Qiagen, #205113). Quantitative real-time PCR (qRT-PCR) was performed using the SYBR Green system (Bio-Rad) according to manufacturer specifications. Primer sequences for RUNX2 FWD 5' CCAAATTTGCCTAACCAGAA 3' and REV 5' GCTCGATTGCAATTGTCTCT 3', and GAPDH FWD 5' GAGAGACCCTCATTGTTG 3' and REV 5' GATGGTACATGACAAGGTGC 3'. Each biological experiment was run in triplicate. Technical and/or biological replicates are specified in figure legends.

2.2.8 Statistics

Please refer to section 3.3.17.

2.3 Results

2.3.1 HSMMP^{3F+DN} tumors exhibit decreased latency compared to HSMMP^{3F+EV}

To investigate the role of MST1/2 *in vivo*, Oristian et al. developed a GEMM of FP-RMS as described in section 1.2.2. In addition to this model, Lisa Crose, PhD and Kristianne Oristian, PhD engineered HSMM models to tumorigenic cells by expression of P3F and cooperating oncogenes as described (54,144,147), then added a dominant negative kinase-dead MST1K59R (HSMMP^{3F+DN}) (Figure 14). MST1K59R prevents MST1 ATP binding and results in the loss of

MST1 autophosphorylation. Next, to confirm that MST1K59R was expressed and kinase-dead, we performed an immunoblot for MST1, P-MOB1, and MOB1 (Figure 15A). We examined P-MOB1 rather than P-MST1 determine that the construct was expressed and functioning (150). When MST1K59R was expressed, we found that MST1 expression increased and P-MOB1 expression was lost, meaning that Hippo signaling downstream of MST1 was lost (Figure 15A). Cells were then injected into the flanks of SCID/*beige* mice to investigate *in vivo* oncogenic phenotypes (Figure 15B-E). Tumors expressing MST1K59R demonstrated decreased tumor latency compared to HSMMP^{P3F+EV} control tumors (Figure 15B). MST1K59R expression resulted in nuclear dimpling, a morphologic change often attributed to a more euchromatic or ‘open’ chromatin state (151) (Figure 15C). Representative H&E of HSMMP^{P3F+DN} tumors were analyzed by pathologist Rex Bentley, MD who found that tumors expressing MST1K59R appeared more aggressive, and primitive given their lack of myotubes and larger nuclei (Figure 15D). Because this experiment was a pilot from more than 10 years ago, complete quantification and HSMMP^{P3F+EV} H&E is unavailable. To be submitted for publication, this experiment will need to be repeated so that appropriate controls can be included.

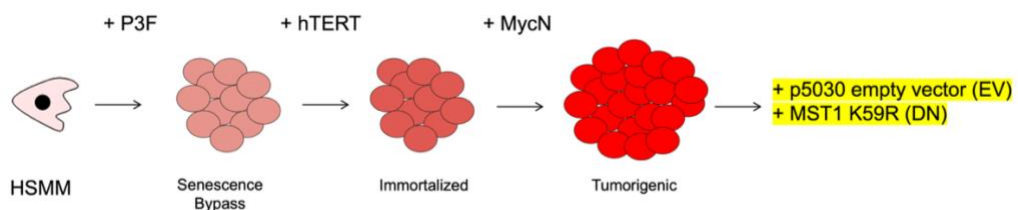


Figure 14: HSMMP^{P3F+EV} and HSMMP^{P3F+DN} cell line derivation.

Prior work demonstrated when P3F is exogenously expressed in HSMMS cells bypass senescence. When hTERT is expressed in HSMMS, cells are immortalized. When MycN is expressed, cells become tumorigenic. When MST1K59R is expressed, MST1 is unable to perform its tumor suppressive function because of the K59R mutation that renders MST1. ‘kinase dead’. Names are shorted to HSMMP^{P3F+EV} and HSMMP^{P3F+DN} for figure clarity.

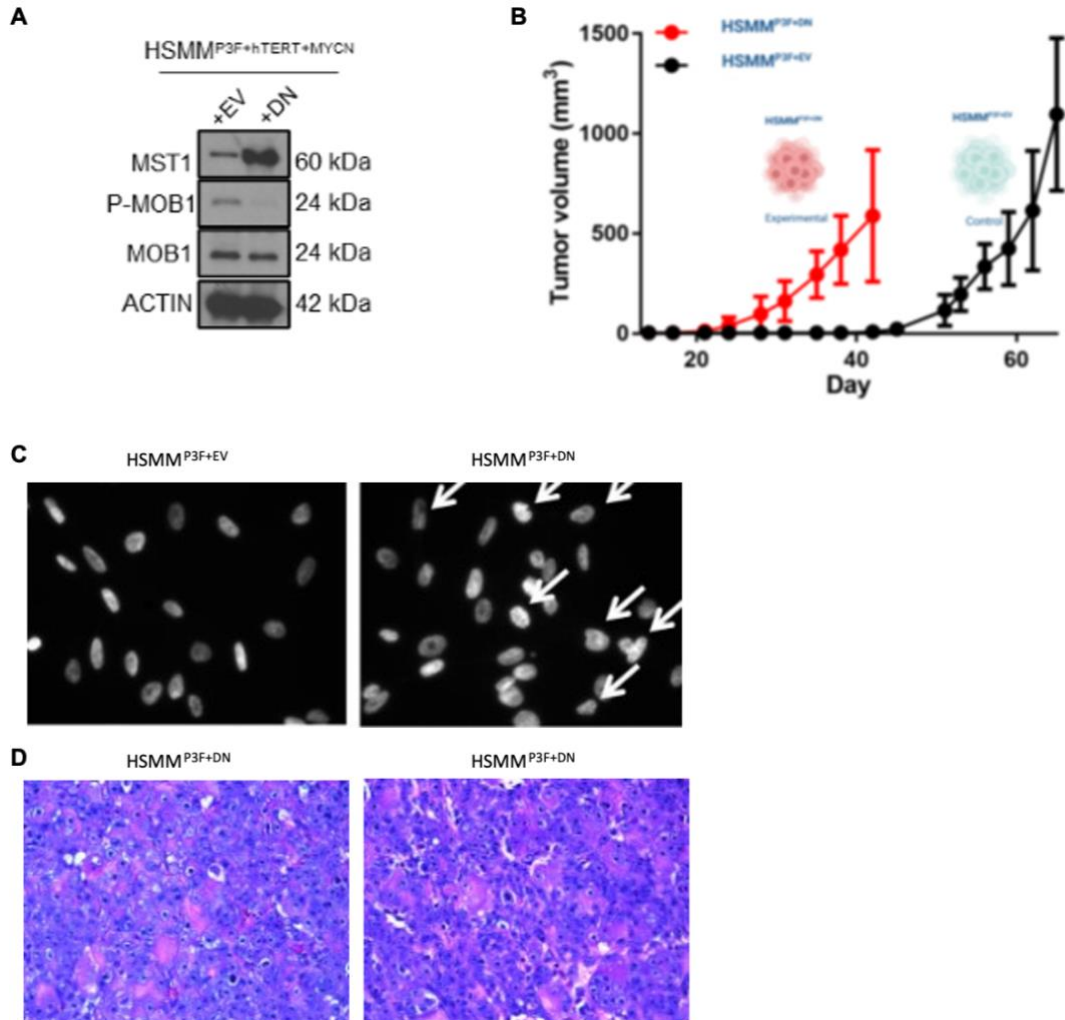


Figure 15: Characterization of isogenic primary human myoblast cells harboring MST1 loss-of-function.

HSMMs expressing P3F/hTERT/MYCN and EV or MST1K59R were injected into the flank of SCID/Beige mice. **A**, Immunoblot for MST1, P-MOB1, MOB1, and ACTIN protein expression in HSMMP^{3F+EV} and HSMMP^{3F+DN}; cells were engineered by Lisa Crose, PhD. **B**, Tumor volume growth curves in mice engrafted with HSMMP^{3F+EV} (n=6) or HSMMP^{3F+DN} (n=6). Experiment performed by Lisa Crose, PhD. **C**, Light microscopy of HSMMP^{3F+EV} (left) and HSMMP^{3F+DN} (right). White arrows point to areas representative of nuclear dimpling. Images were taken by Lisa Crose, PhD. **D**, Representative H&E of HSMMP^{3F+DN} tumors. Images of excised tumors taken at 40X magnification. H&E of HSMMP^{3F+EV} is unavailable and needs to be repeated before publication.

2.3.2 Phosphoproteomics approach to identify cellular circuits altered by MST1 loss-of-function

To better understand the molecular changes that occur because of MST1 loss-of-function, we performed phosphoproteomics of HSMM^{P3F+EV} and HSMM^{P3F+DN} cells grown in 2D culture. We hypothesized that changes would be manifest in a phosphoproteomics assay, since MST1 is a kinase. Using a +1 fold change (FC) criterion and *p*-value cut off of 0.01, I generated a list of phosphoproteins that were upregulated or downregulated upon MST1 loss-of-function (Figure 16). To further narrow hits, we used a *p*-value cutoff of 0.01 and proceeded with STRING analysis (Figure 17A); the inset shows proteins with changes significant to *p*<0.005 (Figure 17A). Four proteins, HMGA1, NCL, LMNA, and TMPO were identified and are all involved in regulating chromatin and or nuclear structure. Implicated residues and their changes in phosphorylation in response to MST1 loss of function can be found in Figure 17B.

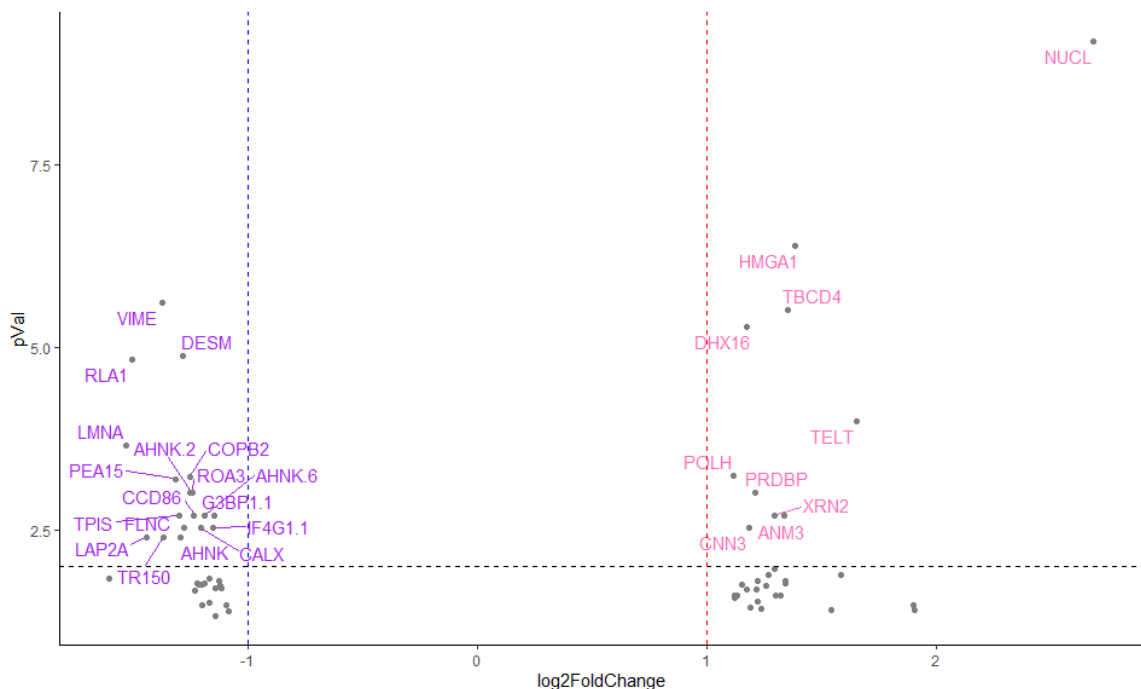


Figure 16: Top proteins hits exhibiting changes in phosphorylation in response to MST1 loss following TiO₂ enrichment and mass spectrometry.

197 differentially expressed proteins identified following TiO2 enrichment and mass spectrometry. Top hits are visualized using ggplot2 HSMM^{P3F+EV} (n=4) and HSMM^{P3F+DN} (n=4).

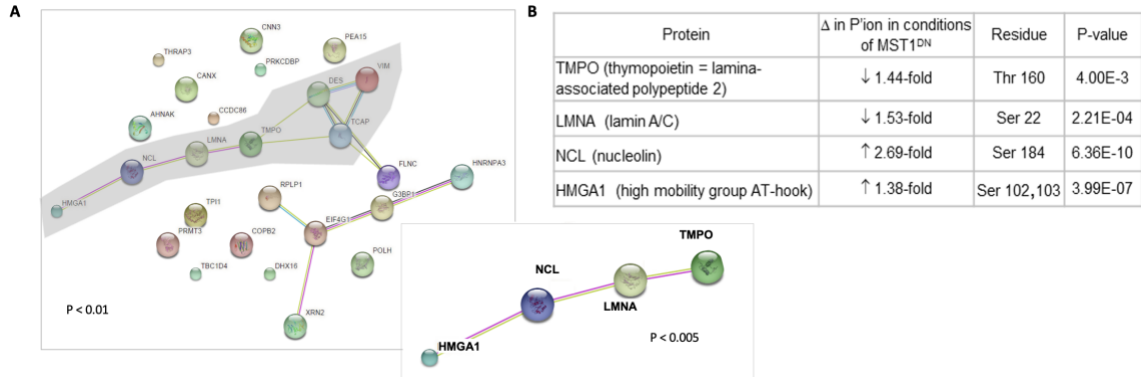


Figure 17: Feasibility of using a phosphoproteomics approach to identify cellular circuits altered by MST1 loss-of-function.

A, STRING analysis of proteins exhibiting changes in phosphorylation in response to MST1 loss of function ($P < 0.01$). Inset shows proteins with changes significant to $P < 0.005$. B, Implicated residues and their changes in phosphorylation in response to MST1 loss of function. HSMM^{P3F+EV} (n=4) and HSMM^{P3F+DN} (n=4) Figure adapted from Lisa Crose, PhD.

2.3.3 *RUNX2* motifs are enriched when MST1 activity is inhibited in HSMM^{P3F+DN} cells expressing P3F, hTERT, MYCN, and MST1K59R

Since MST1's tumor suppressor activity normally promotes chromatin condensation during apoptosis (145), and since our pilot phosphoproteomics experiment revealed a string of proteins involved in altering nuclear morphology as described in section 2.3.2 we hypothesized that MST1 loss of function would result in genomic changes that could be identified by open/closed regions. Thus we performed ATAC-seq to determine whether MST1-loss of function in our models supported a less differentiated state by altering chromatin accessibility (Figure 18). To gain better insights about the 3D signaling environment that may influence cell state, we grew cells in a 3D rhabdosphere culture system (148) to enrich for stemness before extracting DNA to perform ATAC-seq. Following ATAC-seq, we performed motif enrichment analysis (MEF) (152) and identified regions of DNA with increased/decreased accessibility. Next, we analyzed the differences between HSMM^{P3F+DN} and HSMM^{P3F+EV} cell lines and discovered that HSMM^{P3F+DN}

cells were depleted in myogenic motifs (Figure 18A, top) and enriched for RUNX motifs (Figure 18A, bottom). To further characterize the genes identified from MEF, we performed gene ontology (GO) analysis (153) to group hits into biological categories and identify what processes were changed following MST1 loss-of-function (Figure 18B). Several identified GO categories were related to muscle differentiation and development, suggesting that MST1 loss-of-function impacts cell state, potentially to make FP-RMS cells more primitive and less differentiated. WE noted the upregulation of *RUNX* motifs and downregulation of the expression of motifs responsible for driving myogenic differentiation. Given the availability of small molecule inhibitors to RUNX2, and RUNX2's known role as a regulator of differentiation as described in Chapter 1, we first interrogated its expression in our isogenic cell lines (129,154). To determine whether accessible *RUNX* motifs were transcribed into RNA, we performed qRT-PCR and found that *RUNX2* expression was 10-fold higher in HSMM^{P3F+DN} cells (Figure 18C). Our subsequent deep dive into the role of RUNX2 in FP-RMS is found in section 1.3.2.8 and in Chapter 3.

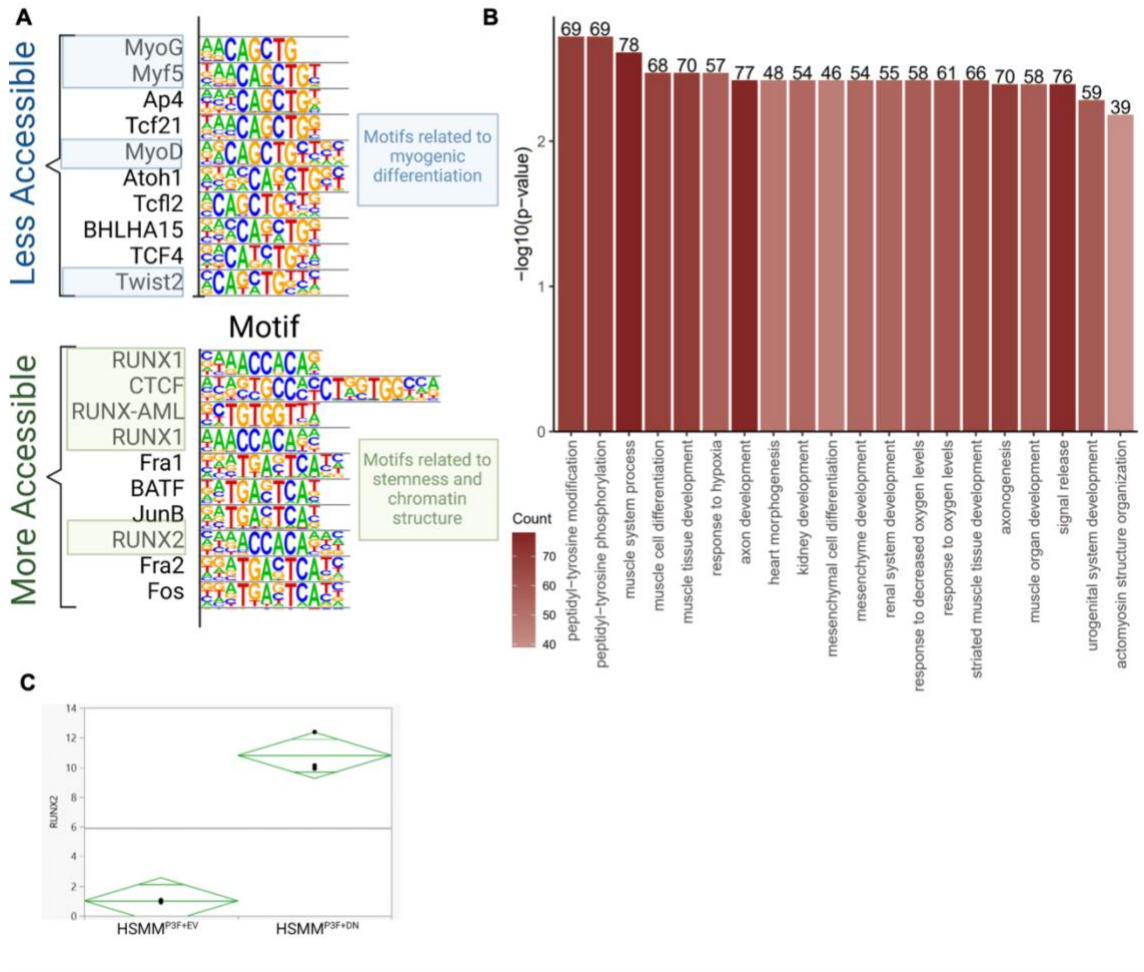


Figure 18: Bulk ATAC-seq of HSMMP3F+DN versus HSMMP3F+EV.

A, Motif enrichment analysis (MEA), top 10 most accessible and least accessible hits ranked by p -value. **B**, Gene ontology (GO) analysis of biological processes when comparing HSMMP3F+DN ($n=3$) to HSMMP3F+EV ($n=3$). Gene counts are listed above each biological process and represent how many genes of interest are associated with the corresponding category. The y-axis denotes the $-\log_{10}(p\text{-value})$ for each GO term. **C**, qRT-PCR for *RUNX2* using RNA from HSMMP3F+DN and HSMMP3F+EV normalized to *GAPDH*. Each dot represents biological replicates.

2.4 Discussion

Children with FP-RMS need new therapies. Our lab's first inkling that P3F restrained the Hippo pathway was demonstrated in human FP-RMS cell lines, and these studies put forth the P3F/RASSF4/MST axis and the idea that one of P3F's function was to inhibit MST activity (54,56). To follow up on these studies, we developed a P3F-GEMM (P3F GOF and Ink4a/ARF

loss-of-function) in which MST1/2 was deleted from the genome (56). In this study, we investigated MST loss-of-function in genetically defined *human* cells. We used our previously established HSMM-based model (147) of FP-RMS in which stable expression of P3F in HSMMs transforms them into tumorigenic cells mimicking FP-RMS. Using this model, we were able to more carefully examine MST1 activity, and study what happens when it is lost without affecting the expression of endogenous MST2 directly (Figure 15A). When we characterized this model *in vivo*, we found that tumors exhibited decreased latency compared to tumors expressing P3F, hTERT, MYCN, and an empty vector (Figure 15B). Next, we studied the effects of MST1 loss-of-function and found that MST1 inhibition led to the upregulation of phosphopeptides related to chromatin organization, which led us to perform ATAC-seq of HSMM rhabdospheres to better understand changes in chromatin accessibility (Figure 16 and Figure 17).

2. Acknowledgements

We thank the Duke University School of Medicine for the use of the Proteomics and Metabolomics Core Facility, which provided a TiO₂ enrichment for phosphopeptides service. We thank *Derek Peters, MD PhD, YueYuan Xu, PhD, and Yarui Diao, PhD* who assisted with ATAC-seq experiments and analysis.

3. RUNX2 inhibition disrupts a PAX3::FOXO1-RUNX2 feed-forward loop and dismantles oncogenic gene programs in FP-RMS

This section, including figures, was adapted from Mendes EA, Munshi A, Singh A, Evans MD, Chou HC, Kim YY, Song Y, Jo A, Lee D, Ciampi J, Chambers A, Weitzel S, Deel M, Bentley RC, Khan J, Green D, Linardic CM. RUNX2 inhibition disrupts a PAX3::FOXO1-RUNX2 feed-forward loop and dismantles oncogenic gene programs in fusion-positive rhabdomyosarcoma. bioRxiv [Preprint]. 2025 Jul 24:2025.07.21.665972. doi: 10.1101/2025.07.21.665972. PMID: 40777370; PMCID: PMC12330556.

It was written primarily by Elizabeth A. Mendes with revisions from Corinne M. Linardic, Javed Khan, and Darrell Green and uploaded to pre-print under Open Access, which allows authors to retain Copyright and permits authors of articles to use their article or parts of their article without restriction provided that reproductions and/or adaptations receive permission from the author (myself).

3.1 Significance

RUNX2 inhibition reduces PAX3::FOXO1 expression and signaling, which impairs fusion-positive rhabdomyosarcoma oncogenic phenotypes. *In vivo* treatment with CADD522 decreased tumor growth and increased survival, indicating that RUNX2 is a promising therapeutic target.

3.2 Introduction

Rhabdomyosarcoma (RMS) is the most common soft tissue sarcoma of childhood and adolescence, characterized by the expression of skeletal muscle markers (9). Current World Health Organization criteria subclassifies RMS by additional histopathologic features into four types: embryonal RMS (ERMS), alveolar RMS (ARMS), spindle cell/sclerosing RMS (SCRMS), and pleomorphic RMS (PRMS) (155). ERMS and ARMS are the most common, and now

classified molecularly based on the absence (fusion-negative RMS; FN-RMS) or the presence (fusion-positive RMS; FP-RMS) of the PAX3/7::FOXO1 fusion oncogene, respectively. Despite these molecular advances, high risk RMS still portends a five-year overall survival of less than 30%, and metastatic RMS of less than 8% (13). Despite decades of research, the standard chemotherapy protocol for RMS remains vincristine, actinomycin D, and an alkylator such as cyclophosphamide or ifosfamide, drug combinations discovered in the 1970s. New therapies are desperately needed (14,15).

FP-RMS represents a disproportionately high percentage of high-risk RMS cases. The oncogenic driver of FP-RMS is PAX3::FOXO1, a chimeric transcription factor generated from the stable reciprocal translocation of chromosomes 2 and 13. PAX3::FOXO1 impairs myogenic differentiation via epigenetic dysregulation that produces myoblast-like cells capable of sustained proliferation but not terminal myogenic differentiation (35,143). Despite its role as an oncogenic driver, PAX3::FOXO1 is refractory to therapeutic targeting due to its lack of catalytic activity, and its intrinsically disordered structure, which leaves few pockets to bind small molecules (35,40,41). However, the transcriptional programs driven by PAX3::FOXO1 may yield alternate therapeutic targets. For example, prior work identified a PAX3::FOXO1 activated myogenic super-enhancer landscape that maintains the myoblastic state (41,42), including *MYCN* and *MYOD1* (41-44), and these are being evaluated as drug targets (46,156).

Here, we have taken a broad view of RMS to nominate additional members of this network that may be more amenable to clinical targeting. Using messenger (mRNA) sequencing data of primary patient tumor tissue, we compared the four histopathologic types of RMS, and with the DepMap resource, prioritized the transcription factors participating in this network. At the top of our list was RUNX2, a transcription factor previously identified as a PAX3::FOXO1 downstream target and part of the PAX3::FOXO1 interactome (41,42), but which has not been

evaluated as a therapeutic target in FP-RMS. Remarkably, this transcription factor also emerged as a top candidate from our prior unbiased ATAC-Seq studies (Chapter 2).

RUNX2 is a member of the RUNX family (RUNX1, RUNX2, RUNX3) that is defined by a DNA-binding runt domain, and which largely operates as part of a heterodimeric core binding factor (CBF) complex with core binding factor-beta (CBF β) to enhance DNA binding capacity (84,85). RUNX2 is best known for its essential role in the differentiation of mesenchymal stem cells (MSCs) into osteoblast and chondrocyte lineages. *RUNX2* transcription is regulated by two promoters, P1 and P2, with both isoforms expressed in osteoblast-lineage cells and chondrocytes, but expression is largely regulated by enhancers, which remain to be elucidated (84,85). RUNX2 is a master regulator and organizer, working in tandem alongside other transcription factors and co-factors (86). RUNX2 also has roles in the differentiation of bipotent MSCs into myotubes and osteogenic cells (87), but these are less well understood.

Here, we investigated the phenotypic consequences of RUNX2 inhibition in FP-RMS, the mechanism by which RUNX2 promotes downstream PAX3::FOXO1 signaling, and evaluated the consequences of RUNX2 inhibition *in vivo*. Using both genetic and pharmacological inhibition of RUNX2 *in vitro* and *in vivo*, we found that RUNX2 is essential to maintaining a proliferative FP-RMS cell state, while preventing apoptosis and terminal myogenic differentiation. Mechanistically, RUNX2 and PAX3::FOXO1 reciprocally regulate one another in a feed-forward loop to drive transcription of downstream PAX3::FOXO1 targets. Our findings suggest that directly inhibiting RUNX2 phenocopies PAX3::FOXO1 suppression and highlights its role as a legitimate druggable driver of oncogenic phenotypes in FP-RMS.

3.3 Materials and methods

3.3.1 Patient samples

The University of East Anglia Faculty of Medicine and Health Science Research Ethics Sub-Committee prospectively approved the collection and study of human RMS samples (ref:

ETH2324-1212). Archived fresh frozen patient derived tissue samples (n=26) were obtained from the Royal Orthopaedic Hospital NHS Foundation Trust Research Tissue Bank (IRAS ID: 289182; REC ref: 22/EM/0042), which is a specialist tertiary hospital for sarcoma surgical management. Prior to tissue banking, a consultant histopathologist confirmed RMS histological interpretation using World Health Organization guidelines. This project included ARMS (n=5), ERMS (n=4), SCRMS (n=3), PRMS (n=1) and wildtype (control) skeletal muscle tissues (SkM) (n=13). All individuals provided written informed consent to donate their tissue for research. Patient demographics are summarized in Table 5 which can be found on the next two pages.

Table 5 Patient Sample Demographics and Histological Interpretations.

Patient tissue bank identification (ID), histology ID, sample ID, demographics, and previous treatments. Continued onto the next page.

Tissue bank ID	Histology ID	Sample ID	Sex	Age (y)	Histological interpretation	Neoadj. chemo (Y/N)
12073	9-0877	R01_T	F	13	ARMS; right arm	Y
18138	13-2973	R02_T	F	54	ARMS; right arm	Y
14780	10-0947	R05_T	M	4	ARMS; right foot	Y
23235	17-1668	R06_T	F	72	SCRMS; right thigh	N
25802	19-0966	R07_T	M	10	ERMS; right thigh	Y
8452	0556/06	R08_T	M	10	ARMS; right foot	Y
7587	1579/06	R09_T	F	12	ERMS; right groin	Y
7587	1579/06	R09_T	F	12	ERMS; right groin	Y
7944	0987/06	R10_T	M	20	ERMS; right leg	Y
5861	2478/04	R11_T	F	88	PRMS; left thigh	N
5861	2478/04	R11_T	F	88	PRMS; left thigh	N
25650	18-2689	R12_T	F	13	ERMS; leg	Y
25650	18-2689	R12_T	F	13	ERMS; leg	Y
6667	2298/04	R13_T	M	34	ARMS; right hand	Y
6667	2298/04	R13_T	M	34	ARMS; right hand	Y
14064	09-2488	R14_T	M	46	SCRMS; left thumb	N
14064	09-2488	R14_T	M	46	SCRMS; left thumb	N
21386	16-1601	R15_T	M	53	SCRMS; left leg	N
23230	17-1668	R17_N	F	72	SkM counterpart to sample R_06T	N
23230	17-1668	R17_N	F	72	SkM counterpart to sample R_06T	N
14065	09-2488	R18_N	M	46	SkM counterpart to sample R_14T	N
14065	09-2488	R18_N	M	46	SkM counterpart to sample R_14T	N

14775	10-0947	R19_N	M	4	SkM counterpart to sample R_05T	Y
13275	0302/07	R20_N	M	54	SkM skeletal muscle	Unknown
5854	2478/04	R21_N	F	88	SkM counterpart to sample R_11T	N
5854	2478/04	R21_N	F	88	SkM counterpart to sample R_11T	N
7945	0987/06	R22_N	M	20	SkM counterpart to sample R_10T	Y
7945	0987/06	R22_N	M	20	SkM counterpart to sample R_10T	Y
30714	22-2225	R23_N	F	33	SkM skeletal muscle	Unknown
25643	18-2689	R24_N	F	13	SkM counterpart to sample R_12T	Y
25643	18-2689	R24_N	F	13	SkM counterpart to sample R_12T	Y
21375	16-1601	R25_N	M	53	SkM counterpart to sample R_15T	N
21375	16-1601	R25_N	M	53	SkM counterpart to sample R_15T	N
6659	2298/04	R26_N	M	34	SkM counterpart to sample R_13T	Y
6659	2298/04	R26_N	M	34	SkM counterpart to sample R_13T	Y
18133	13-2973	R27_N	F	54	SkM counterpart to sample R_02T	Y
7595	1579/06	R28_N	F	12	SkM counterpart to sample R_02T	Y
SCR46	11/13/2023	R29_N	M	59	SkM skeletal muscle	Unknown
SCR47	11/15/2023	R30_N	M	52	SkM skeletal muscle	Unknown

3.3.2 RNA-seq and bioinformatics of patient samples

RMS and matched adjacent control tissues were homogenized under liquid nitrogen. Total RNA was extracted using the miRNeasy Mini Kit (Qiagen, #217084). RNA samples were cleaned using the RNA Clean & Concentrator-5 kit (Zymo Research, #R1014). RNA concentration and integrity was measured on the Nanodrop 8000 spectrophotometer (Thermo Fisher Scientific, #ND-8000-GL) and the TapeStation (Agilent). RNA was stored at -80°C. mRNA libraries were constructed using the NEBNext ultra II RNA library prep kit (New England Biolabs, #E7775) and sequenced on a NovaSeq 6000 (Illumina) set to 150 bp paired end (PE) sequencing parameters. Small (sRNA) libraries were constructed using the NEBNext multiplex small RNA library prep kit (New England Biolabs) and sequenced on a NovaSeq 6000 (Illumina) set to 50 bp single end (SE) sequencing parameters.

For mRNA-derived cDNA libraries, FASTQ files were converted to FASTA files. Reads containing unassigned nucleotides were excluded. Trim Galore (RRID:SCR_011847) was used to remove adapter sequences and reads <20 nt. Trimmed reads were aligned to the human genome (v38) using HISAT2 (RRID:SCR_015530) (157). Transcripts were download from GENCODE (v46, RRID:SCR_014966) and Ensembl (v112, RRID:SCR_002344). Count matrices for transcripts were created using Kallisto (RRID:SCR_016583) (158). Differentially expressed genes were determined using the DESeq2 (v1.2.10, RRID:SCR_015687) package in RStudio (RRID:SCR_000432) (159-162). Differentially expressed genes were selected according to log₂ fold change ≥ 2 , $p \leq 0.05$ and false discovery rate (FDR) <5%. For sRNA derived cDNA libraries, FASTQ files were converted to FASTA. Reads containing unassigned nucleotides were excluded. Adapter sequences (3': AGATCGGAAGAGCACACGTCT; 5': GTTCAGAGTTCTACAGTCCGACGATC) were trimmed. sRNAs were mapped full length with 0 mismatches to the human genome (v38) and corresponding annotations using PatMaN (RRID_SCR_011831) (163). The latest set of human miRNAs were downloaded from miRBase

(v22, RRID:SCR_003152) (164). Normalization and differential expression analysis was performed using DESeq2 (v1.2.10, RRID:SCR_015687) (122,128,160,161,165-168). Independent filtering was used to remove low abundance transcripts in normalized counts. sRNAs were considered differentially expressed if they had a p-value <0.05, FDR <5% according to the Benjamini–Hochberg procedure (160,163) and a log₂ offset fold change >1.

3.3.5 RNA-seq of FP-RMS cells

Total RNA was extracted from cells using RNeasy Plus Mini Kits (Qiagen, #74134). After QC, RNA-seq libraries were constructed using TruSeq Stranded mRNA kits (Illumina) and sequenced on a NextSeq2000 (Illumina) according to instructions of the manufacturer. Reads were mapped to the hg19 human reference genome using STAR (v.2.7.10a, RRID:SCR_004463), and gene expression was calculated as transcripts per million mapped reads (TPM) using RSEM (v.1.3.1, RRID:SCR_000262). For differential expression analysis, the DESeq2 (RRID:SCR_015687) package was utilized. Genes with adjusted *p*-value < 0.05 and fold change of 1.5 or above were considered significantly differentially expressed. GSEA analysis were performed on log₂-fold change ranked list calculated by DESeq2's (RRID:SCR_015687) *lfcshrink* function.

3.3.6 Generation of cell lines and constructs

The human FP-RMS cell line Rh4 (RRID:CVCL_5916) were a gift from Dr. Beat Schaefer. Human FP-RMS cell lines Rh28 (RRID:CVCL_8725) and Rh30 (RRID:CVCL_0041) and human FN-RMS cell line RD (RRID:CVCL_1649), were gifts from Tim Triche (Children's Hospital of Los Angeles, Los Angeles, CA). Rh4 (RRID:CVCL_5916), Rh30 (RRID:CVCL_0041), and Rh28 (RRID:CVCL_8725) cell lines express the *PAX3::FOXO1* fusion gene. U2OS (RRID:CVCL_0042) osteosarcoma cells were a gift from Dr. David Kirsch. SMS-CTR and RH36 human FN-RMS cell lines were gifts from Brett Hall (Columbus Children's

Hospital, OH, USA). All cell lines tested negative for mycoplasma (using Lonza MycoAlert PLUS test at the Duke University Cell Culture Facility) and were also authenticated by short tandem repeat analysis (Promega Powerplex 18D at Duke University DNA analysis facility) in 2021; Rh28 (RRID:CVCL_8725) and Rh30 (RRID:CVCL_0041) were reauthenticated in 2023. HEK293T (RRID:CVCL_0063) cells were obtained from the ATCC through the Duke University Cell Culture Facility and cultured as previously described (26). For all studies cells were imaged on a Leica DMI1 microscope and processed on Leica Application Suite Software. For visual clarity, image contrast was modified, and scale bars were added with ImageJ software (RRID:SCR_003070), quantification was not performed with adjusted images.

RNAi constructs to *RUNX2* (sh1, sh2, and sh4) were obtained from the Duke Functional Genomics Core Facility through their Sigma Mission TRC1 lentiviral shRNA Library. Knockdown (KD) constructs were stably expressed using established lentiviral and selection methods. Lentiviral particles were produced from HEK293T (RRID:CVCL_0063) cells transiently transfected with the lentiviral expression plasmid using FuGENE® 6 (Promega, #E2691). Lentiviral particles were harvested at 24 and 48 h post transfection and filtered through 0.45 μ M filters. Polybrene was added to viral particles to a final concentration of 4 μ g/mL. Rh4 and Rh30 cells were selected with 1.0 μ g/mL puromycin (Sigma) for 72 h. RNAi constructs to negative control (QIAGEN, #1022076) and *PAX3::FOXO1* (Qiagen, #1027423) were purchased and transfected with lipofectamine RNAiMAX (Thermo Fisher Scientific, #13778150) according to manufacturer recommendations and collected after 48 h. RNAi (shRNA and siRNA) sequence information is listed in Table 6 on the next page.

Table 6: RNAi and Primer Sequences.

shRNA	Sequence (5'-3')
RUNX2, sh1	CCGGCTCAGTGATTTAGGGCGCATTCTCGAGAATGCGCCCTAAATCACTGAGTTTTT
RUNX2, sh2	CCGGCAGCACTCCATATCTCTACTACTCGAGTAGTAGAGATATGGAGTGCTGTTTTT
RUNX2, sh4	CCGGGCTACCTATCACAGAGCAATTCTCGAGAATTGCTCTGTGATAGGTAGCTTTTT
siRNA	Target sequence (5'-3')
PAX3::FOXO1	AACCTCTCACCTCAGAATTCA
Primer	FWD, REV (5'-3')
RUNX2	CCAAATTTGCCTAACCAGAA, GCTCGATTGCAATTGTCTCT
OC	GTGCAGAGTCCAGCAAAGGTG, CAGCCAACCTCGTCACAGTCC
MYOD1	CGACGGCATGATGGACTACA, TATATCGGGTTGGGGTTCGC
GAPDH	GAGAGACCCTCATTGTTG, GATGGTACATGACAAGGTGC
PAX3::FOXO1	CATGGATTTTCCAGCTATACAGAC, GTTCCTTCATTCTGAACACG

Doxycycline inducible constructs were cloned using the same oligo sequences from the TRC1 lentiviral shRNA library. Forward and reverse oligonucleotides were ordered with overhangs and loop sequences from Integrate DNA Technologies (IDT) and were then annealed together by PCR according to manufacturer recommendations. The tet-pLKO-puro (Addgene, #21915, RRID:Addgene_21915) backbone was cut using restriction enzymes AgeI and EcoRI (New England Biolabs). The vector and the insert (annealed oligos) were then ligated (TaKaRa, #6023) and transformed using Stbl3 cells. Colonies were picked and grown in lysogeny broth (LB) with ampicillin. Plasmids were extracted (Zymo, #D4213), sequenced by Eton Biosciences, and aligned with SnapGene (RRID:SCR_015052) to ensure that constructs were cloned correctly. Since the AgeI cut site is destroyed in the cloning process, additional verification of cloning included a restriction enzyme digestion with EcoRI, AgeI, and BamHI.

3.3.7 Quantitative real time PCR

RNA was isolated from cell pellets stored at -80°C using a RNeasy Mini Kit (Qiagen, #74106) according to manufacturer specifications. Conversion to cDNA was completed using the Omniscript RT kit (Qiagen, #205113). Quantitative real-time PCR (qRT-PCR) was performed using the SYBR Green system (Bio-Rad) according to manufacturer specifications. Primer sequence information used for qRT-PCR are listed in Table 6. Each biological experiment was run in triplicate. Technical and/or biological replicates are specified in figure legends.

3.3.8 Pharmacologic agents

Computer aided drug design molecule 522 (CADD522) (SelleckChem, #S0790) was solubilized in DMSO to a 10 μ M stock. Further dilutions were made in PBS.

3.3.9 ApoTox-Glo triplex assay

Viability and apoptosis assays were performed using the ApoTox-Glo Triplex Assay (Promega, #G6320) according to manufacturer specifications. Rh30 cells were plated at 5×10^3 cells/well in a 96 well plate in triplicate, samples were read 72 h following the completion of puromycin selection (72 h) with the SpectraMax i3x Multi-Mode Microplate Reader to measure the transmittance and fluorescence.

3.3.10 Immunoblotting

Cell pellets were lysed with high detergent RIPA (Cell Signaling Technology, #9806S) and Halt™ protease and phosphatase inhibitor cocktail (Thermo Fisher Scientific, #78442) then passaged through a 21-gauge needle for optimal shearing of DNA or sonicated for 3-5 sec using the Branson Fisher Scientific 150E Sonic Dismembrator at 22.5 kHz. Protein concentration was measured using the protein assay dye reagent concentrate (Bio-Rad, #500006). 4X protein Sample loading buffer (Thermo Fisher Scientific, #LC2570 and #NP0007) was combined with 20% β -mercaptoethanol or sample reducing agent (Thermo Fisher Scientific, #B0009) and then added to protein samples and then lysates were boiled for five min at 95°C. 20-30 μ g of lysate was loaded onto 10% or 4%-15% gradient Mini-PROTEAN precast gel (Bio-Rad) and resolved with SDS-PAGE and then transferred to Immobulin-FL polyvinylidene difluoride membrane (Millipore, #IPFL00010) or nitrocellulose membrane (Bio-Rad, #1620112). Membranes were immunoblotted with primary monoclonal antibodies anti-RUNX2 (Cell Signaling Technology, #8486S, RRID:AB_10949892), anti-FOXO1 (Cell Signaling, #2880S, RRID:AB_2106495) and anti- β -ACTIN (Cell Signaling Technology, #4970, RRID:AB_2223172). Polyclonal antibodies used included anti-GAPDH (Thermo Fisher Scientific, #PA1-9046, RRID:AB_1074703). Membranes were reacted with a secondary antibody, either anti-rabbit or anti-goat and then fluorescence measured on the Odyssey (Li-Cor) or imaged by enhanced chemiluminescence on the Chemi-Doc (Bio-Rad). Depending upon protein abundance, West Pico PLUS (Thermo Fisher

Scientific, #34580) or West Atto Ultimate Sensitivity (Thermo Fisher Scientific, #A38556) substrates were used and imaged at various exposures according to manufacturer protocol.

3.3.11 Colony formation assay

Cells were collected 72 h after selection and fixed with ice cold 70% ethanol. Cells were centrifuged and the ethanol was removed. Cells were resuspended in 500 μ L of PBS and propidium iodide and RNase A was mixed into solution slowly to avoid cell lysis. Cell cycle analysis was performed using the Canto Flow Cytometry machine through the Duke Flow Cytometry Core. Data was analyzed using FlowJo (RRID:SCR_008520).

3.3.12 MF20 staining

Myogenic differentiation was assessed by MF20 staining under light microscopy, as previously described (26). In brief, cells were plated at equal density to ~60% confluence in 6-well plates in regular media (RPMI with 10% fetal bovine serum). Once adherent, cells were treated with CADD522 for 72 h. Myotubes were fixed, permeabilized, and stained with primary antibody anti-sarcomere-myosin hybridoma MF20 followed by secondary biotinylated anti-mouse IgG, then HRP-streptavidin with a 3,3'-diaminobenzidine reagent. MF20 was obtained from the Developmental Studies Hybridoma Bank, created by the NICHD of the NIH and maintained at The University of Iowa, Department of Biology, Iowa City, IA 52242.

3.3.13 Growth curves

Cell growth was assayed using Trypan blue staining followed by automated cell counting on the TC20™ automated cell counter (BioRad). Cells were cultured in 6 well dishes and counted at three time points between days 1 through 3 in duplicate. 2×10^5 cells were plated per replicate at each time point.

3.3.14 *In vivo* xenograft assays

Xenograft studies utilized 8×10^6 (doxycycline-induced *RUNX2* KD experiment) or 6×10^6 (CADD522 experiment) cells resuspended in growth factor replete Matrigel (BD Biosciences, #354234) and implanted subcutaneously into the flanks of immunodeficient SCID/*beige* mice. Once tumors were palpable (doxycycline-induced *RUNX2* KD experiment) or 200 mm^3 (CADD522 experiment), mice were randomly divided into two groups followed by vehicle or compound administration. For doxycycline studies, mice received regular chow (Purina) or doxycycline containing chow (Enivgo). Prior to use, the CADD522 compound was dissolved in 5%DMSO/95%PBS at 10 mg/kg and injected intraperitoneally (IP). Mice in the vehicle group received 5%DMSO/95%PBS solution via IP injection. Tumors were measured 3 times weekly using calipers and tumor volume calculated as $[(\text{width} \times \text{length})/2]^3/2$. For doxycycline studies mice were sacrificed at specified timepoints of 13 days (sh2) and 15 days (sh4), upon reaching an Institutional Animal Care and Use Committee (IACUC)-defined maximum tumor burden ($2,000 \text{ mm}^3$) or decline in health. In the CADD522 studies, mice were sacrificed upon reaching an Institutional Animal Care and Use Committee (IACUC)-defined maximum tumor burden which was established as tumors measuring $>15 \text{ mm}$ in one direction, $>12 \text{ mm}$ in two directions, or decline in health rather than at a single timepoint for survival analyses. Portions of tumors were preserved in formalin-fixed and paraffin-embedded (FFPE) for immunohistochemistry or flash frozen in liquid nitrogen for RNA extraction using RNeasy Mini Kit (Qiagen, #74134).

3.3.15 Hematoxylin and Eosin

For all xenografts hematoxylin and eosin (H&E) staining, paraffin-embedded sections were deparaffinized in xylene, rehydrated through graded ethanols, and then submerged into hematoxylin (Cancer Diagnostics, #16600). Next, samples were submerged in water, clearing solution (Cancer Diagnostics, #16703-C), water, bluing solution (Cancer Diagnostics, #16702),

water, eosin (Cancer Diagnostics, #16601), dehydrated through graded ethanols, and xylene using the Leica Autostainer XL.

3.3.16 Immunohistochemistry

CADD522 xenografts were stained with rabbit monoclonal Ki-67 (Cell Signaling Technology, #12202, RRID:AB_2620142) according to the manufacturer's protocol. Briefly, paraffin-embedded sections were deparaffinized in xylene, rehydrated through graded ethanols, and then submerged into citrate unmasking solution for heat-induced antigenic retrieval, blocked with animal-free blocking solution (Cell Signaling Technology, #15019), incubated with Ki-67 (Cell Signaling Technology, #12202, RRID:AB_2620142) primary antibody (1:800) 4 °C overnight and developed using the Signalstain® Boost IHC Dec. (HRP, Rab) (Cell Signaling Technology, #8114S) and DAB (Signalstain® DAB diluent, Cell Signaling Technology, #11724S; Signalstain® DAB chromogen concentrate, Cell Signaling Technology, #11725S) followed by counterstaining with Mayer's hematoxylin (Sigma Aldrich, #MSH16-500), dehydration, clearing and mounting. Sections were captured on a Leica DMLB microscope with DFC425 camera and processed on Leica Application Suite software. For quantification, 4 random fields at 40X magnification per section were captured and analyzed by manual counting with the aid of ImageJ (RRID:SCR_003070) software. For visual clarity, image contrast was modified, and scale bars were added with ImageJ software (RRID:SCR_003070), quantification was not performed with adjusted images.

Doxycycline-inducible xenografts were stained with rabbit monoclonal Ki-67 (Abcam, #AB16667, clone SP6, RRID:AB_302459). The antibody is listed as for research use only. Ki-67 (Abcam, #AB16667, clone SP6, RRID:AB_302459) was used at 1:200 dilution with Ab Diluent (Discovery, #760-108). Immunohistochemistry tests were performed using the Ultra Discovery automated staining platform. The tissue sections were pretreated (epitope retrieval) with cell conditioning solution CC1 (Roche, #950-124) for 56 min, then incubated with Ki-67 (Abcam,

#AB16667, clone SP6, RRID:AB_302459) for 1 h at 36 °C. Rabbit IgG, substituted for the primary antibody, was used as the negative control. After binding of the primary antibody, anti-rabbit HQ (Roche, #760-4815, RRID:AB_2811171) were applied and incubated for 12 min, followed by 12 min incubation with anti-HQ HRP (Roche, #760-4820, RRID:AB_3068525) for antigen detection. Roche HRP Detection is a biotin-free, hapten (HQ) anti-hapten (anti-HQ) linked horseradish peroxidase-linker antibody conjugate system for the detection of tissue-bound primary antibodies. The kit includes peroxidase blocking reagent, post primary IgG linker reagent (HQ labelled secondary antibody), and anti-HQ-HRP reagent to localize HQ labelled secondary antibodies, the immunohistochemistry reactions were visualized with DAB chromogen and counterstained hematoxylin. Sections were captured on a Leica DMLB microscope with DFC425 camera and processed on Leica Application Suite software. For quantification, 4 random fields per section were used to analyze with ImageJ (RRID:SCR_003070) software.

For all xenografts, Cleaved Caspase 3 (CC3) staining, the rabbit monoclonal CC3 antibody (Cell Signaling Technology, #9661S, RRID:AB_2341188) was used at 1:800, with Ab Diluent (Discovery, #760-108). Immunohistochemistry tests were performed using the Ultra Discovery automated staining platform. The tissue sections were pretreated (epitope retrieval) with cell conditioning solution CC1 (Roche, #950-124) for 56 min. CC3 (Cell Signaling Technology, #9661S, RRID:AB_2341188) was applied and incubated for 60 min at 36°C. Rabbit IgG, substituted for the primary antibody, was used as the negative control. After binding of the primary antibody, anti-rabbit HQ (Roche, #760-4815) were applied and incubated for 12 min, followed by 12 min incubation with anti-HQ HRP. For visualization, ChromoMap DAB (Discovery, #760-159) was applied and incubated for 5 min. Roche HRP Detection is a biotin-free, hapten (HQ) anti-hapten (anti-HQ) linked horseradish peroxidase-linker antibody conjugate system for the detection of tissue-bound primary antibodies. The kit includes peroxidase blocking reagent, post primary IgG linker reagent (HQ labelled secondary antibody), and anti-HQ-HRP

reagent to localize HQ labelled secondary antibodies. The immunohistochemistry reactions were counterstained with hematoxylin. Sections were imaged on a Leica DMLB microscope with DFC425 camera and processed on Leica Application Suite software, 4 random fields per section were used to analyze with ImageJ (RRID:SCR_003070) software.

3.3.17 Statistical analysis

All statistical analysis, except for sequencing, were performed using GraphPad Prism (RRID:SCR_002798) software. A p -value of 0.05 or lower was considered significant, and p -values were considered significant at *, $p < 0.05$; **, $p < 0.01$; ***, $p < 0.001$; and ****, $p < 0.0001$. Unless otherwise notes, data is presented as the mean and standard error (SE). Statistical tests used include unpaired student's t-test with Welch's correction when appropriate (cell-based assays), Pearson's correlation coefficient when appropriate, two-way analysis of variance (ANOVA) or mixed model with the Holm-Šidák correction (cell growth curves), one-way ANOVA with the Dunnett correction (cell-based assays), multiple unpaired student's t-test with a two-stage linear set-up procedure of Benjamini, Krieger, and Yekutieli methods applied (CADD522 *in vivo* FDR<0.1, doxycycline-inducible *in vivo* FDR<0.01), survival analysis evaluated by Gehan-Breslow-Wilcoxon test. For sequencing experiments of patient samples, variability between sequencing libraries was evaluated using scatter plots, replicate-to-replicate differential expression size split box plots, intersection and Jaccard similarity analysis. Empirical differential expression analysis was confirmed by parametric (t-tests) and non-parametric (Mann-Whitney-U) tests. All sequencing data presented in this study fulfilled log₂ fold change >1, $p < 0.05$ and FDR <.5 criteria. For CRISPR DepMap data, the box plot of the CERES dependency score, which is based on DepMap data from cell depletion assays in CRISPR screens, demonstrating a specific dependency for *RUNX2* in fusion-positive ARMS compared to all cancer types analyzed together. A lower CERES score indicates a higher likelihood that the gene of interest is essential in a given cell line. A score of 0 is equivalent to a gene that is not essential

whereas a score of -1 corresponds to the median of all common essential genes. Two-group comparisons were performed in parallel across genes using the LIMMA (RRID:SCR_010943) RStudio (RRID:SCR_000432) package (169), which uses parametric empirical Bayes methods to pool information across genes when assessing the significance of observed group differences. *P*-values for each gene are computed from empirical Bayes moderated t-statistics. For sequencing experiments of FP-RMS cell lines, genes with adjusted *p*-value < 0.05 and fold change of 1.5 or above were considered significantly differentially expressed.

3.3.18 Data availability

All data supporting the findings of this study are available within the article and Supplementary files or from the corresponding author on request. Raw sequencing files are available at Gene Expression Omnibus (GEO) (RRID:SCR_005012) under the accessions GSE279954 (mRNA) and GSE280045 (sRNA). Raw sequencing files for Rh30 and Rh4 *RUNX2* KD are available at GSE298855 (mRNA).

3.4 Results

3.4.1 *RUNX2* is highly expressed in RMS primary tumor tissue

To investigate clinically relevant dysregulated genes in RMS, establish an additional primary human tumor dataset to aid RMS researchers, and to identify additional targetable proteins important for the FP-RMS myogenic circuit, we analyzed 13 flash-frozen patient-derived RMS primary tumor samples, including alveolar (ARMS), embryonal (ERMS), spindle cell/sclerosing (SCRMS), and pleomorphic (PRMS) histologies, combined with 13 patient-derived non-malignant wildtype skeletal muscle samples (SkM) (Table 5) using mRNA-seq. Around 29M reads per sample were obtained. Short reads were mapped to the human genome, which revealed that the majority mapped to protein coding exons (Supplemental File 1A). Pearson's correlation coefficient (PCC) showed a linear correlation between the RMS and SkM

samples (Supplemental File 1B), meaning there was a difference in mRNA expression patterns between tumor and normal tissues. The coefficient of determination of the SkM group was high ($R^2 < 0.8$), confirming tissue similarity. RMS intragroup variation was not strongly correlated, demonstrating a high variation in mRNA expression patterns between tumor samples (Supplemental File 1B). There was a low correlation between the PRMS sample and all other samples including SkM and RMS, with the strongest correlation with the SCRMS sample ($R^2 = 0.588$) (Supplemental File 1B). Processed sequencing data was reduced to 2-dimensions, where we observed distinct clustering across the samples (Supplemental File 1C). Most RMS subtype groups overlapped, indicating a similarity in differentially expressed genes; however, PRMS was distinctly separate from all other samples suggesting that PRMS is transcriptionally different from other RMS subtypes (Supplemental File 1C), though this was a single patient sample.

To identify and visualize differentially expressed genes in ARMS samples, which are typically fusion-positive, heat map-based hierarchical cluster analysis was performed (Supplemental File 1D). Processed data for all genes is provided in Supplemental File 2. Differentially expressed genes for the heat map were included according to their relevance to sarcoma/cancer (41,170). Among the selected differentially expressed genes, 47 were upregulated and 11 were downregulated (Supplemental File 1D). The most abundant upregulated genes in ARMS samples were *SOX1* (\log_2 fold change (FC)=9.86), *MAPK15* (\log_2 FC=9.18) and *FGF8* (\log_2 FC=7.82) (Supplemental File 1D) FP-RMS related genes (41-44) of interest that were also upregulated included oncogenes such as *MYCN*, *IGF2*, *RUNX2*, *MMP13* and *MMP11* (Supplemental File 1D). The most markedly downregulated were *MYH1* (\log_2 FC=-13.43), *MYH2* (\log_2 FC=-10.77) and *MYOC* (\log_2 FC=-7.9) (Supplemental File 1D). Differentially expressed genes in ERMS, SCRMS and PRMS, which are typically (but not always) fusion-negative were also visualized through heat map-based hierarchical cluster analysis (Supplemental File 1E).

Processed data for all genes is provided in Supplemental File 2. The most abundant upregulated genes included *NPY* (\log_2 FC=26.38), *MAGEA6* (\log_2 FC=25.6) and *MAGEB2* (\log_2 FC=24.53) (Supplemental File 1E). The most markedly downregulated genes included *IDI2* (\log_2 FC=-12.31), *DUPDI* (\log_2 FC=-10.72) and *MYOC* (\log_2 FC=-10.48) (Supplemental File 1E). The *MAGE* gene family, which is being evaluated as a candidate for immunotherapy (171), was the most represented gene group with 14 differentially expressed genes (Supplemental File 1E).

Next, all ARMS and E/SC/PRMS differentially expressed genes were compared to a series of independent publicly available datasets to identify potential FP-RMS and FN-RMS therapeutic and mechanistic targets of interest (Figure 19A). Gene set intersection size of processed data was determined by comparing this study's differentially expressed genes against RMS cell line dependencies and known Rh30 and Rh4 high confidence PAX3::FOXO1 targets, identified through CUT&RUN and ChIP-seq experiments following PAX3::FOXO1 degradation or genetic inhibition (Figure 19A,B) (41,42). Out of 11,494 differentially expressed genes identified in ARMS (n=4,484) and E/SC/PRMS (n=7,008), 27% or 3,091 genes were exclusively represented in both datasets (Figure 19B). When the data was narrowed further to account for potential fusion-status, 0 differentially expressed E/SC/PRMS genes were exclusive to FN-RMS and not FP-RMS dependencies, but 5 genes, *IGF2BP1*, *OSTC*, *CEP152*, *CNPY2*, and *LMO4*, were exclusive to FN-RMS dependencies as well as ARMS and E/SC/PRMS differentially expressed genes (Figure 19B; Supplemental Files 2,3). These hits were not pursued further because we were primarily interested in the gene candidates that were exclusive to probable fusion-status in addition to RMS histological interpretation. This latter analysis identified a subset of 4 differentially expressed genes in ARMS and E/SC/PRMS, *TFAP2B*, *FGF8*, *EYAI*, and *RUNX2*, exclusive to 4/5 gene sets, the FP-RMS DepMap, Rh30 FP-RMS targets, and Rh4 FP-RMS targets (Figure 19A,B; Supplemental Files 2, 3). To further narrow this list, we cross-referenced with the literature to determine whether pharmacological inhibitors were either

available or in development. We found that *EYA1* (\log_2 FC ARMS=2.23 E/SC/PRMS=2.06) and *RUNX2* (\log_2 FC ARMS=2.67 E/SC/PRMS=4.56) fit these criteria (Figure 19A,B) (122,129,130,172). There are several *EYA1* inhibitors in development including DS-1-38, which blocks sonic hedgehog signaling, but despite the incidence of *EYA1* in Ewing's sarcoma there were no publications using these inhibitors in sarcomas (35,173). Alternatively, the *RUNX2* inhibitor, computer aided design molecule 522 (CADD522) reduces the DNA-binding capacity of *RUNX2* and has been tested *in vitro* and *in vivo* in bone sarcoma and breast cancer models (75,122,129,130). Due to the increased differential expression of *RUNX2* versus *EYA1*, we moved forward to study *RUNX2* as a therapeutic target in FP-RMS.

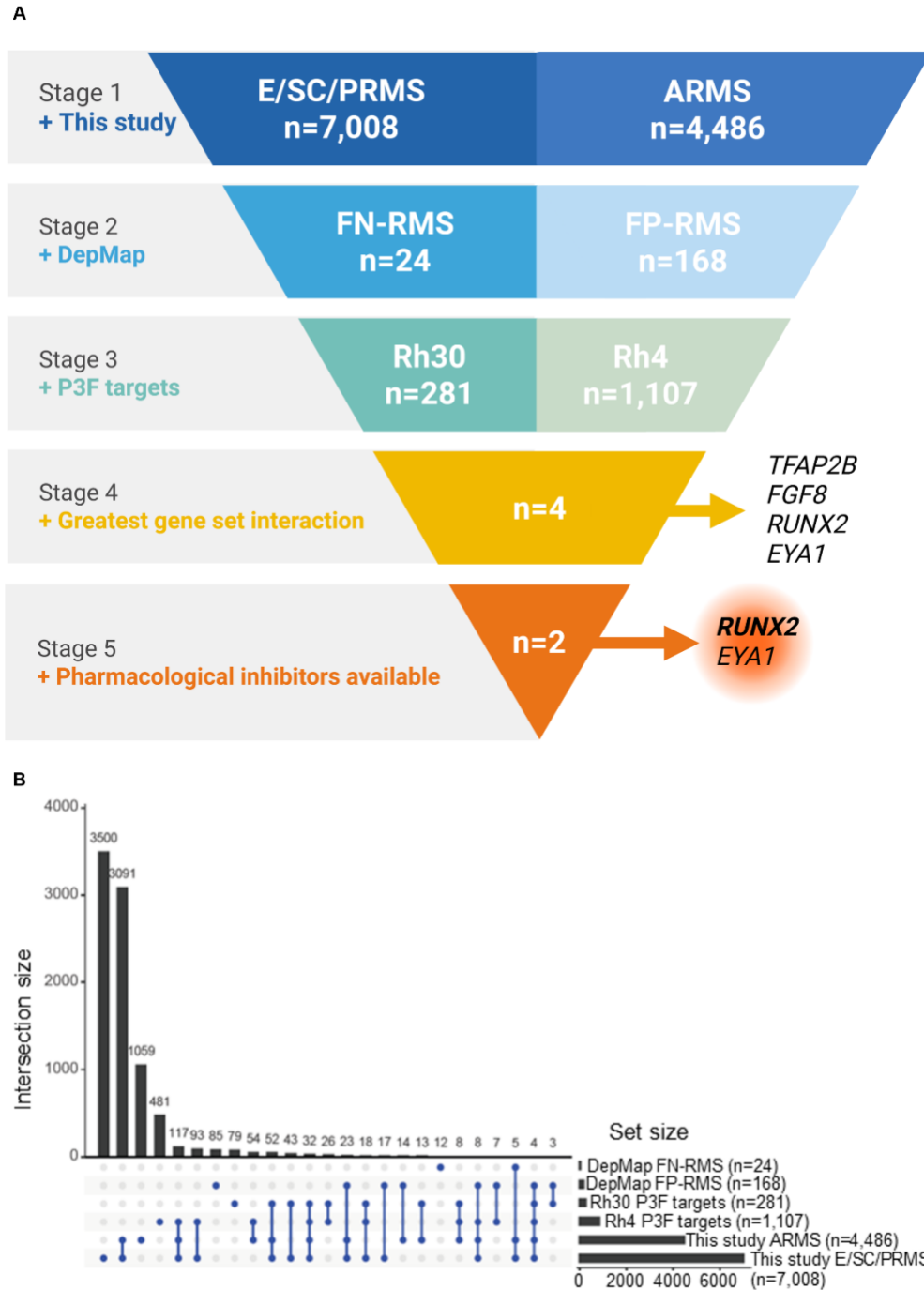


Figure 19: mRNA-seq performed on archival fresh frozen RMS tissues classified according to their histological interpretation.

A, Candidate selection of differentially expressed genes across the current study (stage 1), the cancer DepMap (stage 2), Rh30 and Rh4 P3F targets (stage 3). Candidate genes of interest included those with the greatest gene set intersection (stage 4) and with pharmacological inhibitors (stage 5) available. Top candidate is bolded. B, UpSet plot to

visualize intersected genes (and therefore generate gene/s-of-interest for downstream studies) across the current study, the cancer DepMap, and Rh30 and Rh4 cell line P3F targets.

3.4.2 *RUNX2* dependency is specific to pediatric sarcomas including RMS

To evaluate the clinical relevance of *RUNX2* and its validity as a potential therapeutic and mechanistic RMS target of interest, we interrogated publicly available patient databases. Using the St. Jude PeCan database (<https://pecan.stjude.cloud>) that contains a cohort of 2,486 pediatric tumors, we found *RUNX2* was highly expressed in FP-RMS (Figure 20A), second only to expression in the bone sarcoma osteosarcoma (OS), where the role of *RUNX2* is well characterized (174). *RUNX2* expression was highest in FP-RMS, followed by FN-RMS, while non-sarcoma pediatric cancers including neuroblastoma (NBL), glioma (GLM), ependymoma (EPDY) and medulloblastoma (MBL) were less dependent on *RUNX2* (Figure 20A). mRNA-seq cluster analysis was used to visualize *RUNX2* expression specifically in sarcomas, where the highest expression was in FP-RMS and osteosarcoma (Figure 20B). Further analysis of a published dataset showed that *RUNX2* expression was higher in FP-RMS tumors when compared to FN-RMS and myoblasts (Figure 20C) (41). Analysis of a separate, non-overlapping dataset from the Oncogenomics website (<https://omicsoncogenomics.ccr.cancer.gov/cgi-bin/JK>) hosted by the NCI showed a significant association of poor survival with high expression of *RUNX2* in all RMS regardless of fusion status and histology ($p=0.0143$) (Figure 20D) and combined FP-RMS and FN-RMS cases with known fusion status ($p=0.0399$) (Figure 20E). When separated and analyzed by fusion presence, the statistical power was weaker, but trending towards significance, possibly due to the lower number of patients in the high *RUNX2* group, FP-RMS ($p=0.0554$) high *RUNX2* (n=10) and low *RUNX2* (n=40) (Figure 20F). In the case of FN-RMS ($p=0.1421$), despite a higher number of patients high *RUNX2* (n=19) and low *RUNX2* (n=45) groups (Figure 20G), statistical power was further from significance than in FP-RMS. Thus, we conclude that high *RUNX2* expression was correlated with poor survival across all RMS cases and may portend an

even worse outcome in *PAX3/7::FOXO1* expressing patients (Figure 20E-G). More data is required to establish a strong link between high *RUNX2* expression, fusion status, and survival.

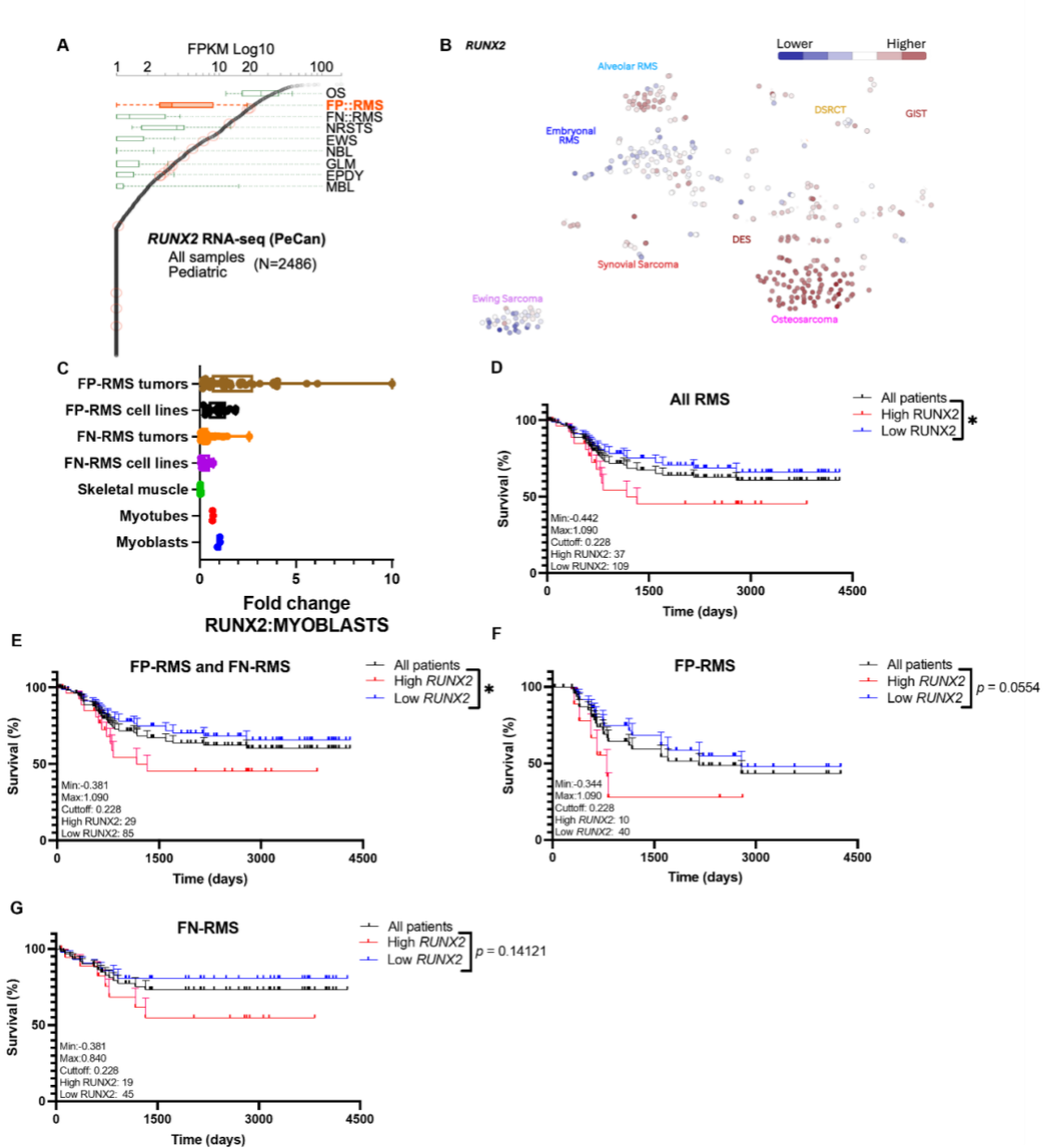


Figure 20: Expression and survival analysis of *RUNX2* in FP-RMS and FN-RMS.

A, Analysis of *RUNX2* expression in a cohort of 2486 pediatric cancers showing expression of *RUNX2* in OS as well as FP-RMS and NRSTS compared to expression in other pediatric solid tumors. OS, osteosarcoma (n=112), FP-RMS, fusion-positive rhabdomyosarcoma (n=16), FN-RMS, fusion-negative rhabdomyosarcoma, NRSTS (n=28), non-rhabdomyosarcoma soft tissue sarcoma (n=13), EWS, Ewing sarcoma (n=5), NBL, neuroblastoma (n=198), GLM, glioblastoma (n=182), EPDY, ependymoma (n=92), MBL,

medulloblastoma (n=31). Other pediatric solid tumors shown for comparison. B, Cluster plot of *RUNX2* expression in pediatric bone and soft tissue sarcomas. C, *RUNX2* expression in FP-RMS tumors compared to myoblasts. Myoblast (n=3), myotube (n=3), skeletal muscle (n=14), FN cell line (n=12), FN tumor (n=63), FP cell line (n=16), FP tumor (n=39). D,E,F,G Kaplan-Meier plot demonstrates the correlation between *RUNX2* and survival in all RMS (n=146), FP-RMS and FN-RMS combined (n=114), FP-RMS (n=50), and FN-RMS (n=64).

Single-nucleus RNA sequencing (snRNA-seq) of GTExPortal data of normal skeletal muscle tissue showed that 2.43% of skeletal muscle myocyte cells express *RUNX2* (Figure 21A). To gain insight into the dependency of individual RMS cell lines on *RUNX2*, we interrogated the DepMap CRISPR database and found that *RUNX2* is strongly selective in human FP-RMS cell lines, ranking #51 in FP-RMS alone (Supplemental File 4A) and #77 compared to all other cancer cell lines (Figure 21B; Supplemental File 4B) (175). Human FP-RMS cell lines exhibit a significantly higher dependency on *RUNX2* compared to FN-RMS and other solid tumor types (Figure 21C) (175). Immunoblot analyses validated elevated *RUNX2* protein levels in FP-RMS cell lines compared to FN-RMS and positive control OS cell lines (Figure 21D). In this work, due to their dependency on and high expression of *RUNX2* (Figure 21C,D), the majority of experiments going forward were performed in Rh30 cells, with supporting complementary experiments performed in Rh4 cells.

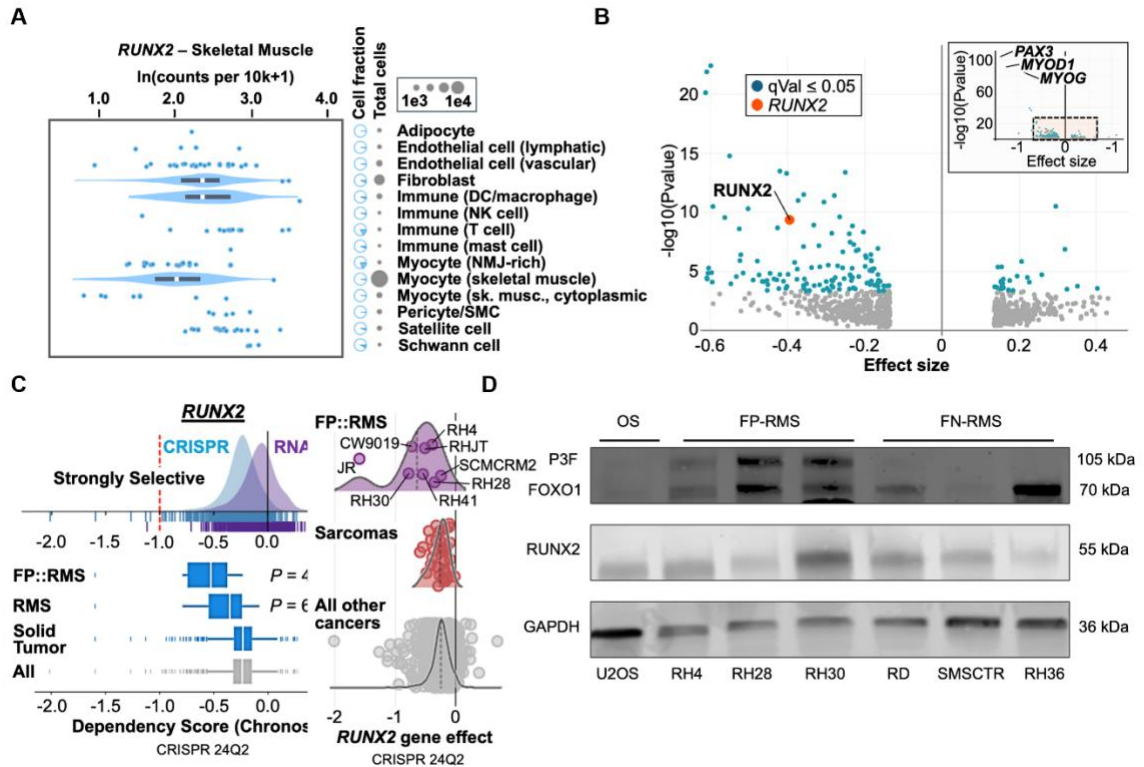


Figure 21: *RUNX2* dependency analysis and characterization in RMS.

A, Expression of *RUNX2* in normal skeletal muscle. Skeletal muscle myocyte expressing *RUNX2* (n=504), total cells (n=20772). **B**, Volcano plot showing gene dependencies in FP-RMS cell lines relative to all other cancer cell lines. Box in upper right-hand corner are all the genes in the dataset and larger figure is a zoom in on the dashed box Supplemental Table 5. **C**, (Left side) Box plot of the CERES dependency score demonstrating *RUNX2* specific dependencies in FP-RMS compared to all cancer types analyzed together. FP-RMS (n=8), RMS (n=13), Solid Tumor (n=1019), All Cancer. (Right side) Characterization of *RUNX2* gene effect on FP-RMS cell lines compared to all sarcomas, and all other cancer. FP-RMS (n=8), RMS (n=13), Solid Tumor (n=1019), All Cancer. **D**, Immunoblot of PAX3::FOXO1, FOXO1, and *RUNX2* protein expression in OS, FP-RMS, and FN-RMS cell lines.

Last, since *RUNX1* is a close ortholog of *RUNX2*, in parallel we investigated the expression and dependency of *RUNX1* in RMS according to publicly available datasets. When comparing FP-RMS to FN-RMS tumors and normal myoblasts, *RUNX1* expression was lower (Figure 22A,B) which was consistent with increased *RUNX1* expression in E/SC/PRMS patients ($\log_2 \text{FC}=1.44$), but not in ARMS (Supplemental File 1D) (35). Though *RUNX1* expression was elevated in FP-RMS and FN-RMS cell lines (Figure 22A) and ARMS and ERMS patients (Figure

22B), Kaplan-Meier analyses revealed that increased *RUNX1* expression was associated with increased survival in all RMS ($p=0.0640$) (Figure 22C) (42).

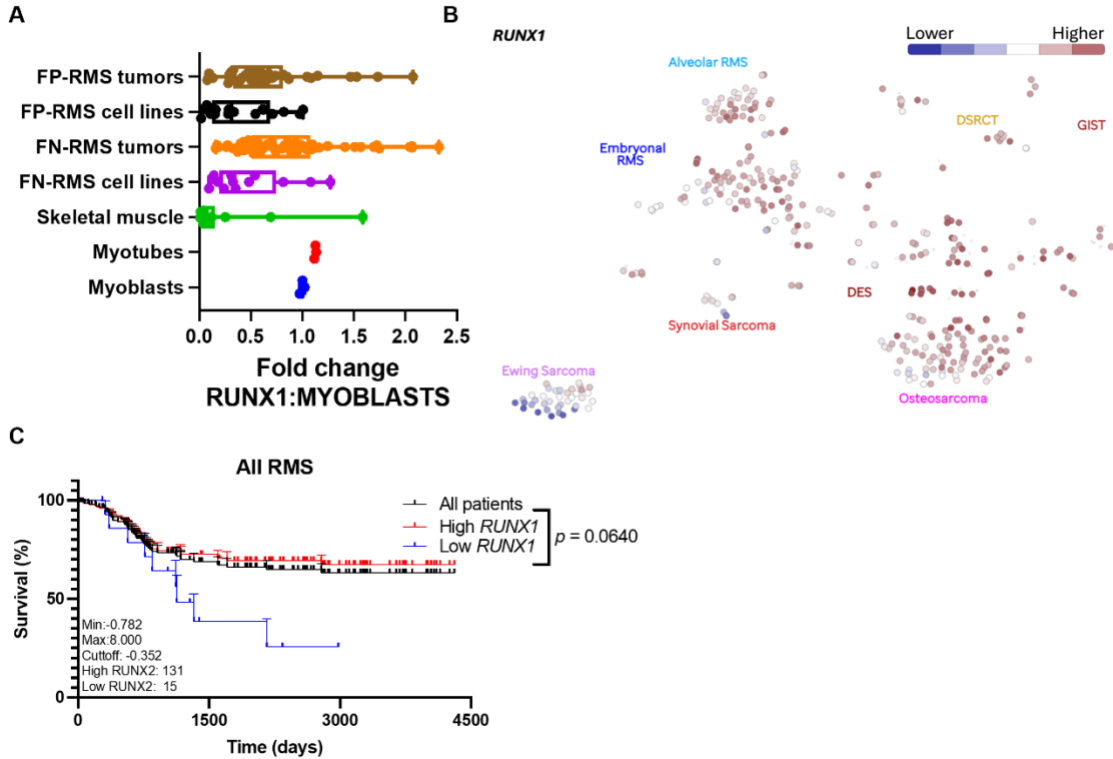


Figure 22: Expression and survival analysis of *RUNX1* in FP-RMS and FN-RMS.

A, *RUNX1* expression in FN-RMS tumors and cell lines compared to myoblasts. Myoblast (n=3), myotube (n=3), skeletal muscle (n=14), FN cell line (n=12), FN tumor (n=63), FP cell line (n=16), FP tumor (n=39). **B**, Cluster plot of *RUNX1* expression in pediatric bone and soft tissue **C**, Kaplan-Meier plot demonstrates the correlation between *RUNX1* and survival in all RMS.

3.4.3 *In vitro* KD of *RUNX2* in FP-RMS cell lines impairs oncogenic phenotypes

Combining the information gained from analysis of RMS patient samples, the role of *RUNX2* in other human cancers, and publicly available patient and cell line-based RMS datasets, we hypothesized that by interfering with *RUNX2* activity we could impair FP-RMS oncogenic phenotypes and potentially disrupt PAX3::FOXO1 signaling. To achieve *RUNX2* loss of function, we generated four lentiviral constructs bearing unique short hairpin (sh)RNAs to the

RUNX2 coding sequence. Because sh3 was ineffective in suppressing *RUNX2* levels, it was excluded from further analysis. Stable expression of any of the three remaining shRNAs (sh1, sh2, or sh4) resulted in *RUNX2* suppression as assessed by qRT-PCR and immunoblot in Rh30 and Rh4 cells (Figure 23A,B; Figure 24A,B). Phenotypically, *RUNX2* KD significantly reduced cell growth over the course of 72 h after selection in Rh30 and Rh4 cells (Figure 23C; Figure 24C). *RUNX2* KD also impaired colony formation of Rh30 cells (Figure 23D,E). To gain insight into Rh30 and Rh4 mechanism of decreased cell growth, we imaged FP-RMS cells after *RUNX2* suppression and found that *RUNX2* KD resulted in decreased cell confluency accompanied by changes in cell morphology (Figure 23F; Figure 24D). Specifically, cells appeared elongated and myotube-like or had cellular blebbing and fragmentation consistent with cell death. Parallel studies in Rh4 cells replicated these morphologies (Figure 23F; Figure 24D). To verify the differentiation phenotype visualized in cell culture, we performed qRT-PCR analysis, which revealed that *MYOD1* and *OC*, genes associated with differentiation of MSCs, myoblasts, and osteoblasts, were significantly upregulated following *RUNX2* KD in Rh30 (Figure 23G,H) (176).

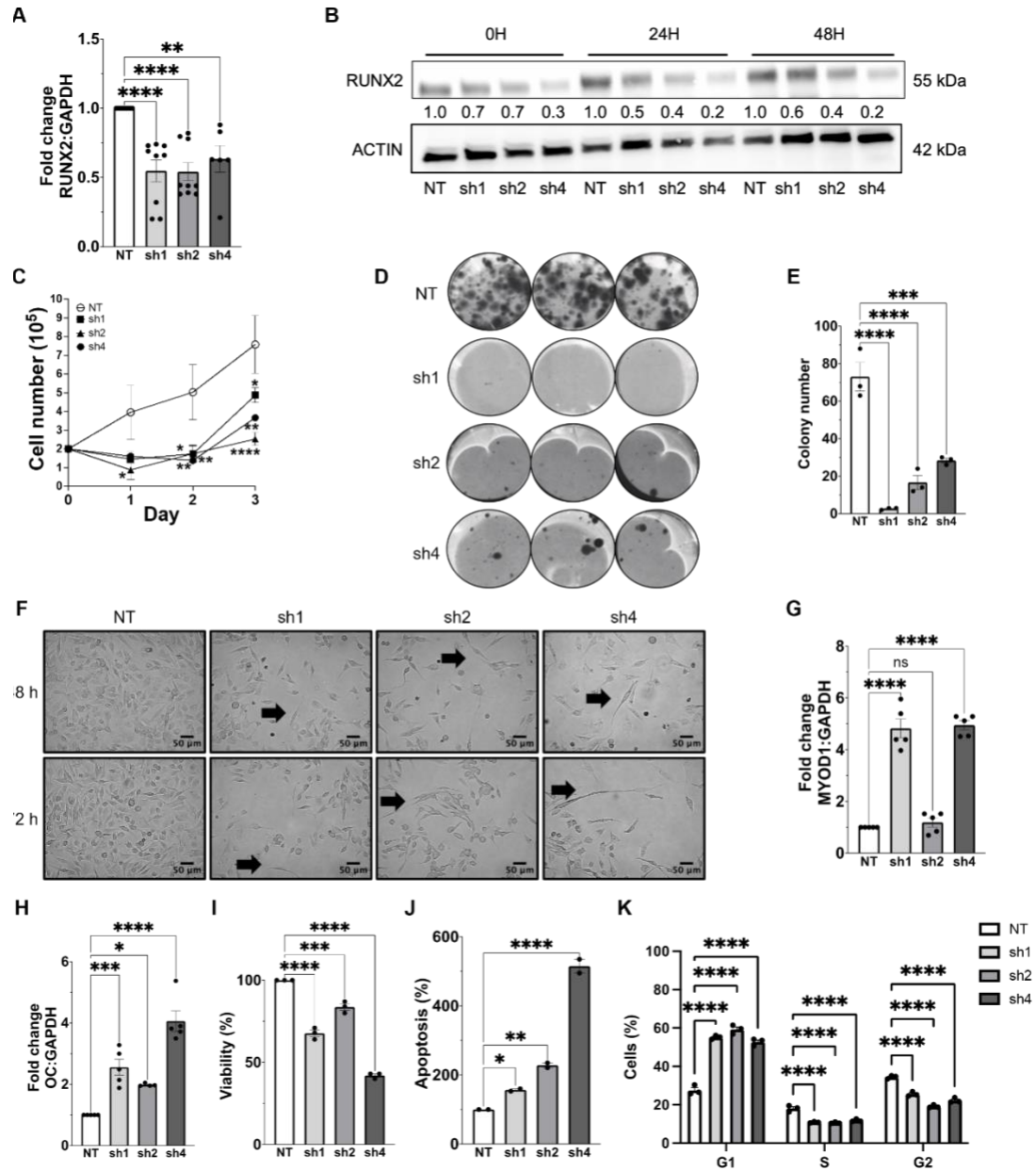


Figure 23: *RUNX2* knockdown in human FP-RMS cells (Rh30) impairs classical oncogenic phenotypes *in vitro*.

A, qRT-PCR for *RUNX2* quantification in the negative control (NT) Rh30 cells and the three independent knockdown cells (sh1, sh2, sh4). Each black dot represents an independent biological replicate. **B**, Normalized *RUNX2* protein expression in the negative control (NT) Rh30 cells and the three independent knockdown cells (sh1, sh2, sh4) measured at 0 h, 24 h and 48 h. **C**, Cell growth in negative control and *RUNX2* stable knockdown Rh30 cells. Black dots are independent biological replicates. **D**, Colony formation in negative control and *RUNX2* stable knockdown Rh30 cells. **E**, Colony numbers in negative control and *RUNX2* stable knockdown Rh30 cells. Black dots are independent

technical replicates. F, *RUNX2* knockdown through three independent stably expressed sh*RUNX2* lentiviral preparations (sh1, sh2, sh4) plus negative control (shNT) in Rh30 cells. Black arrows point to visible areas of differentiation. Cells were imaged at 20X magnification and captured at 48 h and 72 h. Scale bars are 25 μ m. G,H, qRT-PCR for known drivers of mesenchymal stem cell differentiation; *MYOD1* and *OC*, following *RUNX2* stable knockdown. Black dots are independent biological replicates. I, Cell viability of negative control and *RUNX2* stable knockdown Rh30 cells. Black dots are independent technical replicates. J, Quantification of caspase 3/7 mediated apoptosis in negative control and *RUNX2* stable knockdown Rh30 cells. Black dots are independent technical replicates. K, Cell cycle analysis in negative control and *RUNX2* stable knockdown Rh30 cells. Black dots are independent biological replicates consisting of three technical replicates each.

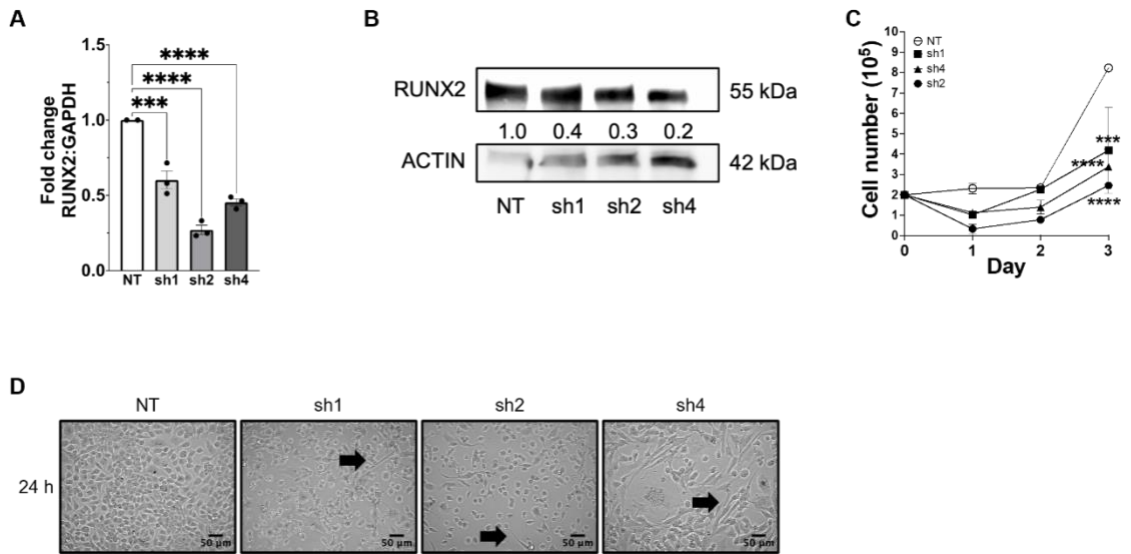


Figure 24: *RUNX2* knockdown in human FP-RMS cells (Rh4) impairs classical oncogenic phenotypes *in vitro*.

A, qRT-PCR for *RUNX2* quantification in the negative control (NT) Rh4 cells and the three independent knockdown cells (sh1, sh2, sh4). Black dots are technical replicates. **B**, Normalized *RUNX2* protein expression in the negative control (NT) Rh4 cells and the three independent knockdown cells (sh1, sh2, sh4) measured at 48 h. This blot is identical to Fig. 5F. **C**, Cell growth in negative control and *RUNX2* stable knockdown Rh30 cells. Black dots are independent biological replicates. **D**, *RUNX2* knockdown through three independent stably expressed sh*RUNX2* lentiviral preparations (sh1, sh2, sh4) plus negative control (shNT) in Rh4 cells. Black arrows point to visible areas of differentiation. Cells were imaged at 20X magnification and captured at 24 h. Scale bars are 50 μ m.

Increased *MYOD1* expression was not significant with sh2 (FC=1.89) while upregulation of *OC* was less robust in sh2 (FC=1.98) versus sh1 (FC=2.56) and sh4 (FC=4.06) (Figure 23G,H). To verify the apoptotic phenotype visualized in cell culture, we performed cell viability assays paired with apoptosis assays (Figure 23I,J). sh4 demonstrated a >50% decrease in cell

viability and a 4-fold increase in apoptosis compared to the negative control (NT) (Figure 23I,J). To further evaluate whether a reduction in proliferation, in addition to increased apoptosis, was responsible for decreased viability, we performed cell cycle analysis of Rh30 cells (Figure 23K). Across all shRNA constructs, we saw an increased accumulation of approximately 40% of cells in G1 compared to the negative control (Figure 23K). Also, there was a significant decrease of cell in S phase by approximately 50% and G2/M by approximately 10% across all shRNAs (Figure 23K). Together, these data support the importance of *RUNX2* expression in maintaining oncogenic phenotypes required for FP-RMS cell growth, cell state, and cell survival.

3.4.4. Bulk transcriptome analysis of *RUNX2* KD validates phenotypic findings and suggests impaired *PAX3::FOXO1* activity

To identify the global genetic changes responsible for oncogenic phenotypes following *RUNX2* KD in Rh30 and Rh4 cells, we performed mRNA-seq of FP-RMS cells with stable sh4 *RUNX* KD at three timepoints: 0 h, 24 h, and 48 h after completion of selection (Figure 25; Figure 26). This analysis not only aimed to identify changes in gene expression patterns, but also evaluated how expression fluctuates over time, to inform future *RUNX2* mechanistic and pharmacologic studies. Around 20M reads per sample were obtained (Supplemental File 5). Short reads were mapped to the human genome, which confirmed the majority mapped to protein coding exons (Supplemental File 5; Supplemental File 6). Processed sequencing data was reduced to 2-dimensions where we observed distinct clustering across the samples (Figure 25A,B). PC1 accounted for 54% of variance while PC2 accounted for an additional 27% variance in Rh30 (Figure 25A). PC1 accounted for 37% of variance while PC2 accounted for an additional 23% variance in Rh4 (Figure 25B). Even though Rh30 and Rh4 are two distinct FP-RMS cell lines, the majority of *RUNX2* KD groups overlapped at distinct duplicate timepoints, indicating a similarity in differentially expressed genes; however, 0 h post selection was distinctly separate

from 24 h and 48 h suggesting that downstream effects of *RUNX2* KD amplify over time (Figure 25A,B).

Of the differentially expressed genes in Rh30 (Figure 25C), the most abundant upregulated genes following *RUNX2* KD at 0 h, 24 h, and 48 h post selection include *HID1* (\log_2 FC=5.90), *COL6A6* (\log_2 FC=3.80) and *C4BPB* (\log_2 FC=6.09) respectively (Supplemental File 6). Genes with known roles in FP-RMS biology were also downregulated at all time points including *MYCN*, *FGFR4*, *NOTCH1*, *WWTR1*, and *RUNX2* (Supplemental File 6) (9,44,54). Of the differentially expressed genes in Rh4 (Figure 25D), the most abundant upregulated genes following *RUNX2* KD at 0 h, 24 h, and 48 h post selection include *KLHDC7B* (\log_2 FC=5.82), *ACP5* (\log_2 FC=4.35) and *SCN9A* (\log_2 FC=4.15) respectively (Supplemental File 6). Genes of interest with known roles in promoting FP-RMS that were also downregulated at all time points included the same genes as in Rh30 except for *MYCN* (Supplemental File 6).

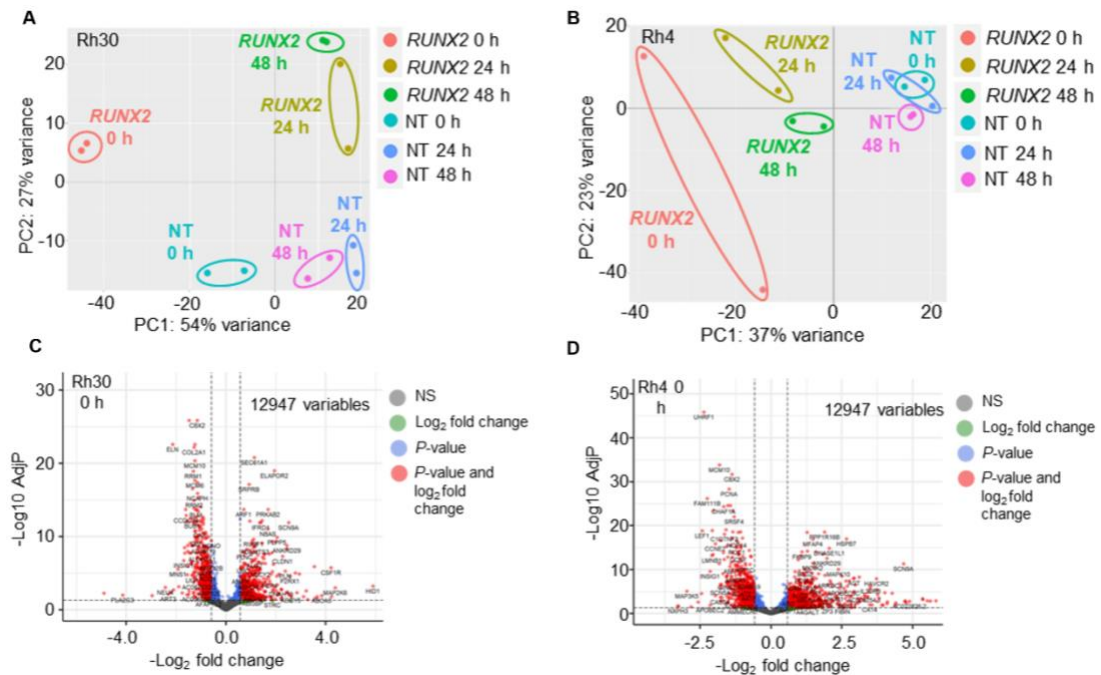


Figure 25: Transcriptomic alterations following *RUNX2* stable knockdown *in vitro*.

A,B, Data reduction to two-dimensions via biplot PCA shows consistent groups along the PC1 axis that correspond to Rh30 and Rh4 cells *RUNX2* knockdown at 0 h post selection (light red), 24 h post selection (olive), 48 h post selection (green), and negative control (NT) cells at identical time points (turquoise- 0 h, blue- 24 h, and pink- 48 h). C,D, Differentially expressed genes between shNT and sh4 *RUNX2* knockdown Rh30 and Rh4 cells at 0 h post selection. X-axis= $-\text{Log}_2\text{FC}$. Y-axis= $-\text{Log}_{10} \text{AdjP}$.

Differentially expressed genes in *RUNX2* KD samples were visualized via volcano plot (Figure 25C,D). Differentially expressed genes were included in a Gene Set Enrichment Analysis (GSEA) to confirm the key roles of *RUNX2* in FP-RMS. Two selected cancer hallmark and NCI gene-sets captured at 0 h, 24 h, and 48 h after selection largely became more enriched overtime in Rh30 and Rh4 (Figure 26A,B). Processed data for additional GSEA analysis is provided in Supplemental File 7. Gene sets involved in regulating myogenesis, skeletal muscle differentiation, myoblast differentiation, and apoptosis had positive enrichment scores that strengthened overtime following *RUNX2* KD in Rh30 and Rh4 (Figure 26C,D). Alternatively, gene-sets involved in positively regulating cell cycle, including *FOXM1*, had negative scores (Figure 26C,D) (177). Studies have reported that *FOXM1* is a promising RMS therapeutic target (178), and these results suggest that *RUNX2* inhibition secondarily inhibits a *FOXM1* gene-set signature. The most interesting enrichment plot conveyed that *RUNX2* KD upregulated the same gene-set signature that is upregulated with *PAX3::FOXO1* KD, suggesting that *RUNX2* inhibition may genetically and morphologically phenocopy direct inhibition of the FP-RMS driver (Figure 26C,D). These findings highlight the importance of *RUNX2* and its impact on FP-RMS biology.

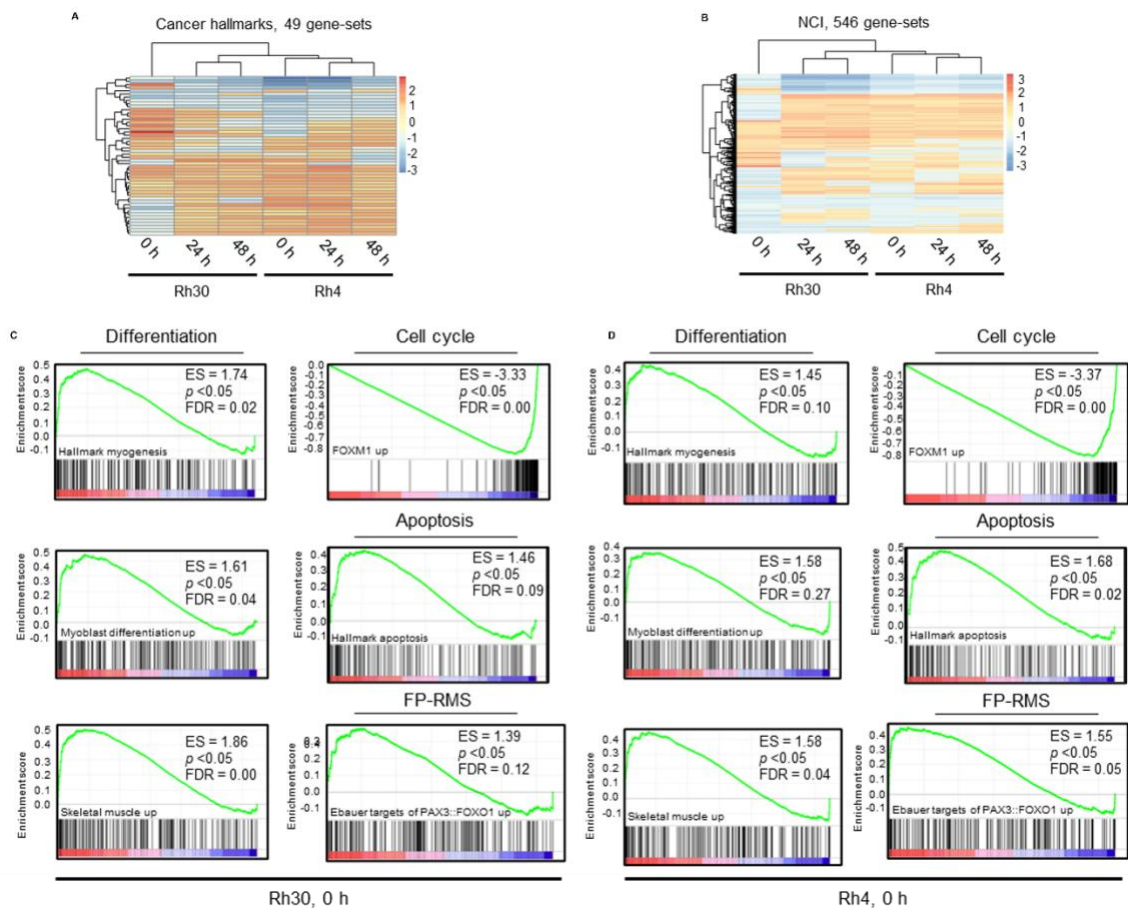


Figure 26: Gene set enrichment analysis (GSEA) following *RUNX2* stable knockdown *in vitro*.

A,B, Heat map based hierarchical cluster analysis following gene set enrichment analysis (GSEA) of Rh30 and Rh4 cells at selected timepoints (x-axis), and cancer hallmark (n=49) and NCI (n=546) gene-sets (y-axis). Key represents normalized enrichment score (NES). C,D Enrichment plots for Rh30 and Rh4 cells following *RUNX2* knockdown at 0 h post selection. Selected gene-sets characterize the effect of *RUNX2* knockdown on differentiation, cell cycle, apoptosis, and FP-RMS regulatory circuitry. Enrichment score (ES), *P*-values, and false discovery rate (FDR) are shown.

3.4.5 Conditional genetic *RUNX2* KD decreases PAX3::FOXO1 expression *in vitro* and impairs tumor growth *in vivo*

To prepare for evaluation of *RUNX2* KD *in vivo*, we engineered conditional (dox-inducible) shRNAs to *RUNX2*. Hairpin sequences sh2 and sh4 targeting *RUNX2* were subcloned into a doxycycline-inducible backbone and validated *in vitro* with Rh30 FP-RMS cells (Figure 27A,B) (Figure 27 legend is extended to two pages to maintain appropriate formatting). Cells

were cultured and treated with a range of doxycycline doses for 72 h; doxycycline-inducible KD phenocopied constitutively active KD (Figure 27C; Figure 23). Since mRNA-seq of *RUNX2* KD lead to increased gene expression of targets increased with *PAX3::FOXO1* KD, we performed qRT-PCR for *PAX3::FOXO1* and found *RUNX2* inhibition downregulated expression of the fusion transcript (Figure 27D). To determine the consequences of *RUNX2* inhibition *in vivo*, cells were grown and injected subcutaneously into the flanks of SCID/*beige* mice (Figure 27E; Figure 28A,B). Mice with *RUNX2* KD had significantly reduced tumor volume compared to control mice, suggesting that *RUNX2* inhibition attenuates oncogenic phenotypes *in vivo* (Figure 27E; Figure 28A,B). Tumors harvested from mice with sh2 *RUNX2* KD weighed significantly less than control tumors, while those from mice with sh4 *RUNX2* did not meet statistical significance, likely because tumors began to escape the growth suppressive KD effects (Figure 27E; Figure 28C). H&E of sh2 tumors did not show histological differences (Figure 27G, top row). IHC for Ki-67 and CC3 was performed to confirm whether the anti-proliferative and pro-apoptotic effects seen *in vitro* hold true *in vivo*; proliferation was not significantly decreased, but one tumor exhibited less Ki-67 staining. The effect on apoptosis was significantly increased by approximately 5-fold in all sh2 tumors with active *RUNX2* KD compared to control tumors (Figure 27G-I). H&E and IHC for sh4 tumors is ongoing. qRT-PCR for select genes evaluated *in vitro* were repeated with RNA from sh2 and sh4 tumors (Figure 27J; Figure 28D). *RUNX2* and *PAX3::FOXO1* expression decreased by ~40% for a subset of sh2 tumors (Figure 27J). In sh4 tumors, *RUNX2* was significantly decreased by 50% in 5 out of 6 mice (Figure 28D) and *PAX3::FOXO1* was decreased by 50% in all mice (Figure 28D). In sh2 tumors *MYOD1* and *OC* expression increased by 4-fold in some instances (Figure 27J), but in sh4 tumors *MYOD1* expression is significantly decreased (Figure 28D). Significant reduction of *RUNX2* and *PAX3::FOXO1* gene expression paired with a significant increase in *OC* expression validate that genetic changes observed *in vitro* are replicated *in vivo*. The variability in sh2 versus sh4 *MYOD1*

response is likely due to compensation of *RUNX2* transcription towards conclusion of the experiment or representative of tumor heterogeneity. In the future, we plan to complete mRNA-seq to determine if myogenic signatures are increased *in vivo* as *in vitro* and check other myogenic markers such as *MYOG*, *MYF5*, and *MYF6*.

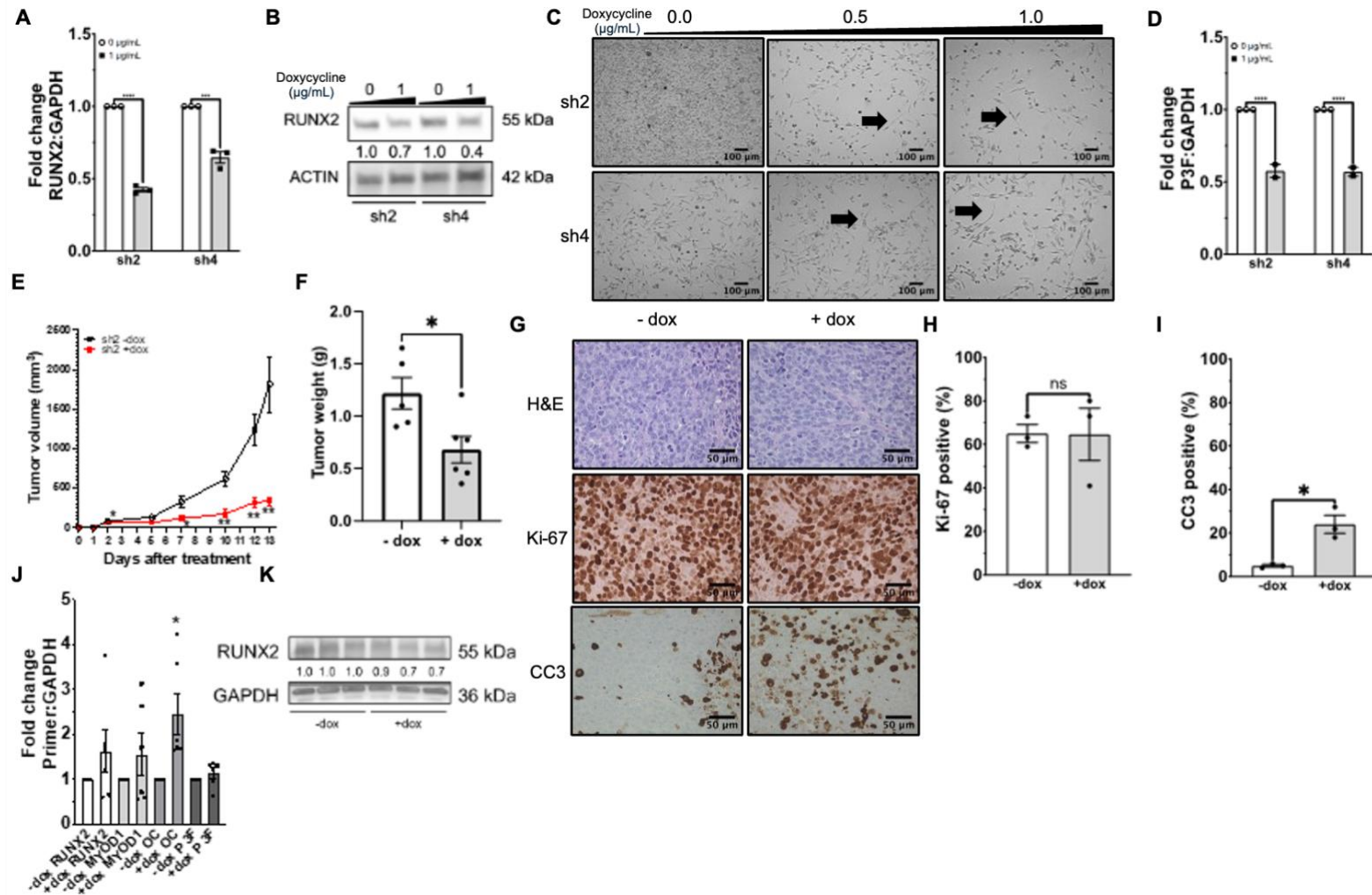


Figure 27: Doxycycline inducible *RUNX2* knockdown in Rh30 FP-RMS cells.

A, qRT-PCR for *RUNX2* 72 h after 1 $\mu\text{g}/\text{mL}$ doxycycline treatment. Black dots represent technical replicates. B, *RUNX2* protein expression in *RUNX2* knockdown cells (sh2, sh4) following treatment with 1 $\mu\text{g}/\text{mL}$ doxycycline for 140 h. C, Doxycycline inducible knockdown of *RUNX2* in Rh30 cells using two different shRNA constructs (sh2, sh4). Black arrows point to visible differentiated phenotypes. Cells were imaged at 10X magnification. Scale bars are 100 μm . D, qRT-PCR for *PAX3::FOXO1* expression 72 h after 1 $\mu\text{g}/\text{mL}$ doxycycline treatment in the *RUNX2* knockdown cells (sh2, sh4). Black dots are technical replicates. E, Tumor volume growth curves in mice engrafted with sh2 doxycycline inducible *RUNX2* knockdown Rh30 cells and with or without access to doxycycline chow. Stars above each day represent a significant difference between means of control versus treated tumors on that day. F, Tumors excised from the mice and weighed (g). Black dots represent independent biological replicates. G, Representative H&E images of excised tumors taken at 40X magnification plus immunohistochemistry for Ki-67 and CC3. Scale bars are 50 μm . H,I, Three representative tumors from each group (one shown) stained for Ki-67 and CC3 and quantified using ImageJ. J, qRT-PCR for *RUNX2*, *MYOD1*, *OC*, and *PAX3::FOXO1* expression following *RUNX2* knockdown *in vivo*. Black dots represent independent biological replicates. K, *RUNX2* protein expression following sh2 doxycycline inducible *RUNX2* knockdown Rh30 cells and with (n=3) or without (n=3) access to doxycycline chow.

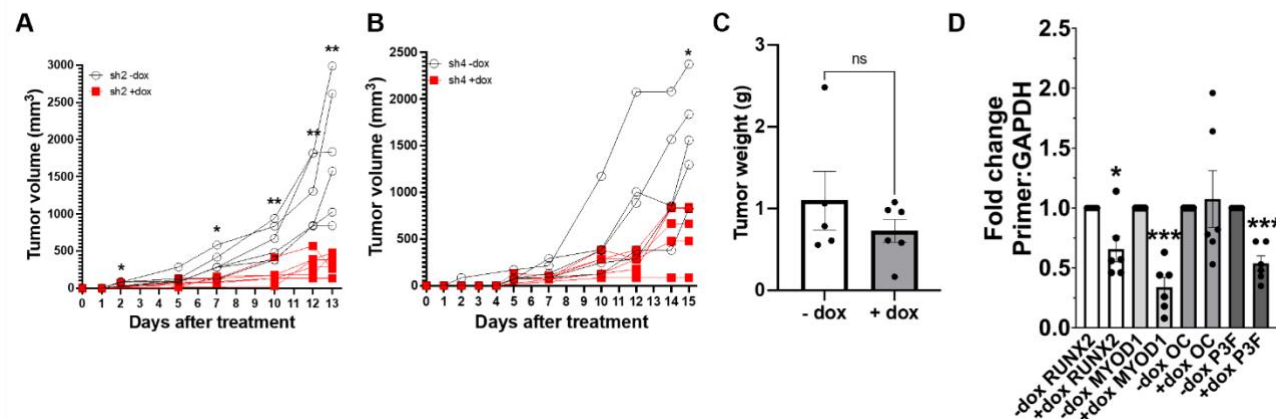


Figure 28: Additional *in vivo* experiments and expanded analyses.

A, Tumor volume spider plot in mice engrafted with sh2 doxycycline inducible *RUNX2* knockdown Rh30 cells and with or without access to doxycycline chow (see Figure 27). Each line represents a single mouse. B, Tumor volume spider plot in mice engrafted with sh4 doxycycline inducible *RUNX2* knockdown Rh30 cells and with or without access to doxycycline chow. Each line represents a single mouse. C, Tumors excised from the mice and weighed (g). Black dots represent independent biological replicates. D, qRT-PCR for *RUNX2*, *MYOD1*, *OC*, and *PAX3::FOXO1* expression following *RUNX2* knockdown *in vivo*. Black dots represent independent biological replicates.

3.4.6 Identification of a feed-forward loop between PAX3::FOXO1 and RUNX2

Since *RUNX2* KD altered expression of *PAX3::FOXO1* and its target genes, we next evaluated whether *PAX3::FOXO1* conversely regulated *RUNX2*. Mining of previously published mRNA-seq datasets showed that *RUNX2* but not *RUNX1* expression is decreased following lentiviral KD of *PAX3::FOXO1* in Rh4 FP-RMS cells (A,B) (Figure 29 legend is extended to the next page to maintain appropriate formatting) (41). Prior studies in Rh30 cells showed that *RUNX2* was rapidly inhibited following *PAX3::FOXO1* degradation (42). To expand *PAX3::FOXO1* KD findings, we transiently suppressed *PAX3::FOXO1* using siRNAs, and found that *PAX3::FOXO1* KD inhibited *RUNX2* expression by approximately 85% in Rh30 cells (Figure 29C,D). Taken together, these data suggest that *RUNX2* and *PAX3::FOXO1* can regulate one another (Figure 27D; Figure 29C,D). This relationship is supported by the direct binding of *PAX3::FOXO1* to *RUNX2* enhancer as determined by a previously published ChIP-seq dataset in Rh4 cells (Figure 29E) (41). Previous studies reported similar results in Rh30 cells using CUT&RUN (42), thus collectively these data suggest that *PAX3::FOXO1* binding to the *RUNX2* enhancer is not cell line-specific but likely occurs in all *PAX3::FOXO1* expressing cell lines (41,42). Additional ChIP-seq analyses reveal active histone marks (H3K27ac, H3K9ac, and H3K4me3) but inactive repressive marks (H3K27me3) at the *RUNX2* promoter, confirming that the *RUNX2* promoter is active when *PAX3::FOXO1* is bound to the *RUNX2* enhancer (Figure 29E). The core regulatory circuit of *PAX3::FOXO1* associated transcription factors regulate each other and finding *MYOD1* at the enhancer of *RUNX2* may indicate that *RUNX2* is an important target of the core regulatory circuit (Figure 29E); since *MYOD1* and myogenic signatures increase when *RUNX2* is KD *in vitro*, it is possible that *RUNX2* binds *MYOD1* as well as other myogenic enhancers in FP-RMS cells (Figure 23G; Figure 26C,D). This finding was validated in an additional cell line and expanded on in the previously published Rh30 CUT&RUN dataset where other *PAX3::FOXO1* complex proteins such as *PAX3*, *CDK8*, *RUNX1*, and *BRD4* localize at the

same enhancer alongside PAX3::FOXO1 (42). Additional tracks visualizing ATAC-seq and mRNA-seq data demonstrates that the *RUNX2* gene is open and expressed in the presence of PAX3::FOXO1, but lost with *PAX3::FOXO1* KD; potentially because of the ability of PAX3::FOXO1 to coordinate enhancer architecture and remodel chromatin of enhancers and super enhancers (41,42).

Given the regulatory effects of PAX3::FOXO1 on *RUNX2*, and *RUNX2* on *PAX3::FOXO1* and associated target genes, we investigated whether *RUNX2* KD impacted PAX3::FOXO1 protein expression. Indeed, inhibition of *RUNX2* resulted in decreased expression of PAX3::FOXO1 and endogenous FOXO1 in both Rh4 and Rh30 cells, signifying a novel mechanism wherein PAX3::FOXO1 protein and gene expression is dependent on the expression of *RUNX2* (Figure 29F,G). With longer *RUNX2* KD (144 h after selection), PAX3::FOXO1 and endogenous FOXO1 expression were almost completely absent (Figure 29H). Together, these findings establish a feed-forward loop between *RUNX2* and PAX3::FOXO1 that regulates FP-MS oncogenic phenotypes and regulatory gene networks.

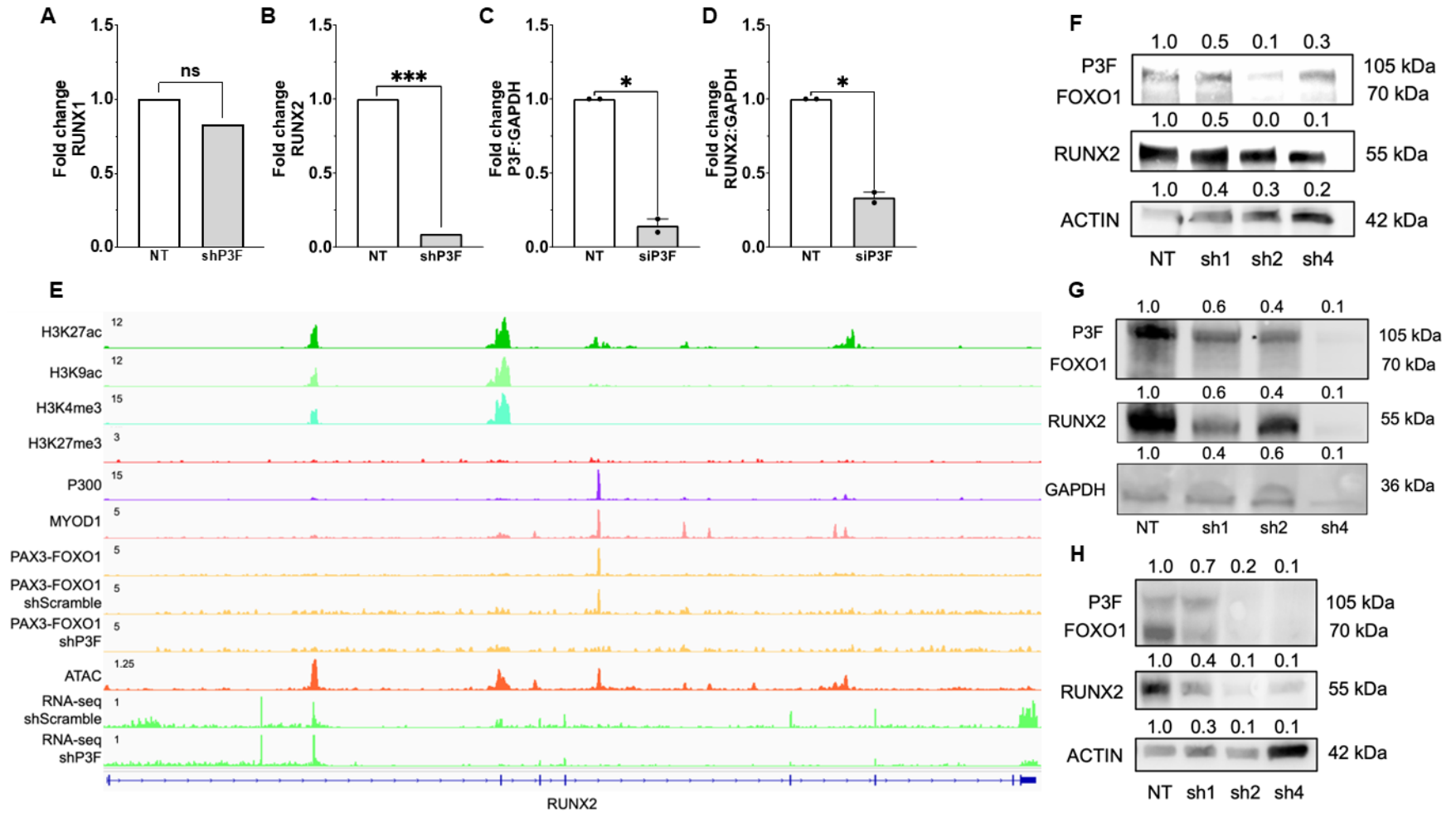


Figure 29: PAX3::FOXO1 and RUNX2 reciprocally regulate one another in FP-RMS.

A,B, Stable knockdown of *PAX3::FOXO1* in Rh4 cells affect on *RUNX2* and *RUNX1* expression. C,D, qRT-PCR for *PAX3::FOXO1* and *RUNX2* expression in *PAX3::FOXO1* transient knockdown Rh30 cells. Black dots are independent biological replicates. E, Genome browser view of *RUNX2*. Peaks for the top 9 rows reflect degree of DNA-binding of H3K27ac, H3K9ac, H3K4me3, H3K27me3, P300, MYOD1, and *PAX3::FOXO1* using ChIP-seq. Row 10 is open chromatin peaks from ATAC-seq, and rows 11 and 12 are mRNA-seq reads. All rows are in Rh4 cells, counts are in reads per million. F, *PAX3::FOXO1*, *FOXO1*, and *RUNX2* protein expression in negative control (NT) and puromycin selected *RUNX2* knockdown Rh4 cells after 48 h selection. G, *PAX3::FOXO1*, *FOXO1* and *RUNX2* protein expression in negative control (NT) and puromycin selected *RUNX2* knockdown Rh30 cells after 72 h selection. H, *PAX3::FOXO1*, *FOXO1* and *RUNX2* protein expression in negative control (NT) and puromycin selected *RUNX2* knockdown Rh30 cells 144 h after selection.

3.4.7 Pharmacologic inhibition of RUNX2 via the small molecule RUNX2 inhibitor CADD522 impairs FP-RMS tumor xenograft formation

To evaluate RUNX2 inhibition for clinical purposes, we investigated the efficacy of computer aided drug design molecule (CADD522), a commercially available small-molecule RUNX2 inhibitor previously tested pre-clinically in human breast cancer, Ewing sarcoma, and OS animal models (122,129,130,179), but not in FP-RMS models. To capture early genetic changes in response to CADD522 treatment, qRT-PCR of *RUNX2* significantly decreased with 1.0 μ M CADD522 treatment for 24 h (Figure 30A). Further *in vitro* investigation determined that treatment with 12 μ M CADD522, similar to *RUNX2* KD, resulted in decreased colony number (Figure 30B,C). Rh30 cells with 1.5 μ M and 3.0 μ M CADD522 for 72 h exhibited that drug treatment morphologically phenocopied genetic *RUNX2* KD (Figure 30D, top row). Next, we performed MF20 staining on Rh30 cells and found that CADD522 treatment induced myotubes, thus supporting RUNX2's effects on FP-RMS cell differentiation (Figure 30D, bottom row, E). qRT-PCR of *MYOD1*, and *PAX3::FOXO1* partially mimicked results seen with *RUNX2* KD in a dose-dependent manner, but *OC* expression did not change with 0.5 μ M and 1.0 μ M CADD522 treatment for 24 h suggesting mechanistic differences between the drug and KD, likely because of differing mechanisms of inhibition and off target effects on metabolism (Figure 30F-H) (129). Expanded *in vitro* studies using different doses of and exposure to CADD522 are warranted to fully elucidate its mechanism in FP-RMS.

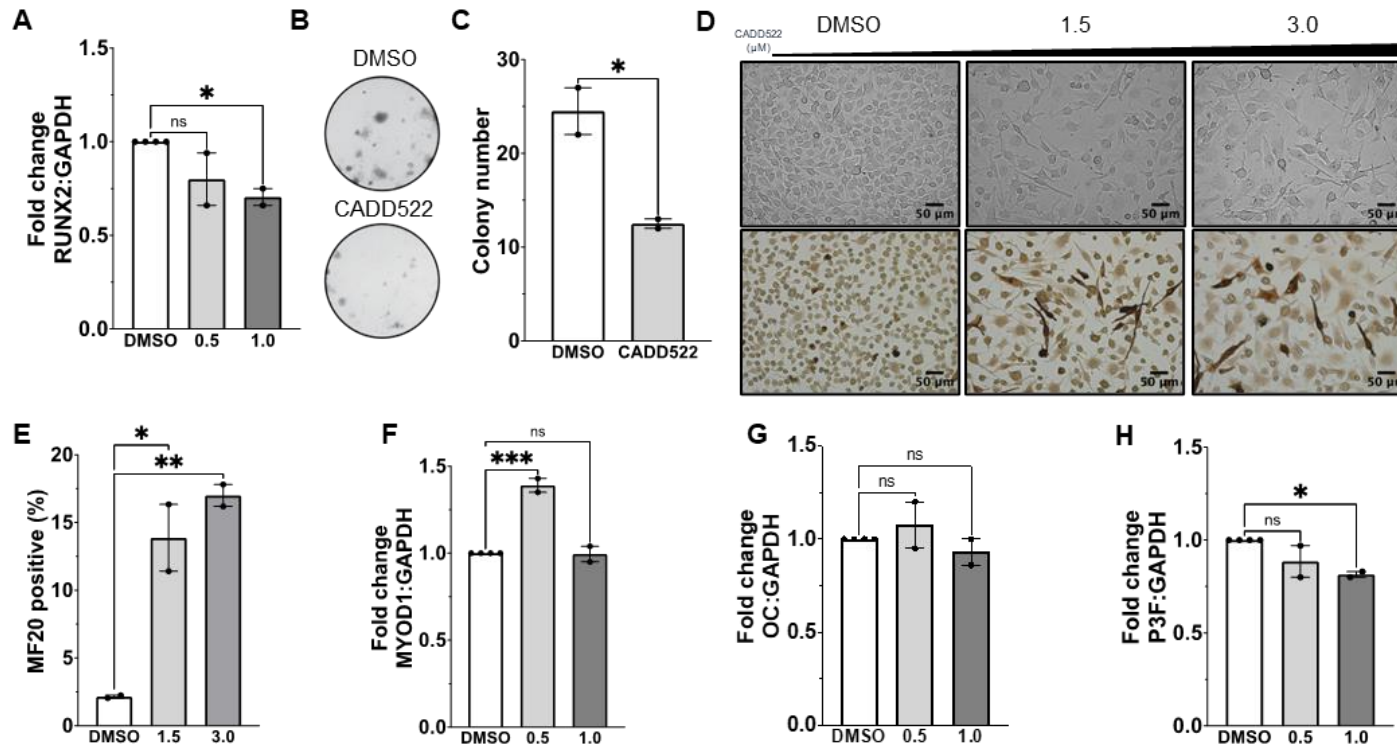


Figure 30: Rh30 cells treated with the RUNX2 small molecule inhibitor CADD522 *in vitro*.

A, qRT-PCR for *RUNX2* performed following 24 h of treatment with 0.5 μ M and 1.0 μ M of CADD522 *in vitro*. Black dots are independent biological replicates. **B**, CADD522 treatment effects on colony formation *in vitro*. Cells were treated with a 12 μ M dose every other day for 14 d. **C**, Colony number after CADD522 treatment. Black dots represent technical replicates. **D**, Rh30 cells stained with the myogenic marker sarcomere myosin (MF20) when treated with a negative control (DMSO) and different CADD522 concentrations over 72 h. Images were captured at 20X magnification. Scale bars are 50 μ m. **E**, Quantification of MF20 positive cells (dark brown) versus MF20 negative cells (light brown) following CADD522 treatment. **F**, **G**, **H** qRT-PCR for *MYOD1*, *OC*, and *PAX3::FOXO1* performed following 24 h of treatment with 0.5 μ M and 1.0 μ M of CADD522 *in vitro*. Black dots are independent biological replicates.

Finally, to determine whether CADD522 is effective at suppressing tumor growth and extending survival *in vivo*, we injected Rh30 cells subcutaneously into the flanks of SCID/*beige* mice and treated them with 10 mg/kg of drug 3x weekly once tumors were 200 mm³. Mice in the drug treatment group had significantly increased survival and reduced tumor volume (Figure 31A,B). Mice treated with CADD522 also had significantly increased survival ($p=0.0017$) (Figure 31C). To characterize tumors further, we performed IHC for Ki-67 and CC3 and determined that drug treated tumors were significantly less proliferative and significantly more apoptotic (Figure 31D-F). Finally, qRT-PCR for *RUNX2*, *MYOD1 OC*, and *PAX3::FOXO1* (Figure 31G) closely resembled *in vitro* and *in vivo* findings seen in Figure 23, Figure 27, and Figure 28, except for *PAX3::FOXO1* expression, which was variable, and *OC* expression, which was significantly decreased. These findings suggest that dose optimization and continuing studies are required to fully determine the mechanistic effects of CADD522 in FP-RMS. We are currently repeating *in vivo* CADD522 studies and expanding our cohort to include male and female mice.

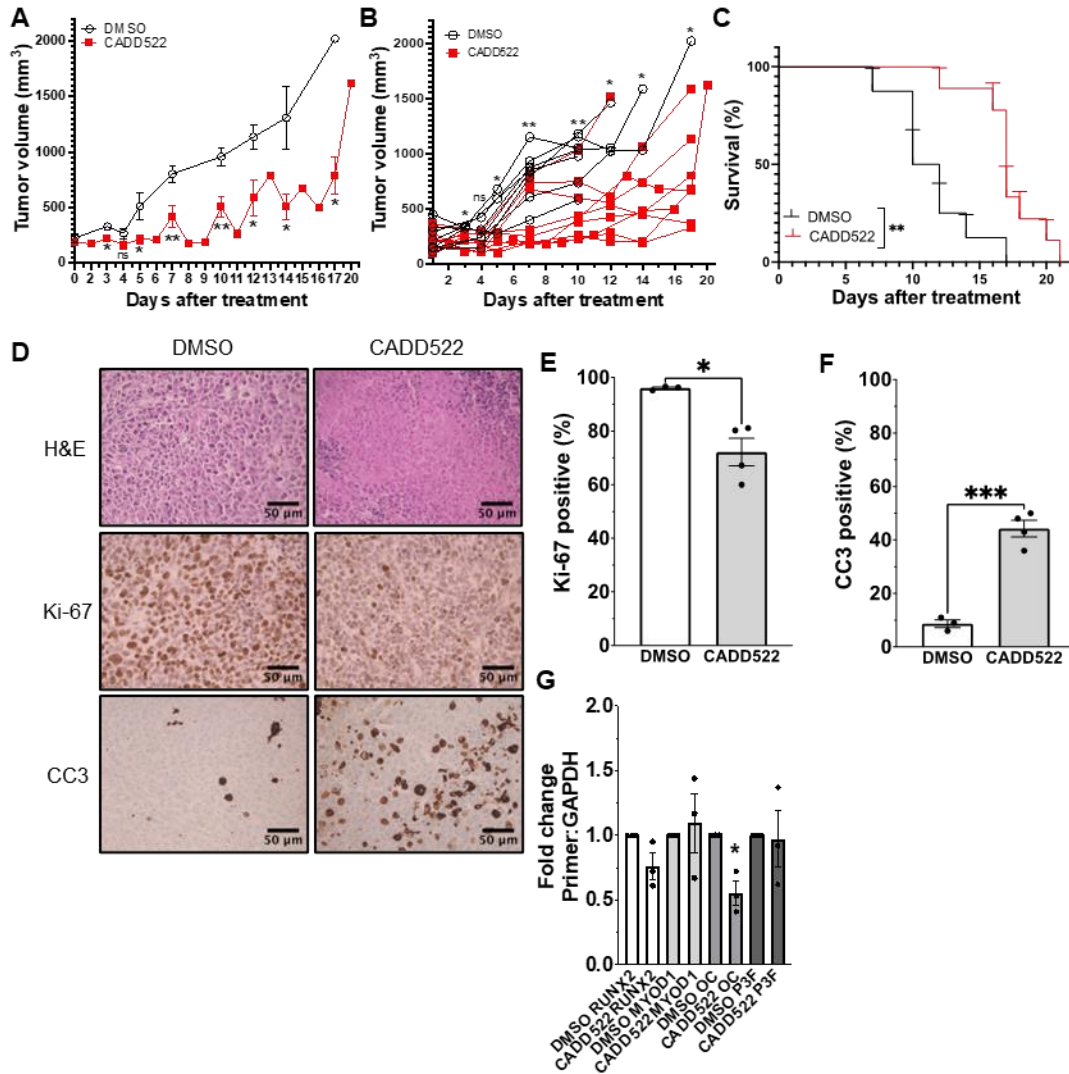


Figure 31: Rh30 cells treated with the RUNX2 small molecule inhibitor CADD522 *in vivo*.

A, Tumor volume growth curves with (n=9) or without 10 mg/kg CADD522 (n=8). **B**, Tumor volume spider plot in mice engrafted with wild type Rh30 cells with or without CADD522 treatment (see Figure 30). Each line represents a single mouse. Stars above each day represent a significant difference between means of control versus treated tumors on that day. **C**, Kaplan-Meier survival curve for mice treated with 10 mg/kg CADD522. Stars above each day represent a significant difference between means of control versus treated tumors on that day. **C**, H&E stains on excised tumors and immunohistochemistry (IHC) for Ki-67 and CC3 with and without CADD522 treatment. Images were captured at 40X magnification. Scale bars are 50 μm. **E**, **F**, Ki-67 and CC3 quantification. **D**, qRT-PCR for *RUNX2*, *MYOD1*, *OC*, and *PAX3::FOXO1* expression following CADD522 treatment *in vivo*. Black dots represent independent biological replicates

3.4.8 microRNA mediated regulation of RUNX2 in ARMS patient samples

Since RUNX2 expression is also known to be regulated by microRNAs (miRNAs), specifically miR-34a (180), in parallel with our mRNA-seq of primary tumor tissue, we also performed sRNA-seq, to identify novel and validate previously published miRNAs responsible for regulating key RMS genes. Representative frequency mapping of miRNA expression in wild-type and RMS tissues revealed that SkM tissues predominantly expressed miRNAs at 22 nt, while RMS tissues exhibited two major peaks: one at 22 nt for miRNAs and another at 32 nt for tRNA-derived fragments (tRFs) and Y-RNA small RNA (ysRNAs) (Supplemental File 8A). The PCC plot demonstrated a strong linear correlation between the sample sets, indicating consistency within each group (Supplemental File 8B). PCA further supported these findings, showing distinct clustering along the PC1 axis that corresponded to ARMS, ERMS, and SkM tissues (Supplemental File 8C). Approximately 15M reads per sample were obtained (Supplemental File 2). Hierarchical cluster analysis of selected miRNAs in ARMS tissues compared to SkM revealed significant changes in miRNA expression, providing insight into their role in regulating RMS biology (Supplemental File 8D). Similarly, a heatmap of selected miRNAs across ERMS tissues compared to SkM highlighted additional miRNAs involved in RMS regulation (Supplemental File 8E). Processed data for all miRNAs can be found in Supplemental File 9. miR-34a was identified as highly expressed in all RMS histological subtypes coinciding with its known role of supporting *RUNX2* expression in patients with calcific aortic valve stenosis (Supplemental File 8; Supplemental File 9) (122). These data suggest that RUNX2 is likely regulated by specific miRNAs in FP-RMS, some of which may make interesting future therapeutic targets, and be critical to RUNX2-PAX3::FOXO1 signaling in FP-RMS.

3.5 Discussion

RMS is the most common soft tissue sarcoma diagnosed in the pediatric population (9,13,15,155). Prior studies have revealed that around 1 in 4 RMS cases harbor a *PAX3/7::FOXO1* driver mutation (9,13,15,155). The encoded fusion oncoproteins create *de novo* enhancers (41,42) that appear to contribute to tumorigenesis and eventually tumor progression; considered high-risk disease with higher chemoresistance and increased metastatic propensity (15,155,181). The *PAX3/7::FOXO1* oncoproteins are ideal targets for cancer drugs because they are unique to RMS cells; however, they possess no catalytic activity and are intrinsically disordered proteins with ill-defined binding pockets for small molecule inhibitors, meaning alternative strategies are required to target RMS cells. Here we perform sequencing of pediatric primary tumor samples and cross reference publicly available datasets to identify *RUNX2*, long considered a bone development transcription factor, as being critical for the oncogenic properties of FP-RMS, a cancer more associated with the skeletal muscle lineage. Short read sequencing of patient tumors was employed for differential expressed gene analysis using the original histological diagnosis, future work will employ long read sequencing and diagnosis based on fusion status going forward, in combination with short read (Illumina) sequencing. Data mining from non-malignant tissue and developmental pathways indeed places *RUNX2* squarely in myogenic processes. For example, GTExPortal snRNA-seq data of skeletal muscle tissue revealed that *RUNX2* is expressed in 2.43% of skeletal muscle myocyte cells (Figure 21A), supporting its context-specific function in normal tissue. There is evidence that *RUNX2* is critical for cell fate decisions (e.g. bone and muscle lineages), since some muscle progenitor cells are bipotent and can be directed towards osteogenic or myogenic lineages depending upon modifications by lysine methyltransferases (*LSD1*) or lysine demethylases (*MLL4*), which have opposing functions at *RUNX2* enhancers to regulate myogenic versus osteogenic differentiation (87). While the relationship between *PAX3::FOXO1* and *RUNX2* is largely unknown, several

studies have interrogated the relationship between FOXO1 and RUNX2 in other contexts (180,182).

In prostate cancer, *RUNX2* governed migration and invasion is negatively regulated by increased *FOXO1* expression; in early osteoblast differentiation, amino acids 360-456 of FOXO1 directly interacts with amino acids 242-258 of RUNX2 to dissociate RUNX2 from the *osteocalcin (OC)* promoter (180,182). In the case of FP-RMS, it is likely that RUNX2 upregulation contributes to the core regulatory circuitry maintaining the cells in a myoblastic state, since when we suppress *RUNX2*, genes responsible for myogenesis are upregulated, while genes for cell cycle inhibition and PAX3::FOXO1 specific gene signatures mediating the anti-apoptotic function of PAX3::FOXO1 (181) are downregulated (Figure 32). Mechanistically, this appears due to a feed-forward loop, whereby PAX3::FOXO1 transcriptionally upregulates *RUNX2*, and *RUNX2* maintains PAX3::FOXO1 transcript levels, sustaining PAX3::FOXO1 signaling to genes such as *MYCN*, *POU4F1*, *RASSF4*, and *FGFR2*. At the chromatin level, it is more complex, since when a PAX3::FOXO1 regulated-enhancer of *RUNX2* was deleted following depletion of PAX3::FOXO1, *RUNX2* expression decreased, but when the non-PAX3::FOXO1 enhancer was deleted, the effect was the same; therefore, two elements are independently required to maintain *RUNX2* gene expression (42). These data suggest that multiple mechanisms likely regulate *RUNX2* in FP-RMS, some of which may be pertinent to FN-RMS. For example, single cell transcriptomic profiling of FN-RMS cells identified a molecularly-defined tumor-propagating subpopulation that shares similarity to bipotent, MSCs capable of differentiating into muscle and osteogenic cells (176). These observations, in combination with our finding that *RUNX2* expression is high not only in FP-RMS but also in histologically defined ERMS, SCRMS, and PRMS patient samples (strongly associated with FN-RMS) suggest that *RUNX2* oncogenic signaling may be relevant beyond its relationship with PAX3::FOXO1 and FP-RMS (181), and may be a pan-RMS target.

A relatively unexplored but intriguing direction supported by our work is the relationship of RUNX1 to RUNX2 in FP-RMS. In non-cancer situations, cooperation of RUNX1 and RUNX2 are required to regulate sternal morphogenesis and the commitment of MSCs to chondrocytes (78,84,85). Several platforms and the literature highlight RUNX1 as a prognostic biomarker across many human malignancies including hepatocellular carcinoma and gastric cancer. On the other hand, RUNX1 is tumor-suppressive in lung and prostate cancer (183). In breast cancer stem cells, RUNX1 and RUNX2 serve opposing roles (78). Germline mutations of *RUNX1* are associated with myeloid malignancies, and *RUNX1* is required for growth and survival of multiple leukemia cell types (184). Therefore, it is likely that the behaviors and contributions of RUNX1 and RUNX2 to cancer is context-dependent. Here, we found that *RUNX1* is upregulated in ERMS but is not differentially expressed in ARMS (ERMS: $\log_2FC=1.4$); survival data suggests that low *RUNX1* expression is correlated with poor outcome (41). Regarding mechanism, there are conflicting reports on whether *RUNX1* is transcriptionally regulated by PAX3::*FOXO1*. Through analysis of published datasets, we found that shRNA KD of PAX3::*FOXO1* did not affect *RUNX1* expression, and that PAX3::*FOXO1* did not bind *RUNX1* enhancers (41). This finding may in part explain why PAX3::*FOXO1* was found to regulate RUNX1 enhancer independently, but regulated RUNX2 enhancer alongside other DNA-binding factors such as MYOD1 (42). However, RUNX1 is part of the PAX3::*FOXO1* protein interactome; and that *RUNX1* is downregulated upon loss of PAX3::*FOXO1* protein within 6 h of dTAG-47 treatment (42). These data may be of significance for the future understanding of the role of RUNX1 in FP-RMS and deciphering a potentially coregulatory relationship between RUNX1 and RUNX2 in FP-RMS.

The clinical relevance of RUNX2 rests on its use as a biomarker of outcome and as a therapeutic target. Because our sample size was small, it is too early to say whether RUNX2 is a bona fide biomarker in FP-RMS. RUNX2 is a prognostic cancer biomarker in diseases such as

OS, blastic plasmacytoid dendritic cell neoplasm (BPDCN), breast cancer, and prostate cancer; indirect and direct biological functions of RUNX2 regulate oncogenic processes such as cancer stemness, metastasis, proliferation, cell cycle regulation, and apoptosis (68,104,105,122,130,185,186). In BPDCN, the plasmacytoid dendritic cells (pDCs) *RUNX2* super-enhancer is hijacked to activate *MYC* in and *RUNX2* expression to promote proliferation (185).

However, given the slowing of tumor xenograft growth by either genetic or CADD522 pharmacologic inhibition of RUNX2, the value of RUNX2 as a therapeutic target should be pursued. Transcription factors including RUNX2 remain challenging as drug targets because of their lack of catalytic activity and their intrinsically disordered state, lacking binding pockets for small molecules. However, the RUNX2-directed agent used here, CADD522, is in development for clinical trials (187), and others are developing allosteric inhibitors to RUNX2 and CBF β inhibitors (188). Like CADD522, active inhibitor compounds demonstrate anti-tumor activities with concentrations that are achievable *in vivo* (122,130,188). There may also be indirect ways to target RUNX1/RUNX2. The small molecule imatinib, FDA-approved for the treatment of multiple hematologic malignancies, is being examined in clinical trials as a means to block tyrosine phosphorylation of RUNX1, thereby restoring RUNX1 activity, especially in patients with RUNX1 germline mutations (189,190). These data highlight the importance of RUNX-targeted therapies across various cancer types and the demand for other RUNX-targeted pharmacologic approaches such as PROTACS and molecular glues.

Finally, we query what other pathways may control RUNX2 expression, since targets in these pathways may also be required to keep RUNX2 expression high. For example, HDAC4, which is a direct negative regulator of *RUNX2* promoter accessibility (191), was downregulated in both ARMS ($\log_2FC=1.1$) and ERMS ($\log_2FC=2.14$) samples, which might underlie the

observed *RUNX2* upregulation. Because microRNAs are known to regulate HDAC4, we performed sRNA-seq using the same samples subject to mRNA profiling. Most of the miRNAs known to negatively regulate *HDAC4* – therefore permitting expression of HDAC4 targets including *RUNX2* - were paradoxically downregulated [e.g. miR-140 (both 3p and 5p isoforms), muscle specific miR-1 and miR-206] except for miR-155, which was upregulated (ARMS: $\log_2FC=2.0$; ERMS: $\log_2FC=3.1$). A future study could directly test a miR-155 - HDAC4 - *RUNX2* axis in RMS because miR-155 was previously reported as a poor prognostic marker in sarcoma; the current data might explain the causal mechanism for the previously reported observation (192). To provide future directions, all differentially expressed microRNAs were funneled through the DepMap (Supplemental File 8) to identify microRNAs exclusively shared between all RMS histological subtypes (175). The 81 exclusively shared microRNAs, which included miR-140 isoforms and miR-155, can be found in Supplemental File 9.

In summary, here we have corroborated the upregulation of *RUNX2* in FP-RMS and other RMS variants and newly identified a feed-forward loop, whereby PAX3::FOXO1 transcriptionally upregulates *RUNX2*, and *RUNX2* supports the expression of PAX3::FOXO1. We have demonstrated that loss of *RUNX2* in FP-RMS abrogates oncogenic phenotypes *in vitro*, and that genetic or pharmacologic blockade of *RUNX2 in vivo* impairs FP-RMS tumor growth. Future studies will focus on the development of *RUNX2* as therapeutic target and the molecular mechanisms of *RUNX2* regulation.

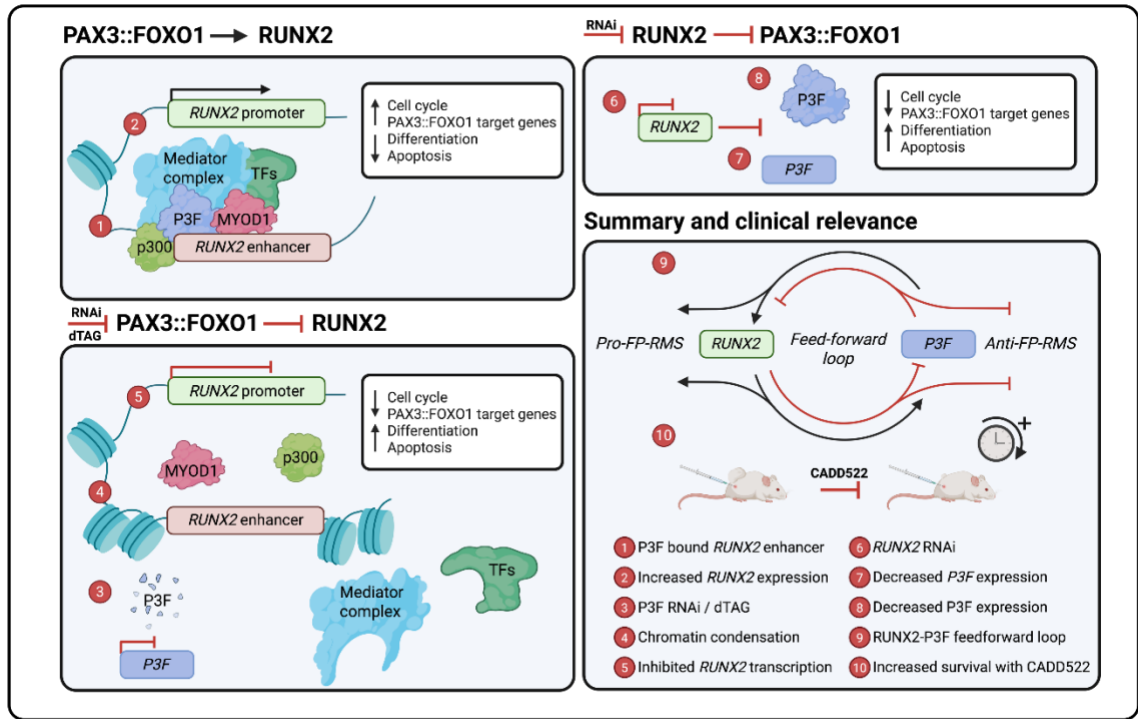


Figure 32: PAX3::FOXO1 transcriptionally upregulates *RUNX2* expression to prevent FP-RMS terminal differentiation and apoptosis via the defined regulatory circuitry.

3.6 Conflict of interest statement

CML's spouse is founder and owner of Grid Therapeutics, which is developing a monoclonal antibody for adult lung cancer. CML's lab has received funding from Ryvu. Neither of these are related to the research in this manuscript. DG reports patents EP3897609B1 and WO2023209077A1.

3.7 Acknowledgements

We thank members of the NCI FusOnC2 group and the laboratories of Dr. Gerry Blobel, Dr. Tammara Watts, and Dr. Michael Deel (Duke) for helpful discussions. We thank Dr. Katherine Gonzales, Dr. Xiangfeng Shen, Dr. Edward O'Brien, and Dr. Manqi Zhang for assistance with IHC and imaging. We thank Dr. John Bushweller for participating in helpful conversations about *RUNX2* pharmacological inhibition. We

thank Angelica Velasquez, Dr. Thomas Whitlow, and Dr. Purushothama Tata for their contributions to Figure 27 and Figure 28; in the updated manuscript submission, these individuals will be added as authors. We thank the Duke University BioRepository and Precision Pathology Center (Duke BRPC; supported by P30CA014236) and the NCI's Cooperative Human Tissue Network (CHTN (RRID:SCR_004446); supported at Duke University by UM1CA239755 for processing histological tissues. CML's lab and team was supported by NIH grant 1U54CA231630 (to CML), NIH grant 5T32GM142605-03 (supporting EAM), and a Duke OBGE Precision Genomics Collaboratory Grant (to EAM). SW was supported by the Pediatric Oncology Student Training (POST) Program. AM was supported by the CureSearch for Children's Cancer Acceleration Initiative Award. AJ was supported by the CA230526 Department of Defense Grant. AC was supported by the NSF Computers in Science and Math Undergraduate Education award 1834159. DG's lab and members, ME, AS were supported by Children with Cancer UK and donations made to the Childhood, Adolescent and Young Adult Cancer Research Programme at the University of East Anglia. The authors thank Dionne Wortley for support with obtaining patient samples. Figure 19A, Figure 23D, Figure 32, and Supplemental File 8A were Created in BioRender (Mendes, E. (2025) <https://BioRender.com/26c5ptj>, <https://BioRender.com/tk0t2im>, <https://BioRender.com/kggsksv>).

4. Laying the foundations for future interrogation of RUNX2-Hippo pathway protein interactions

The purpose of this section is to present preliminary data to inform future directions for the Linardic laboratory and our continued collaborations. I would like to acknowledge Michael Deel's, MD help as a collaborator on preliminary TAZ studies and for providing mass spectrometry and mRNA-seq results related to his ongoing, unpublished study. Please note that I have limited sharing permissions, for additional questions related to the datasets and methodology, please reach out to Michael.Deel@cchmc.org.

4.1 Introduction

As described in section 1.4 and Chapter 2 the RUNX family of transcription factors participates in crosstalk with many members of the Hippo pathway such as YAP and TAZ, but at the time of these findings, there were no reports of an association between RMS and RUNX1, -2, or -3. In Chapter 2 this work began investigating the consequences of MST1 loss-of-function and established that RUNX motifs were enriched when MST1 was inhibited. Therefore, a logical next step was to begin interrogating the relationships between RUNX transcription factors and the Hippo pathway in FP-RMS. Many sources have documented the relationship between RUNX2, YAP, and TAZ in promoting oncogenic phenotypes (53,89). qRT-PCR of *RUNX2* following KD with sh4 *in vitro* and *in vivo* found that *YAP*, *TEAD*, and *WWTR1/TAZ* expression were significantly decreased. Co-immunoprecipitation (IP) studies and IP-mass spectrometry (IP-MS) studies revealed direct protein-protein interactions between PAX3::FOXO1, TAZ, RUNX1, -2, and -3. Last, *RUNX2* was significantly decreased following *YAP* and *WWTR1/TAZ* KD. These studies suggest that RUNX2 and TAZ may participate in a feed-forward loop; additionally, it is possible that PAX3::FOXO1 forms a protein complex with RUNX2 and TAZ to promote pro-FP-RMS gene signatures.

4.2 Methods

4.2.1 Generation of cell lines and constructs

Please refer to section 2.2.1.

4.2.2 mRNA-seq of Rh30 and Rh4 cells

Please refer to section 3.3.5.

4.2.3 Co-immunoprecipitation

Co-immunoprecipitation (Co-IP) experiments were completed with the help of Michael Deel, MD as a collaborator on this project. Michael Deel, MD created Rh4 flag-tagged TAZ mutants, 106 Δ , Δ WW, and Δ 304 using site-directed mutagenesis followed by lentiviral transduction as described in section 3.3.6. Rh4 cells harboring either flag-tagged TAZ mutants or endogenously flag-tagged P3F (Rh4-Flag) were transfected in two, 10 cm plates of Rh4 cells, pelleted at 72 h following selection, and prepared for protein extraction. Co-IP was performed using the Dynabeads Co-IP Kit (Life Technologies, #14321D) according to the manufacturer's protocol. Antibodies used for each stage of IP and immunoblotting can be found in Table 7.

Table 7: Co-IP Antibodies: RUNX2-TAZ-PAX3::FOXO1 Interaction Studies.

Cell Line	IP Antibody, Catalog No., Volume	Blot Antibody, Catalog No.
Rh4 flag-tagged mutants	Flag M2, Sigma #F1804, (5 μ L)	Flag M2, Sigma #F3165
	IgG R, CST #2729, (2.5 μ L)	FOXO1, CST #2880
	IgG M, Sigma #12371, (2.5 μ L)	RUNX2, CST #12556
Rh4-Flag (P3F)	Flag M2, Sigma #F1804, (5 μ L)	Flag M2, Sigma #F3165
	TAZ, CST #4883 (5 μ L)	TAZ, CST #4883
	IgG R, CST #2729, (2.5 μ L)	RUNX2, CST #12556
	IgG M, Sigma #12371, (2.5 μ L)	

4.2.3 Immunoblotting

Please refer to section 2.2.2.

4.2.4 Statistics

Please refer to section 3.3.17.

4.3 Results and discussion points

Please note that in this section, I will include discussion points alongside the results to better guide readers since this is not a published study. Additional discussion points can be found in section 4.3.4.

4.3.1 *In vitro* and *in vivo* KD of *RUNX2* in FP-RMS cell lines impairs Hippo signaling

Using mRNA-seq data from figure 25, figure 26, and supplemental file 6 we determined the effect of *RUNX2* KD on *WWTR1/TAZ*, *YAP1*, and *TEAD1* in Rh30 and Rh4 FP-RMS cells (Figure 33A). At 24h and 48 h after selection in Rh30 cells (Figure 33B) and at 0 h, 24 h, and 48 h after selection in Rh4 cells (Figure 33C), *WWTR1/TAZ* expression was significantly decreased. This suggests that *WWTR1/TAZ* may be directly downstream of *RUNX2* in FP-RMS, and that *WWTR1/TAZ*'s expression is dependent on the expression of *RUNX2*. *RUNX2* KD in Rh30 had an insignificant effect on *YAP1* and *TEAD1* expression (Figure 33A), but at 24 h in Rh4 cells, *YAP1* and *TEAD1* expression were decreased by approximately 50% (Figure 33D,E). It is possible that *CDK4* amplification in Rh30 cells (193), which is not present in Rh4 cells, may bypass the effects of *RUNX2* inhibition by promoting *YAP1* stability as it does in hepatocellular carcinoma progression (194).

Next, we performed gene set enrichment analysis (GSEA) to identify Hippo-associated gene signatures using our previously described mRNA-seq dataset (Supplemental File 7). *RUNX2* KD in Rh30 and Rh4 resulted in a negative normalized enrichment score (NES) for the *YAP/TAZ* target genes that rely on *BRD4* expression and are downregulated when *BRD4* is inhibited with a BET inhibitor JQ1 (Table 8) (195). *BRD4*, *YAP*, and *TAZ* are all part of the FP-

RMS core regulatory circuitry (39,47), and in triple negative breast cancer, YAP/TAZ bound enhancers interact with BRD4 and PolIII to promote cancer growth (195). In mouse osteoblasts, Brd4 does not directly bind Runx2 instead, Brd4 occupies the same enhancer sites as Runx2 in the early stages of osteogenic differentiation (196). Since the genes in this dataset are downregulated when BRD4-YAP-TAZ mediated signaling is inhibited, it is possible that inhibiting RUNX2 serves an indirect/direct role in the ability of BRD4 to engage YAP/TAZ. Finally, we investigated our *WWTR1/TAZ* expression following *RUNX2* KD *in vivo* and found that *WWTR1/TAZ* expression was significantly decreased (Figure 34). Combined, these data suggest that *WWTR1/TAZ* is potentially directly downstream of RUNX2. To validate our findings, we have to perform ChIP-seq following *RUNX2* KD in FP-RMS cells.

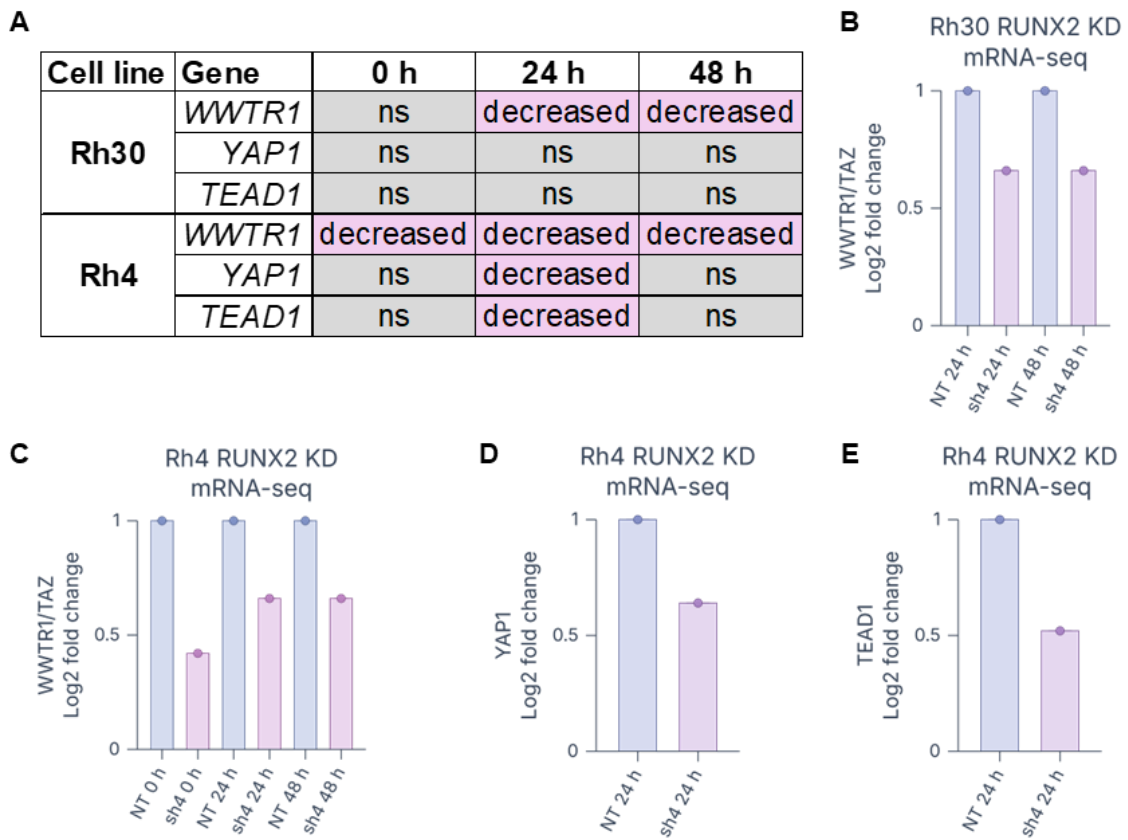


Figure 33: Hippo pathway alterations following *RUNX2* stable knockdown *in vitro*.

Stable knockdown of *RUNX2* in Rh4 and Rh30 cells using sh4 (see Figure 25 and Figure 26 in Chapter 3). A, Panel displaying a subset of Hippo genes, *WWTR1/TAZ*, *YAP1*, and

TEAD1 from mRNA-seq dataset described in Chapter 3. Cells highlighted in grey did not show a significant increase or decrease in expression following *RUNX2* KD (ns). Cells in magenta represent genes that were significantly decreased following *RUNX2* KD. B, mRNA-seq for *WWTR1/TAZ* expression at 24 h and 48 h after selection in Rh30 cells. C, mRNA-seq for *WWTR1/TAZ* expression at 0 h, 24 h, and 48 h after selection in Rh4 cells. D,E mRNA-seq for *YAPI* and *TEAD1* expression 24 h after selection in Rh30 cells. Panels in B-E were created in Graphmatik.io. Significant is $p < 0.05$.

Table 8: NESs and FDRs of YAP/TAZ target gene signature for genes that are dependent on BRD4.

GSEA from mRNA-seq of stable knockdown of RUNX2 in Rh4 and Rh30 cells using sh4 (see Figure 25 and Figure 26 in Chapter 3 and Supplemental File 7). NES and FDR for Rh30 and Rh4 at 0 h, 24 h, and 48 h post selection are displayed below.

Cell line	NES/FDR	0 h	24 h	48 h
Rh30	<i>NES</i>	-2.32	-1.53	-1.73
	<i>FDR</i>	0.00	0.14	0.02
Rh4	<i>NES</i>	-2.36	-1.01	-1.27
	<i>FDR</i>	0.00	0.56	0.34

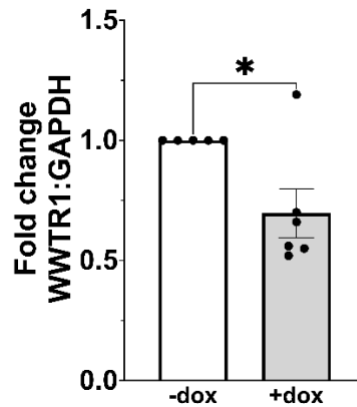


Figure 34: *WWTR1/TAZ* alterations following *RUNX2* conditional knockdown *in vivo*.

Please refer to Figure 28 for original experiment using sh4 to KD *RUNX2* in Rh30 cells *in vivo*.

4.3.2 *RUNX2*, *PAX3::FOXO1*, and *TAZ* directly bind one another in FP-RMS

Next, we aimed to characterize the direct relationships between *RUNX2*, *PAX3::FOXO1*, and *TAZ*. In breast cancer and osteoblasts, *RUNX2* and *TAZ* are known to directly interact with one another, at the WW domain of *TAZ* and the PY motif found in *RUNX2* as shown in Figure 12 in Chapter 1 (75,89,134). To identify potential *RUNX2*-Hippo pathway mechanisms described we did Co-IP of Rh4 FP-RMS cells expressing *TAZ* mutants lacking the WW domain (Δ WW), TEAD binding domain (106 Δ), and TAD/PDZ binding domain (Δ 304) of *TAZ* (Figure 35). When

we immunoprecipitated (IP) TAZ and blotted for P3F and RUNX2 in Rh4 cells expressing flag-tagged TAZ mutants, we found that the P3F and RUNX2 bands were diminished in the Δ WW lane but absent in the 106 Δ lane (Figure 36). Thus, TAZ-RUNX2 and TAZ-P3F interactions may require TEAD binding domain and WW domain in FP-RMS.

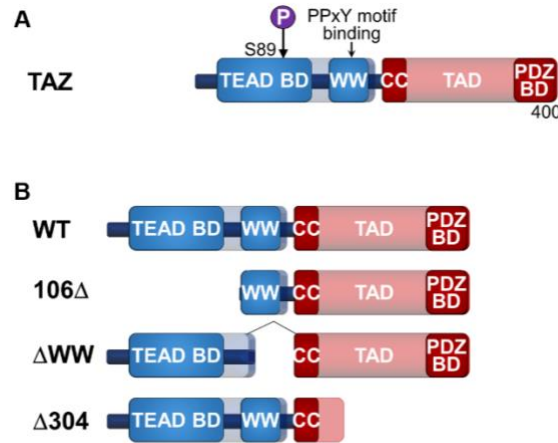


Figure 35: TAZ mutant protein domain structures.

Graphic of TAZ wild type (WT) and mutant protein domains. A, The human TAZ protein encodes 400 amino acids. The TEAD-binding domain binds TEAD transcription factors which bind DNA. S89 in the TEAD-binding domain is responsible for 14-3-3 binding and cytoplasmic retention (197). The WW domain is 40 amino acids and binds proline-rich peptide motifs ‘PPxY’, which is found in the activation domain of RUNX2 (53) The coiled-coil domain and PDZ-binding domain are transcriptional regulatory regions capable of binding additional proteins (198). The transactivation domain (TAD) assists with RNA polymerase II elongation as part of the preinitiation complex (199). B, The WT protein contains all TAZ domains. TAZ mutants lack the TEAD binding domain (106 Δ), WW domain (Δ WW), and TAD/PDZ binding domain (Δ 304) of TAZ. Figure created by Michael Deel, MD.

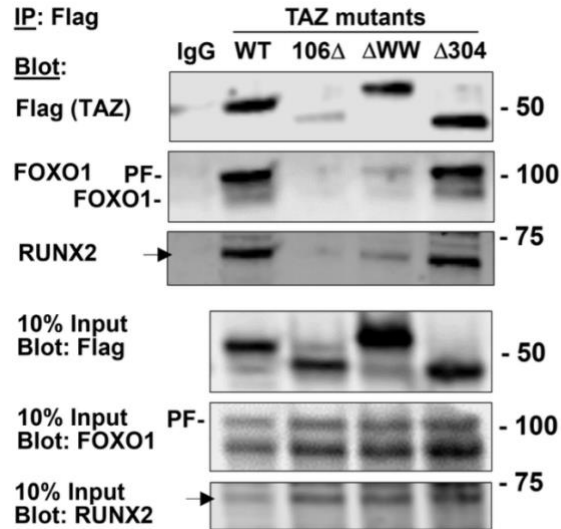


Figure 36: Co-IP for flag-tagged TAZ mutants expressed in Rh4 FP-RMS cells.

IP for TAZ and blot for flag-tagged TAZ, P3F, and RUNX2. The WT protein contains all TAZ domains. TAZ mutants lack the TEAD binding domain (106Δ), WW domain (ΔWW), and TAD/PDZ binding domain (Δ304) of TAZ.

Since P3F and RUNX2 required the same domains to bind TAZ, we performed IP for flag in Rh4 cells endogenously expressing flag-tagged P3F (Figure 37, left) and discovered a faint band for RUNX2 suggesting that P3F and RUNX2 may directly bind in FP-RMS. This finding is aligned with prior publications stating that RUNX2 and P3F are in the same protein interactome (42). Next, when we IP for endogenously expressed TAZ in Rh4 flag-P3F cells, a prominent RUNX2 band is present and no P3F-flag band is present (Figure 37, right), which may be an issue of transfer or because of low protein abundance.

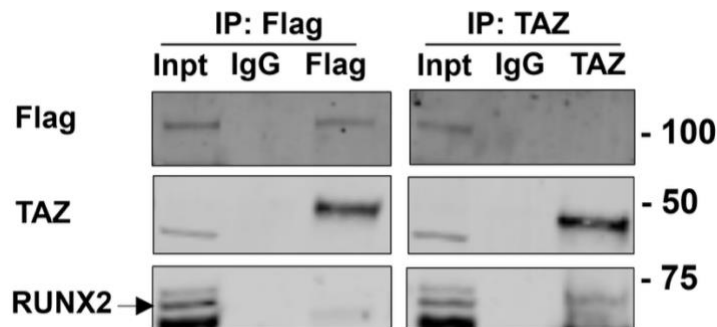


Figure 37: Co-IP for endogenous P3F and TAZ protein in Rh4 cells expressing an endogenous flag-tagged P3F.

Left, IP for endogenous P3F-flag and blot for endogenous P3F-Flag, TAZ, and RUNX2. Right, IP for endogenous TAZ and blot for endogenous P3F-Flag, TAZ, and RUNX2.

To validate whether RUNX2 is directly binding P3F and TAZ, we performed IP coupled with mass spectrometry in Rh4 cells exogenously expressing Flag-P3F and HA-TAZ; IP and immunoblotting for flag and HA concluded that P3F and TAZ bind one another and confirm the expression of each protein (Figure 38). IP-MS confirms results found in Figures 35 and 36; all RUNX proteins, including RUNX2, pulled down with both Flag-P3F and HA-TAZ (Figure 39). RUNX3 is the most abundantly expressed in Flag-P3F and HA-TAZ. This data suggests that all RUNX proteins may be important to P3F and TAZ-P3F associated transcriptional regulation and may all be part of the P3F interactome.

Rh4 cells, Flag-P3F and HA-TAZ

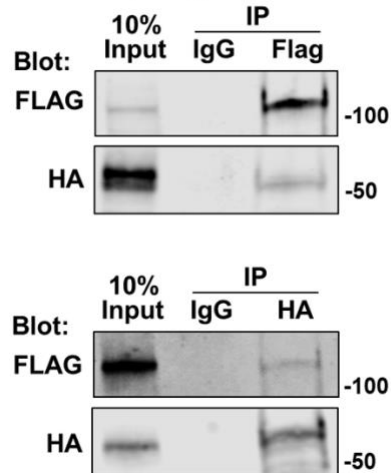


Figure 38: Co-IP for Flag-P3F and HA-TAZ in Rh4 FP-RMS cells.

Top, IP for Flag-P3F and blot for Flag-P3F and HA-TAZ. Bottom, IP for HA-TAZ and blot for Flag-P3F and HA-TAZ.

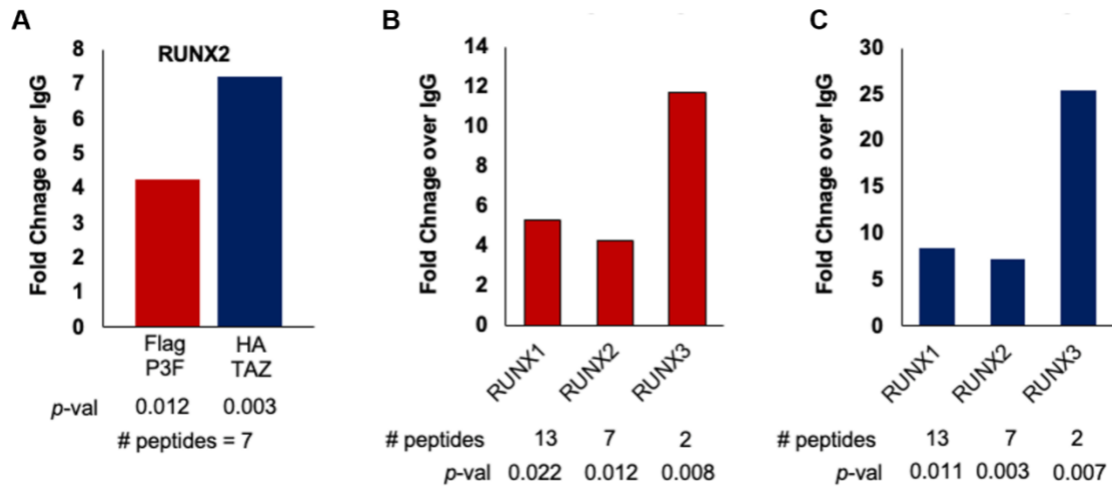


Figure 39: All RUNX proteins bind Flag-P3F, and HA-TAZ expressed in Rh4 FP-RMS cells.

TAZ and P3F bind RUNX1, RUNX2, and RUNX3. A, RUNX2 expression in IP-MS over IgG background for Flag-P3F (red) and HA-TAZ (blue). B, RUNX1, -2, and -3 expression in IP-MS over IgG background. C, RUNX1, -2, and -3 expression in IP-MS for HA-TAZ over IgG background.

4.3.3 *In vitro* and *in vivo* KD of *YAP1* and *WWTR1/TAZ* in FP-RMS cell lines impairs RUNX signaling

Finally, we performed initial epistasis experiments to determine what happens to *RUNX1* and *RUNX2* when Hippo genes, *WWTR1/TAZ* and *YAP* are knocked down in FP-RMS Rh4 and Rh28 cells. When *WWTR1/TAZ* expression was inhibited, *RUNX1* and *RUNX2* expression was decreased in both Rh4 and Rh30 cells (Figure 40). In breast cancer *RUNX1* and *RUNX3* can act as tumor suppressors; for example, when *RUNX1* and *RUNX3* were overexpressed in breast cancer cells, *YAP*-induced mammosphere formation and migration (200). Meanwhile, other reports in cancers such as AML, *RUNX1* is a negative prognostic marker (183). When *YAP* expression was inhibited, *RUNX1* expression decreased in Rh28 cells but not Rh4 cells (Figure 40). Since Rh4 cells and Rh28 cells have different RUNX dependencies (see Chapter 3), perhaps *RUNX1* serves different roles in each or has a different relationship with *YAP*. Additional studies are required to better understand the role of RUNX proteins and their interactions with members of the Hippo pathway.

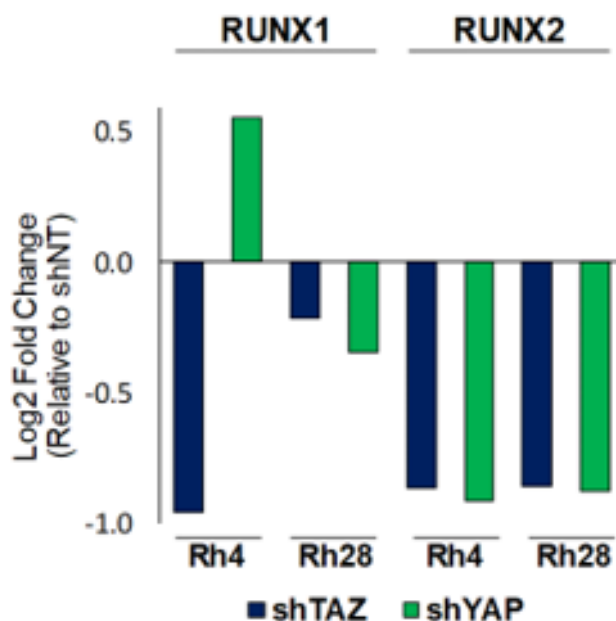


Figure 40: *RUNX1* and *RUNX2* expression is decreased following *WWTR1/TAZ* and *YAP* RNAi knockdown in Rh4 and Rh28 FP-RMS cells.

RNA-seq differential expression data is from Michael Deel, MD. RNA was extracted from Rh4 and Rh28 FP-RMS cells following *WWTR1/TAZ* knockdown (blue) or *YAP* knockdown (green). Log2FC was calculated relative to non-targeting (NT) shRNA.

4.3.4 Discussion

Since RUNX motifs were more accessible in this isogenic myoblast FP-RMS model (Figure 18), we interrogated RUNX2 (Chapter 3) and characterized RUNX/Hippo signaling. We determined that RUNX1, -2 and -3 directly bind TAZ and P3F (Figures 36-39). Since many TAZ, YAP, and TEAD inhibitors have failed (51) despite efforts and knowledge that YAP/TAZ/TEAD mediated transcription is responsible preventing terminal differentiation, increasing proliferation, and preventing apoptosis in FP-RMS (201).

TAZ and RUNX2 are both oncogenic in FP-RMS. To develop better treatments, we can identify proteins that may cooperate with TAZ, such as RUNX2, and small molecules that may synergize with available treatments to targets. It is possible that *RUNX1* and *RUNX2* are directly downstream of YAP/TAZ because *WWTR1/YAP* knockdown resulted in decreased *RUNX1* and *RUNX2* expression (Figure 40). Therefore, RUNX2 small molecule inhibition may further

amplify or extend the effects of YAP/TAZ/TEAD inhibitors. We found that TAZ-RUNX2 binding may require TAZ's TEAD and WW domain, in the future we will determine what domain of RUNX2 is bound by TAZ in FP-RMS; we suspect that the WW domain of TAZ binds the activation domain (PY motif) of RUNX2 with a weak interaction at the C-terminus to stabilize the complex based on reports in other cell lines. Interestingly, RUNX2 binding appeared to be preferential to the TEAD domain and not the WW domain, though this has not been previously reported in other systems (Figure 36).

Mutant overexpression may have amplified results, or the RUNX2-TAZ interaction may be mediated by P3F since RUNX2 and P3F required both the TEAD and WW domains (Figure 36; Figure 37). To investigate this further, IP for endogenous TAZ and found that RUNX2 still blotted (Figure 37). Additionally, RUNX2 was bound to Flag-P3F and HA-TAZ (Figure 38). We conclude that RUNX2, TAZ, and P3F bind each other, but will need to complete additional experiments to identify domain and protein specific interactions. Alternative approaches include using combinations of RUNX2, TAZ, and P3F mutants to identify domain specific interactions. Also, we can perform IP-MS following *WWTR1* or *P3F* knockdown and reevaluate protein-protein relationships.

5. Discussion

In my pursuit of knowledge, I have found that dissertation work generates more scientific questions than it does answers. Here, I will summarize my findings from Chapters 2, 3, and 4 (section 5.1), discuss the implications of this work (Section 5.2), and to discuss possible future directions for this work (Section 5.3).

5.1 Overview

Chapter 2 began with an explanation of the past efforts that the Linardic laboratory has made studying dysregulated Hippo signaling in FP-RMS. This work led to the discovery that PAX3::FOXO1 contributes to FP-RMS in part by dysregulating Hippo signaling. PAX3::FOXO1 results in increased *RASSF4* expression and that RASSF4 binds the C-terminal SARAH domain found in MST1/2 to restrain its tumor suppressor function (54,56). To characterize the downstream effects of MST1/2 inhibition we developed *in vitro* and *in vivo* models and determined that the addition of MST1K59R to human skeletal muscle myoblasts (HSMs) that were engineered to be tumorigenic by expressing PAX3::FOXO1, hTERT, and MYCN resulted in cells that were even more aggressive (Figure 15), and phosphoproteomics identified a string of chromatin modifying proteins that were enriched (Figure 17). These studies inspired us to investigate global changes to chromatin occupancy, further characterize MST1 loss-of-function, and identify potential therapeutic targets. Bulk ATAC-seq of cells expressing PAX3::FOXO1/hTERT/MYCN and MST1K59R revealed a series of RUNX motifs that were enriched (Figure 18).

Keeping RUNX2 in mind, in Chapter 3 we performed mRNA sequencing of primary patient tumor samples and interrogated publicly available databases such as the DepMap and St. Jude's Pecan database to identify FP-RMS vulnerabilities. We found that *RUNX2* expression was increased in patient samples and that RUNX2 was one of two differentially expressed genes that currently have small molecular inhibitors available to them (Figure 19). Despite the availability of

pharmacologic agents to RUNX2 (122,129,130,179), robust literature available on RUNX2 in another fusion-driven pediatric sarcoma, Ewing's sarcoma, and the high dependency of FP-RMS on RUNX2 (Figure 21C), RUNX2 had not been studied in FP-RMS. Using RNAi and the small molecule CADD522, we characterized RUNX2 loss-of-function and FP-RMS *in vitro* and *in vivo* (Figure 23-31). We have corroborated the upregulation of RUNX2 in FP-RMS and other RMS variants and newly identified a feed-forward loop, whereby PAX3::FOXO1 transcriptionally upregulates RUNX2, and RUNX2 supports the expression of PAX3::FOXO1.

In Chapter 4, we expanded our original studies on the Hippo pathway in FP-RMS and RUNX2 in FP-RMS to study protein-protein interactions between RUNX2 and PAX3::FOXO1 and TAZ. In collaboration with Dr. Michael Deel, we performed a series of co-immunoprecipitation experiments and mass spectrometry and found that *RUNX2* knockdown (KD) decreased YAP/TAZ gene signatures as well as *YAPI*, *WWTRI/TAZ*, and *TEAD1* expression (Figure 33; Figure 34), RUNX2 and PAX3::FOXO1 require the TEAD binding and WW domain of TAZ (Figure 36; Figure 37), all RUNX transcription factors bind PAX3::FOXO1 and TAZ, and that *RUNX1* and *RUNX2* may be downstream of YAP and TAZ (Figure 40).

5.2 Implications and future directions

I have stated implications and future directions throughout this text, but summarize additional points in the following sections. An improved understanding of the mechanisms through which PAX3::FOXO1 functions are critical to identifying viable therapeutic targets. For the first time in FP-RMS, we found that it is possible to decrease fusion oncogene/protein expression by genetically and pharmacologically inhibiting an upstream protein (RUNX2). This work is proof-of-concept that indirect methods of inhibiting difficult to drug oncogenes/proteins are achievable. It seems possible that RUNX2 directly targets a *PAX3::FOXO1* enhancer or promoter region, but additional ChIP-seq studies are required to confirm how RUNX2 alters PAX3::FOXO1 gene and protein expression. A study in osteoblasts found that RUNX2 directly

binds an intronic region of FOXO1 that is conserved in the *PAX3::FOXO1* fusion oncogene (202). Additionally, the predominant RUNX2 consensus sequence, 5'TGTGGT3' can be found in the *PAX3::FOXO1* distal super-enhancer (39,47). If we better characterize the mechanisms and possible intermediates linking PAX3::FOXO1 and RUNX2, we may be able to pharmacologically inhibit those in addition to RUNX2. We should investigate fusion-driver expression in addition to fusion-associated gene signatures when studying a FP-RMS target of interest. To better achieve this, we can re-run gene set enrichment analysis on previously generated datasets and identify if other FP-RMS transcriptional targets alter downstream PAX3::FOXO1 signaling globally.

5.2.1 RUNX2 and beyond: pharmacologically targeting the relationships within FP-RMS core regulatory circuitry

This work communicates the importance of RUNX2 in FP-RMS, but additional mechanistic studies are required to transform our understanding of PAX3::FOXO1 and improve FP-RMS treatments. Studying individual targets like RUNX2 allows us to piece together the mechanistic relationships between a single target and the rest of FP-RMS signaling. To better understand this cancer, we must think of individual targets within the context of the PAX3::FOXO1 core regulatory complex (Figure 41, next page). Studies have identified the PAX3::FOXO1 core regulatory circuitry which consists of a list of genes that drive FP-RMS oncogenic signaling. Given the proximity of proteins such as YAP, TAZ, MYOD1, RUNX2, PAX3::FOXO1 and others to one another, it is likely that they coordinate signaling in a co-factor dependent manner. For example, RUNX2, TAZ, and PAX3::FOXO1 may coordinate signaling differently compared to when CDK8 is also present. Additionally, co-factor binding may impact broader signaling and chromatin dynamics such as the spatial patterns of FP-RMS CTCF sites (203).

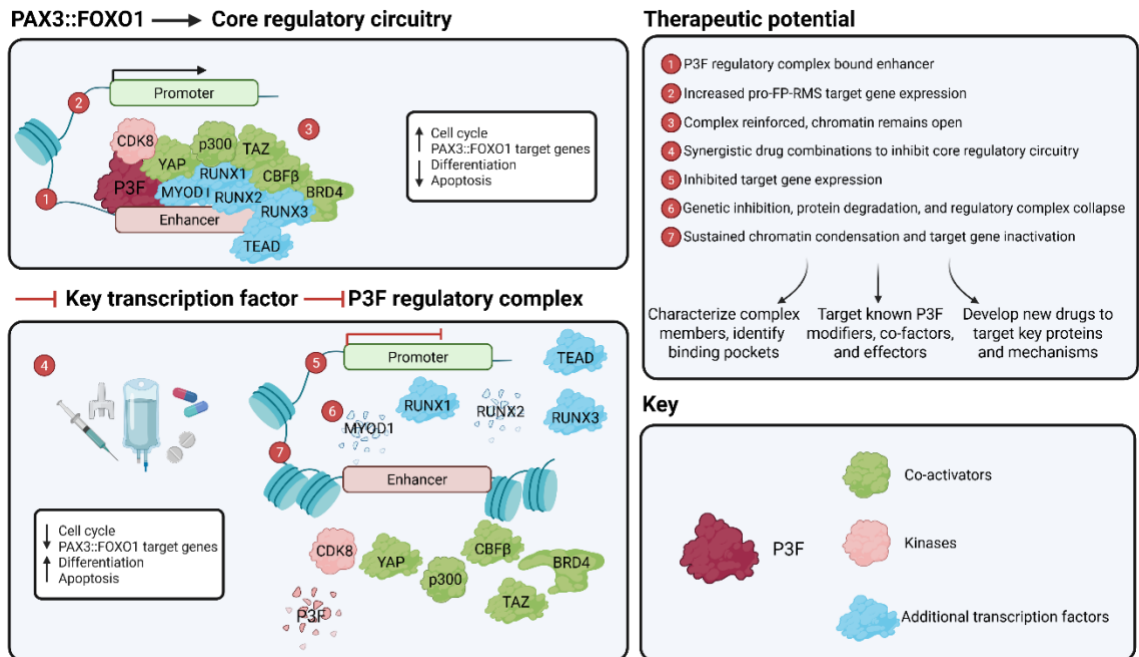


Figure 41: Hypothesized therapeutic potential within the FP-RMS core regulatory circuitry.

PAX3::FOXO1 is not currently druggable due to its intrinsically disordered structure and conferred instability, limited availability of binding pockets, and lack of catalytic/enzymatic activity. Over the past several decades, the RMS field has identified parts of the FP-RMS core regulatory circuitry that sustains pro-FP-RMS signaling and oncogenic phenotypes. Select proteins from this study and prior studies are visualized in panels 1 and 2 (39,42,47). In this work, we have identified transcriptional and protein-protein relationships between the RUNX transcription factors, PAX3::FOXO1, and the Hippo pathway. In the past, many inhibitors of regulatory complex members have failed, including studies with kinase inhibitors such as fascaplysin and BET (BRD4) inhibitors such as JQ1 (204). In the future, therapeutic options may improve by characterizing the P3F core regulatory complex members, using synergistic combinations of drugs to inhibit P3F core regulatory complex members, and by developing new drugs, such as protein degraders, small molecules, and gene therapies, to target P3F core regulatory complex members. Created in BioRender. Mendes, E. (2025) <https://BioRender.com/kggsksv>.

5.2.2 Continued drug discovery

Due to RUNX2's role in mesenchymal stem cell (MSC) differentiation, its importance in pediatric sarcomas such as RMS and Ewing's sarcoma, and potential cancer biomarker, we hope to see additional studies on RUNX2 in other fusion-driven and difficult to treat pediatric cancers such as clear cell sarcoma of soft tissue, synovial sarcoma, and desmoplastic small round cell tumor (DSRCT). With advances in next-generation sequencing (NGS), drug screening, and drug

development, the RMS field is well equipped to identify and develop therapies to FP-RMS drug targets such as RUNX2. For example, because there are limited small molecules available to inhibit RUNX2, I am working to develop a RUNX2 degradation tag (dTAG) system with input from Susu Zhang, PhD, who developed a dTAG-47 construct to degrade PAX3::FOXO1 (42). In addition to expressing the dTAG, I am planning to include an HA tag for IP studies and a HiBit tag that can be used for future high-throughput compound screening (205). Tools such as this designed to RUNX2 and other core regulatory circuit members will allow us to develop novel therapies and differentiate between the effects of genetic inhibition and protein degradation on FP-RMS signaling. Since transcription factors are difficult to drug due to the lack of catalytic activity and often, intrinsically disordered structure, engineering dTAG systems to enable high throughput assays will rapidly increase the FP-RMS potential clinical portfolio. By placing an emphasis on oncogenes implicated in many cancers such as RUNX2, we can more readily translate FP-RMS studies to other subtypes.

Additionally, we need to perform combination studies using RUNX2 inhibitors along with the standard chemotherapy protocol for RMS vincristine, actinomycin D, and an alkylator such as cyclophosphamide or ifosfamide (14,15), and in combination with previously failed monotherapies such as BET inhibitors (204). Identifying synergistic drug combinations as suggested in the Figure 41 legend will better inform future clinical trials.

References

1. Siegel RL, Giaquinto AN, Jemal A. Cancer statistics, 2024. *CA Cancer J Clin* **2024**;74:12–49
2. Rodriguez-Galindo C, Friedrich P, Alcasabas P, Antillon F, Banavali S, Castillo L, *et al.* Toward the Cure of All Children With Cancer Through Collaborative Efforts: Pediatric Oncology As a Global Challenge. *J Clin Oncol* **2015**;33:3065–73
3. SEER*Explorer: An interactive website for SEER cancer statistics. In: Surveillance Research Program NCI, editor, Acute Lymphocytic Leukemia (ALL) SEER 5-Year Relative Survival Rates 2015-20212025.
4. Bhakta N, Force LM, Allemani C, Atun R, Bray F, Coleman MP, *et al.* Childhood cancer burden: a review of global estimates. *Lancet Oncol* **2019**;20:e42–e53
5. Ruymann FB. The development of VAC chemotherapy in rhabdomyosarcoma: what does one do for an encore? *Curr Oncol Rep* **2003**;5:505–9
6. Nagavalli Somasundaram SHC, Richard Quek, Joanne Ngeow. Chapter 43 - Advances in Sarcoma Genomics and Therapeutic Management. In: Franco Dammacco FS, editor. *Oncogenomics*: Academic Press; 2019. p 609–21.
7. Kunisada T, Nakata E, Fujiwara T, Hosono A, Takihira S, Kondo H, *et al.* Soft-tissue sarcoma in adolescents and young adults. *Int J Clin Oncol* **2023**;28:1–11
8. Hettmer S, Linardic CM, Kelsey A, Rudzinski ER, Vokuhl C, Selfe J, *et al.* Molecular testing of rhabdomyosarcoma in clinical trials to improve risk stratification and outcome: A consensus view from European paediatric Soft tissue sarcoma Study Group, Children's Oncology Group and Cooperative Weichteilsarkom-Studiengruppe. *Eur J Cancer* **2022**;172:367–86
9. Linardic CM. PAX3-FOXO1 fusion gene in rhabdomyosarcoma. *Cancer Lett* **2008**;270:10–8
10. Hettmer S, Linardic CM, Kelsey A, Rudzinski ER, Vokuhl C, Selfe J, *et al.* Molecular testing of rhabdomyosarcoma in clinical trials to improve risk stratification and outcome: A consensus view from European paediatric Soft tissue sarcoma Study Group, Children's Oncology Group and Cooperative Weichteilsarkom-Studiengruppe. *Eur J Cancer* **2022**;172:367–86
11. Ognjanovic S, Linabery AM, Charbonneau B, Ross JA. Trends in childhood rhabdomyosarcoma incidence and survival in the United States, 1975-2005. *Cancer* **2009**;115:4218–26

12. Haduong JH, Heske CM, Allen-Rhoades W, Xue W, Teot LA, Rodeberg DA, *et al.* An update on rhabdomyosarcoma risk stratification and the rationale for current and future Children's Oncology Group clinical trials. *Pediatr Blood Cancer* **2022**;69:e29511
13. Heske CM, Chi YY, Venkatramani R, Li M, Arnold MA, Dasgupta R, *et al.* Survival outcomes of patients with localized FOXO1 fusion-positive rhabdomyosarcoma treated on recent clinical trials: A report from the Soft Tissue Sarcoma Committee of the Children's Oncology Group. *Cancer* **2021**;127:946–56
14. Arndt CA, Stoner JA, Hawkins DS, Rodeberg DA, Hayes-Jordan AA, Paidas CN, *et al.* Vincristine, actinomycin, and cyclophosphamide compared with vincristine, actinomycin, and cyclophosphamide alternating with vincristine, topotecan, and cyclophosphamide for intermediate-risk rhabdomyosarcoma: children's oncology group study D9803. *J Clin Oncol* **2009**;27:5182–8
15. Skapek SX, Ferrari A, Gupta AA, Lupo PJ, Butler E, Shipley J, *et al.* Rhabdomyosarcoma. *Nat Rev Dis Primers* **2019**;5:1
16. Agaram NP. Evolving classification of rhabdomyosarcoma. *Histopathology* **2022**;80:98–108
17. Dermawan JK, Malik F, Gross JM, Baraban E, Pratilas C, Mneimneh W, *et al.* Novel PAX3::MAML3 Fusion Identified in Alveolar Rhabdomyosarcoma, Using DNA Methylation Profiling to Expand the Genetic Spectrum of "Fusion-Positive" Cases. *Mod Pathol* **2024**;37:100594
18. Gorunova L, Bjerkehagen B, Micci F, Heim S, Panagopoulos I. Cytogenetic and Molecular Study of an Adult Sclerosing Rhabdomyosarcoma of the Extremity: MYOD1-mutation and Clonal Evolution. *Cancer Genomics Proteomics* **2020**;17:563–9
19. Sankhe CS, Hall L, Kendall GC. Fusion oncogenes in rhabdomyosarcoma: model systems, mechanisms of tumorigenesis, and therapeutic implications. *Front Oncol* **2025**;15:1570070
20. Saoud C, Dermawan JK, Sharma AE, Tap W, Wexler LH, Antonescu CR. Genomic profiling of pleomorphic rhabdomyosarcoma reveals a genomic signature distinct from that of embryonal rhabdomyosarcoma. *Genes Chromosomes Cancer* **2024**;63:e23238
21. Shern JF, Chen L, Chmielecki J, Wei JS, Patidar R, Rosenberg M, *et al.* Comprehensive genomic analysis of rhabdomyosarcoma reveals a landscape of alterations affecting a common genetic axis in fusion-positive and fusion-negative tumors. *Cancer Discov* **2014**;4:216–31

22. Suying Lu JH, Feifei Sun, Juan Wang, Jia Zhu, Yi Que, Mengzhen Li, Zijun Zhen, Yizhuo Zhang. Molecular profiling and prognosis of spindle cell/sclerosing rhabdomyosarcoma: A report from the Chinese PPOG trial. *J Clin Oncol* **2025**;43
23. Freycon C, Lupo PJ, Witkowski L, Budd C, Foulkes WD, Goudie C. A systematic review of the prevalence of pathogenic or likely pathogenic germline variants in individuals with FOXO1 fusion-positive rhabdomyosarcoma. *Pediatr Blood Cancer* **2023**;70:e30651
24. Furlong MA, Fanburg-Smith JC. Pleomorphic rhabdomyosarcoma in children: four cases in the pediatric age group. *Ann Diagn Pathol* **2001**;5:199–206
25. Chen S, Rudzinski ER, Arnold MA. Challenges in the Diagnosis of Pediatric Spindle Cell/Sclerosing Rhabdomyosarcoma. *Surg Pathol Clin* **2020**;13:729–38
26. Li JJ, Kovach AR, DeMonia M, Slemmons KK, Oristian KM, Chen C, *et al.* Expression of oncogenic HRAS in human Rh28 and RMS-YM rhabdomyosarcoma cells leads to oncogene-induced senescence. *Sci Rep* **2021**;11:16505
27. Arnold MA, Anderson JR, Gastier-Foster JM, Barr FG, Skapek SX, Hawkins DS, *et al.* Histology, Fusion Status, and Outcome in Alveolar Rhabdomyosarcoma With Low-Risk Clinical Features: A Report From the Children's Oncology Group. *Pediatr Blood Cancer* **2016**;63:634–9
28. Shern JF, Chen L, Chmielecki J, Wei JS, Patidar R, Rosenberg M, *et al.* Comprehensive genomic analysis of rhabdomyosarcoma reveals a landscape of alterations affecting a common genetic axis in fusion-positive and fusion-negative tumors. *Cancer Discov* **2014**;4:216–31
29. Shern JF, Selfe J, Izquierdo E, Patidar R, Chou HC, Song YK, *et al.* Genomic Classification and Clinical Outcome in Rhabdomyosarcoma: A Report From an International Consortium. *J Clin Oncol* **2021**;39:2859–71
30. Morel VJ, Rossler J, Bernasconi M. Targeted immunotherapy and nanomedicine for rhabdomyosarcoma: The way of the future. *Med Res Rev* **2024**;44:2730–73
31. Pozzo E, Yedigaryan L, Giarratana N, Wang CC, Garrido GM, Degreeef E, *et al.* miR-449a/miR-340 reprogram cell identity and metabolism in fusion-negative rhabdomyosarcoma. *Cell Rep* **2025**;44:115171
32. Gustafson AL, Durbin AD, Artinger KB, Ford HL. Myogenesis gone awry: the role of developmental pathways in rhabdomyosarcoma. *Front Cell Dev Biol* **2024**;12:1521523

33. Shern JF, Selfe J, Izquierdo E, Patidar R, Chou HC, Song YK, *et al.* Genomic Classification and Clinical Outcome in Rhabdomyosarcoma: A Report From an International Consortium. *J Clin Oncol* **2021**;39:2859–71
34. Hernandez KC, Shah AM, Lopez VA, Tagliabracci VS, Chen K, Xu L, *et al.* CD73 contributes to the pathogenesis of fusion-negative rhabdomyosarcoma through the purinergic signaling pathway. *Proc Natl Acad Sci U S A* **2024**;121:e2315925121
35. Hsieh J, Danis EP, Owens CR, Parrish JK, Nowling NL, Wolin AR, *et al.* Dependence of PAX3-FOXO1 chromatin occupancy on ETS1 at important disease-promoting genes exposes new targetable vulnerability in Fusion-Positive Rhabdomyosarcoma. *Oncogene* **2025**;44:19–29
36. Laubscher D, Gryder BE, Sunkel BD, Andresson T, Wachtel M, Das S, *et al.* BAF complexes drive proliferation and block myogenic differentiation in fusion-positive rhabdomyosarcoma. *Nat Commun* **2021**;12:6924
37. Panagopoulos I, Gorunova L, Andersen K, Lund-Iversen M, Tafjord S, Micci F, *et al.* Fusion of the Paired Box 3 (PAX3) and Myocardin (MYOCD) Genes in Pediatric Rhabdomyosarcoma. *Cancer Genomics Proteomics* **2021**;18:723–34
38. Barr FG, Galili N, Holick J, Biegel JA, Rovera G, Emanuel BS. Rearrangement of the PAX3 paired box gene in the paediatric solid tumour alveolar rhabdomyosarcoma. *Nat Genet* **1993**;3:113–7
39. Gryder BE, Yohe ME, Chou HC, Zhang X, Marques J, Wachtel M, *et al.* PAX3-FOXO1 Establishes Myogenic Super Enhancers and Confers BET Bromodomain Vulnerability. *Cancer Discov* **2017**;7:884–99
40. Wachtel M, Schafer BW. PAX3-FOXO1: Zooming in on an "undruggable" target. *Semin Cancer Biol* **2018**;50:115–23
41. Gryder BE, Yohe ME, Chou HC, Zhang X, Marques J, Wachtel M, *et al.* PAX3-FOXO1 Establishes Myogenic Super Enhancers and Confers BET Bromodomain Vulnerability. *Cancer Discov* **2017**;7:884–99
42. Zhang S, Wang J, Liu Q, McDonald WH, Bomber ML, Layden HM, *et al.* PAX3-FOXO1 coordinates enhancer architecture, eRNA transcription, and RNA polymerase pause release at select gene targets. *Mol Cell* **2022**;82:4428–42 e7
43. Ahmed AA, Habeebu S, Farooqi MS, Gamis AS, Gonzalez E, Flatt T, *et al.* MYOD1 as a prognostic indicator in rhabdomyosarcoma. *Pediatr Blood Cancer* **2021**;68:e29085

44. Driman D, Thorner PS, Greenberg ML, Chilton-MacNeill S, Squire J. MYCN gene amplification in rhabdomyosarcoma. *Cancer* **1994**;73:2231–7
45. Pomella S, Cassandri M, D'Archivio L, Porrazzo A, Cossetti C, Phelps D, *et al.* MYOD-SKP2 axis boosts tumorigenesis in fusion negative rhabdomyosarcoma by preventing differentiation through p57(Kip2) targeting. *Nat Commun* **2023**;14:8373
46. Wang W, Du Y, Datta S, Fowler JF, Sang HT, Albadari N, *et al.* Targeting the MYCN-MDM2 pathways for cancer therapy: Are they druggable? *Genes Dis* **2025**;12:101156
47. Gryder BE, Wachtel M, Chang K, El Demerdash O, Aboreden NG, Mohammed W, *et al.* Miswired Enhancer Logic Drives a Cancer of the Muscle Lineage. *iScience* **2020**;23:101103
48. Zhang T, Cooper S, Brockdorff N. The interplay of histone modifications - writers that read. *EMBO Rep* **2015**;16:1467–81
49. Helm BR, Zhan X, Pandya PH, Murray ME, Pollok KE, Renbarger JL, *et al.* Gene Co-Expression Networks Restructured Gene Fusion in Rhabdomyosarcoma Cancers. *Genes (Basel)* **2019**;10
50. Ma S, Meng Z, Chen R, Guan KL. The Hippo Pathway: Biology and Pathophysiology. *Annu Rev Biochem* **2019**;88:577–604
51. Deel MD, Li JJ, Crose LE, Linardic CM. A Review: Molecular Aberrations within Hippo Signaling in Bone and Soft-Tissue Sarcomas. *Front Oncol* **2015**;5:190
52. Chen X, Li Y, Luo J, Hou N. Molecular Mechanism of Hippo-YAP1/TAZ Pathway in Heart Development, Disease, and Regeneration. *Front Physiol* **2020**;11:389
53. Chuang LSH, Ito Y. The Multiple Interactions of RUNX with the Hippo-YAP Pathway. *Cells* **2021**;10
54. Crose LE, Galindo KA, Kephart JG, Chen C, Fitamant J, Bardeesy N, *et al.* Alveolar rhabdomyosarcoma-associated PAX3-FOXO1 promotes tumorigenesis via Hippo pathway suppression. *J Clin Invest* **2014**;124:285–96
55. Kovach AR, Oristian KM, Kirsch DG, Bentley RC, Cheng C, Chen X, *et al.* Identification and targeting of a HES1-YAP1-CDKN1C functional interaction in fusion-negative rhabdomyosarcoma. *Mol Oncol* **2022**;16:3587–605

56. Oristian KM, Crose LES, Kuprasertkul N, Bentley RC, Lin YT, Williams N, *et al.* Loss of MST/Hippo Signaling in a Genetically Engineered Mouse Model of Fusion-Positive Rhabdomyosarcoma Accelerates Tumorigenesis. *Cancer Res* **2018**;78:5513–20
57. Slemmons KK, Crose LE, Rudzinski E, Bentley RC, Linardic CM. Role of the YAP Oncoprotein in Priming Ras-Driven Rhabdomyosarcoma. *PLoS One* **2015**;10:e0140781
58. Slemmons KK, Crose LES, Riedel S, Sushnitha M, Belyea B, Linardic CM. A Novel Notch-YAP Circuit Drives Stemness and Tumorigenesis in Embryonal Rhabdomyosarcoma. *Mol Cancer Res* **2017**;15:1777–91
59. Ito Y. RUNX genes in development and cancer: regulation of viral gene expression and the discovery of RUNX family genes. *Adv Cancer Res* **2008**;99:33–76
60. Mevel R, Draper JE, Lie ALM, Kouskoff V, Lacaud G. RUNX transcription factors: orchestrators of development. *Development* **2019**;146
61. Durst KL, Hiebert SW. Role of RUNX family members in transcriptional repression and gene silencing. *Oncogene* **2004**;23:4220–4
62. Zaret KS, Carroll JS. Pioneer transcription factors: establishing competence for gene expression. *Genes Dev* **2011**;25:2227–41
63. Makita N, Suzuki M, Asami S, Takahata R, Kohzaki D, Kobayashi S, *et al.* Two of four alternatively spliced isoforms of RUNX2 control osteocalcin gene expression in human osteoblast cells. *Gene* **2008**;413:8–17
64. Shen J, She W, Zhang F, Guo J, Jia R. YBX1 Promotes the Inclusion of RUNX2 Alternative Exon 5 in Dental Pulp Stem Cells. *Int J Stem Cells* **2022**;15:301–10
65. Ben-Ami O, Pencovich N, Lotem J, Levanon D, Groner Y. A regulatory interplay between miR-27a and Runx1 during megakaryopoiesis. *Proc Natl Acad Sci U S A* **2009**;106:238–43
66. Lee JW, Park TG, Bae SC. Involvement of RUNX and BRD Family Members in Restriction Point. *Mol Cells* **2019**;42:836–9
67. Komori T. Whole Aspect of Runx2 Functions in Skeletal Development. *Int J Mol Sci* **2022**;23
68. Lin TC. RUNX2 and Cancer. *Int J Mol Sci* **2023**;24

69. Ito Y. RUNX3 is expressed in the epithelium of the gastrointestinal tract. *EMBO Mol Med* **2012**;4:541–2; author reply 3–4
70. Goh YM, Cinghu S, Hong ETH, Lee YS, Kim JH, Jang JW, *et al.* Src kinase phosphorylates RUNX3 at tyrosine residues and localizes the protein in the cytoplasm. *J Biol Chem* **2010**;285:10122–9
71. Zeng L, Wei J, Han D, Liu H, Liu Y, Zhao N, *et al.* Functional analysis of novel RUNX2 mutations in cleidocranial dysplasia. *Mutagenesis* **2017**;32:437–43
72. Newton AH, Pask AJ. Evolution and expansion of the RUNX2 QA repeat corresponds with the emergence of vertebrate complexity. *Commun Biol* **2020**;3:771
73. Lee YF, Nimura K, Lo WN, Saga K, Kaneda Y. Histone H3 lysine 36 methyltransferase Whsc1 promotes the association of Runx2 and p300 in the activation of bone-related genes. *PLoS One* **2014**;9:e106661
74. Leboy P, Grasso-Knight G, D'Angelo M, Volk SW, Lian JV, Drissi H, *et al.* Smad-Runx interactions during chondrocyte maturation. *J Bone Joint Surg Am* **2001**;83-A Suppl 1:S15–22
75. Brusgard JL, Choe M, Chumsri S, Renoud K, MacKerell AD, Jr., Sudol M, *et al.* RUNX2 and TAZ-dependent signaling pathways regulate soluble E-Cadherin levels and tumorsphere formation in breast cancer cells. *Oncotarget* **2015**;6:28132–50
76. Bresciani E, Carrington B, Wincovitch S, Jones M, Gore AV, Weinstein BM, *et al.* CBFbeta and RUNX1 are required at 2 different steps during the development of hematopoietic stem cells in zebrafish. *Blood* **2014**;124:70–8
77. Wu H, Whitfield TW, Gordon JA, Dobson JR, Tai PW, van Wijnen AJ, *et al.* Genomic occupancy of Runx2 with global expression profiling identifies a novel dimension to control of osteoblastogenesis. *Genome Biol* **2014**;15:R52
78. Fritz AJ, Hong D, Boyd J, Kost J, Finstaad KH, Fitzgerald MP, *et al.* RUNX1 and RUNX2 transcription factors function in opposing roles to regulate breast cancer stem cells. *J Cell Physiol* **2020**;235:7261–72
79. Jaruga A, Hordyjewska E, Kandzierski G, Tylzanowski P. Cleidocranial dysplasia and RUNX2-clinical phenotype-genotype correlation. *Clin Genet* **2016**;90:393–402
80. Bruderer M, Richards RG, Alini M, Stoddart MJ. Role and regulation of RUNX2 in osteogenesis. *Eur Cell Mater* **2014**;28:269–86

81. Lee MH, Kim YJ, Yoon WJ, Kim JI, Kim BG, Hwang YS, *et al.* Dlx5 specifically regulates Runx2 type II expression by binding to homeodomain-response elements in the Runx2 distal promoter. *J Biol Chem* **2005**;280:35579–87
82. Huang J, Jia R, Guo J. RUNX2 isoform II protects cancer cells from ferroptosis and apoptosis by promoting PRDX2 expression in oral squamous cell carcinoma. *Elife* **2025**;13
83. Sancisi V, Boretini G, Maramotti S, Ragazzi M, Tamagnini I, Nicoli D, *et al.* Runx2 isoform I controls a panel of proinvasive genes driving aggressiveness of papillary thyroid carcinomas. *J Clin Endocrinol Metab* **2012**;97:E2006–15
84. Komori T. Runx2, a multifunctional transcription factor in skeletal development. *J Cell Biochem* **2002**;87:1–8
85. Komori T. Molecular Mechanism of Runx2-Dependent Bone Development. *Mol Cells* **2020**;43:168–75
86. Schroeder TM, Jensen ED, Westendorf JJ. Runx2: a master organizer of gene transcription in developing and maturing osteoblasts. *Birth Defects Res C Embryo Today* **2005**;75:213–25
87. Munehira Y, Yang Z, Gozani O. Systematic Analysis of Known and Candidate Lysine Demethylases in the Regulation of Myoblast Differentiation. *J Mol Biol* **2017**;429:2055–65
88. Adhami MD, Rashid H, Chen H, Clarke JC, Yang Y, Javed A. Loss of Runx2 in committed osteoblasts impairs postnatal skeletogenesis. *J Bone Miner Res* **2015**;30:71–82
89. Brusgard JL. A Role For RUNX2 And TAZ In Promoting A Tumorigenic Phenotype In Luminal Breast Cancer Cells: University of Maryland, Baltimore; 2014.
90. Hojo H, Saito T, He X, Guo Q, Onodera S, Azuma T, *et al.* Runx2 regulates chromatin accessibility to direct the osteoblast program at neonatal stages. *Cell Rep* **2022**;40:111315
91. Brusgard JL, Passaniti A. RUNX2 Transcriptional Regulation in Development and Disease. In: Kumar R, editor. *Nuclear Signaling Pathways and Targeting Transcription in Cancer*. New York, NY: Springer New York; 2014. p 57–86.
92. Matsuo Y, Qin X, Moriishi T, Kawata-Matsuura VKS, Komori H, Sakane C, *et al.* An Osteoblast-Specific Enhancer and Subenhancer Cooperatively Regulate Runx2 Expression in Chondrocytes. *Int J Mol Sci* **2025**;26

93. Long F, Linsenmayer TF. Regulation of growth region cartilage proliferation and differentiation by perichondrium. *Development* **1998**;125:1067–73
94. Hinoi E, Bialek P, Chen YT, Rached MT, Groner Y, Behringer RR, *et al.* Runx2 inhibits chondrocyte proliferation and hypertrophy through its expression in the perichondrium. *Genes Dev* **2006**;20:2937–42
95. Azarkina K, Gromova E, Malashicheva A. "A Friend Among Strangers" or the Ambiguous Roles of Runx2. *Biomolecules* **2024**;14
96. Gao B, Yang L, Luo ZJ. Transdifferentiation between bone and fat on bone metabolism. *Int J Clin Exp Pathol* **2014**;7:1834–41
97. Qin X, Jiang Q, Nagano K, Moriishi T, Miyazaki T, Komori H, *et al.* Runx2 is essential for the transdifferentiation of chondrocytes into osteoblasts. *PLoS Genet* **2020**;16:e1009169
98. Takarada T, Yoneda Y. Transactivation by Runt related factor-2 of matrix metalloproteinase-13 in astrocytes. *Neurosci Lett* **2009**;451:99–104
99. Korinskaya S, Parameswaran S, Weirauch MT, Barski A. Runx Transcription Factors in T Cells-What Is Beyond Thymic Development? *Front Immunol* **2021**;12:701924
100. Jin YH, Zhang J, Zhu H, Fan GT, Zhou GX. Functions of Exogenous RUNX2 in Giant Cell Tumor of Bone In Vitro. *Orthop Surg* **2020**;12:668–78
101. Yamada D, Fujikawa K, Kawabe K, Furuta T, Nakada M, Takarada T. RUNX2 Promotes Malignant Progression in Glioma. *Neurochem Res* **2018**;43:2047–54
102. Mi J, Wang S, Liu P, Liu C, Zhuang D, Leng X, *et al.* CUL4B Upregulates RUNX2 to Promote the Osteogenic Differentiation of Human Periodontal Ligament Stem Cells by Epigenetically Repressing the Expression of miR-320c and miR-372/373-3p. *Front Cell Dev Biol* **2022**;10:921663
103. Wang Q, Yu W, Huang T, Zhu Y, Huang C. RUNX2 promotes hepatocellular carcinoma cell migration and invasion by upregulating MMP9 expression. *Oncol Rep* **2016**;36:2777–84
104. Khan AS, Campbell KJ, Cameron ER, Blyth K. The RUNX/CBFBeta Complex in Breast Cancer: A Conundrum of Context. *Cells* **2023**;12
105. Akech J, Wixted JJ, Bedard K, van der Deen M, Hussain S, Guise TA, *et al.* Runx2 association with progression of prostate cancer in patients: mechanisms

- mediating bone osteolysis and osteoblastic metastatic lesions. *Oncogene* **2010**;29:811–21
106. Chen X, Wang L, Yang M, Zhao W, Tu J, Liu B, *et al.* RUNX transcription factors: biological functions and implications in cancer. *Clin Exp Med* **2024**;24:50
 107. Cecconi D, Brandi J, Manfredi M, Serena M, Dalle Carbonare L, Deiana M, *et al.* Publisher Correction: Runx2 stimulates neoangiogenesis through the Runt domain in melanoma. *Sci Rep* **2020**;10:2784
 108. Kim LA, D'Amore PA. A brief history of anti-VEGF for the treatment of ocular angiogenesis. *Am J Pathol* **2012**;181:376–9
 109. Bernal C, Otalora A, Canas A, Barreto A, Prieto K, Montecino M, *et al.* Regulatory Role of the RUNX2 Transcription Factor in Lung Cancer Apoptosis. *Int J Cell Biol* **2022**;2022:5198203
 110. Browne G, Nesbitt H, Ming L, Stein GS, Lian JB, McKeown SR, *et al.* Bicalutamide-induced hypoxia potentiates RUNX2-mediated Bcl-2 expression resulting in apoptosis resistance. *Br J Cancer* **2012**;107:1714–21
 111. Nakamura M, Sugimoto H, Ogata T, Hiraoka K, Yoda H, Sang M, *et al.* Improvement of gemcitabine sensitivity of p53-mutated pancreatic cancer MiaPaCa-2 cells by RUNX2 depletion-mediated augmentation of TAp73-dependent cell death. *Oncogenesis* **2016**;5:e233
 112. Sharma JR, Agrawal H, Yadav UCS. Cigarette smoke induces epithelial-to-mesenchymal transition, stemness, and metastasis in lung adenocarcinoma cells via upregulated RUNX-2/galectin-3 pathway. *Life Sci* **2023**;318:121480
 113. Yin X, Teng X, Ma T, Yang T, Zhang J, Huo M, *et al.* RUNX2 recruits the NuRD(MTA1)/CRL4B complex to promote breast cancer progression and bone metastasis. *Cell Death Differ* **2022**;29:2203–17
 114. Zhang L, Liu L, Xu X, He X, Wang G, Fan C, *et al.* miR-205/RunX2 axis negatively regulates CD44(+)/CD24(-) breast cancer stem cell activity. *Am J Cancer Res* **2020**;10:1871–87
 115. Komori T. Regulation of Proliferation, Differentiation and Functions of Osteoblasts by Runx2. *Int J Mol Sci* **2019**;20
 116. Cruz-De la Rosa MI, Jimenez-Wences H, Alarcon-Millan J, Romero-Lopez MJ, Castanon-Sanchez CA, Salmeron-Barcenas EG, *et al.* miR-218-5p/RUNX2 Axis Positively Regulates Proliferation and Is Associated with Poor Prognosis in Cervical Cancer. *Int J Mol Sci* **2022**;23

117. Yuan H, Chen C, Li H, Qu G, Chen L, Liu Y, *et al.* Role of a novel circRNA-CGNL1 in regulating pancreatic cancer progression via NUDT4-HDAC4-RUNX2-GAMT-mediated apoptosis. *Mol Cancer* **2024**;23:27
118. Jing GY, Zheng XZ, Ji XX. lncRNA HAND2-AS1 overexpression inhibits cancer cell proliferation in hepatocellular carcinoma by downregulating RUNX2 expression. *J Clin Lab Anal* **2021**;35:e23717
119. Lv F, Si W, Xu X, He X, Wang Y, Li Y, *et al.* RUNX2 prompts triple negative breast cancer drug resistance through TGF-beta pathway regulating breast cancer stem cells. *Neoplasia* **2024**;48:100967
120. Magar AG, Morya VK, Koh YH, Noh KC. Synergistic HDAC4/8 Inhibition Sensitizes Osteosarcoma to Doxorubicin via pAKT/RUNX2 Pathway Modulation. *Int J Mol Sci* **2025**;26
121. Li XQ, Lu JT, Tan CC, Wang QS, Feng YM. RUNX2 promotes breast cancer bone metastasis by increasing integrin alpha5-mediated colonization. *Cancer Lett* **2016**;380:78–86
122. Green D, Singh A, Tippett VL, Tattersall L, Shah KM, Siachisumo C, *et al.* YBX1-interacting small RNAs and RUNX2 can be blocked in primary bone cancer using CADD522. *J Bone Oncol* **2023**;39:100474
123. Li R, Lin Y, Hu F, Liao Y, Tang J, Shen Y, *et al.* LncRNA TEX41 regulates autophagy by increasing Runx2 expression in lung adenocarcinoma bone metastasis. *Am J Transl Res* **2023**;15:949–66
124. Panagopoulos I, Gorunova L, Lobmaier I, Andersen K, Kostolomov I, Lund-Iversen M, *et al.* FOS-ANKH and FOS-RUNX2 Fusion Genes in Osteoblastoma. *Cancer Genomics Proteomics* **2020**;17:161–8
125. Bishop JA, Nakaguro M, Weinreb I, Palsgrove D, Rooper LM, Vandergriff TW, *et al.* Comprehensive Next Generation Sequencing Reveals that Purported Primary Squamous Cell Carcinomas of the Parotid Gland are Genetically Heterogeneous. *Head Neck Pathol* **2024**;18:106
126. Li X, McGee-Lawrence ME, Decker M, Westendorf JJ. The Ewing's sarcoma fusion protein, EWS-FLI, binds Runx2 and blocks osteoblast differentiation. *J Cell Biochem* **2010**;111:933–43
127. Illendula A, Gilmour J, Grembecka J, Tirumala VSS, Boulton A, Kuntimaddi A, *et al.* Small Molecule Inhibitor of CBFbeta-RUNX Binding for RUNX Transcription Factor Driven Cancers. *EBioMedicine* **2016**;8:117–31

128. Green D, Mohorianu I, McNamara I, Dalmay T, Fraser WD. miR-16 is highly expressed in Paget's associated osteosarcoma. *Endocr Relat Cancer* **2017**;24:L27–L31
129. Kim MS, Gernapudi R, Cedeno YC, Polster BM, Martinez R, Shapiro P, *et al.* Targeting breast cancer metabolism with a novel inhibitor of mitochondrial ATP synthesis. *Oncotarget* **2020**;11:3863–85
130. Kim MS, Gernapudi R, Choi EY, Lapidus RG, Passaniti A. Characterization of CADD522, a small molecule that inhibits RUNX2-DNA binding and exhibits antitumor activity. *Oncotarget* **2017**;8:70916–40
131. Underwood KF, D'Souza DR, Mochin-Peters M, Pierce AD, Kommineni S, Choe M, *et al.* Regulation of RUNX2 transcription factor-DNA interactions and cell proliferation by vitamin D3 (cholecalciferol) prohormone activity. *J Bone Miner Res* **2012**;27:913–25
132. Underwood KF, Mochin MT, Brusgard JL, Choe M, Gnatt A, Passaniti A. A quantitative assay to study protein:DNA interactions, discover transcriptional regulators of gene expression, and identify novel anti-tumor agents. *J Vis Exp* **2013**
133. Deng Y, Wu A, Li P, Li G, Qin L, Song H, *et al.* Yap1 Regulates Multiple Steps of Chondrocyte Differentiation during Skeletal Development and Bone Repair. *Cell Rep* **2016**;14:2224–37
134. Passaniti A, Brusgard JL, Qiao Y, Sudol M, Finch-Edmondson M. Roles of RUNX in Hippo Pathway Signaling. *Adv Exp Med Biol* **2017**;962:435–48
135. Byun MR, Kim AR, Hwang JH, Sung MK, Lee YK, Hwang BS, *et al.* Phorbaketal A stimulates osteoblast differentiation through TAZ mediated Runx2 activation. *FEBS Lett* **2012**;586:1086–92
136. Guo Z, Zhou K, Wang Q, Huang Y, Ji J, Peng Y, *et al.* The transcription factor RUNX2 fuels YAP1 signaling and gastric cancer tumorigenesis. *Cancer Sci* **2021**;112:3533–44
137. Matsumoto Y, La Rose J, Kent OA, Wagner MJ, Narimatsu M, Levy AD, *et al.* Reciprocal stabilization of ABL and TAZ regulates osteoblastogenesis through transcription factor RUNX2. *J Clin Invest* **2016**;126:4482–96
138. Won GW, Sung M, Lee Y, Lee YH. MST2 kinase regulates osteoblast differentiation by phosphorylating and inhibiting Runx2 in C2C12 cells. *Biochem Biophys Res Commun* **2019**;512:591–7

139. Zhu Y, Wu Y, Cheng J, Wang Q, Li Z, Wang Y, *et al.* Pharmacological activation of TAZ enhances osteogenic differentiation and bone formation of adipose-derived stem cells. *Stem Cell Res Ther* **2018**;9:53
140. van der Weyden L, Papaspyropoulos A, Poulogiannis G, Rust AG, Rashid M, Adams DJ, *et al.* Loss of RASSF1A synergizes with deregulated RUNX2 signaling in tumorigenesis. *Cancer Res* **2012**;72:3817–27
141. Ying J, Wang P, Zhang S, Xu T, Zhang L, Dong R, *et al.* Transforming growth factor-beta1 promotes articular cartilage repair through canonical Smad and Hippo pathways in bone mesenchymal stem cells. *Life Sci* **2018**;192:84–90
142. Basu-Roy U, Bayin NS, Rattanakorn K, Han E, Placantonakis DG, Mansukhani A, *et al.* Sox2 antagonizes the Hippo pathway to maintain stemness in cancer cells. *Nat Commun* **2015**;6:6411
143. Laubscher D, Gryder BE, Sunkel BD, Andresson T, Wachtel M, Das S, *et al.* BAF complexes drive proliferation and block myogenic differentiation in fusion-positive rhabdomyosarcoma. *Nat Commun* **2021**;12:6924
144. Naini S, Etheridge KT, Adam SJ, Qualman SJ, Bentley RC, Counter CM, *et al.* Defining the cooperative genetic changes that temporally drive alveolar rhabdomyosarcoma. *Cancer Res* **2008**;68:9583–8
145. Ura S, Masuyama N, Graves JD, Gotoh Y. Caspase cleavage of MST1 promotes nuclear translocation and chromatin condensation. *Proc Natl Acad Sci U S A* **2001**;98:10148–53
146. Bohm M, Wachtel M, Marques JG, Streiff N, Laubscher D, Nanni P, *et al.* Helicase CHD4 is an epigenetic coregulator of PAX3-FOXO1 in alveolar rhabdomyosarcoma. *J Clin Invest* **2016**;126:4237–49
147. Linardic CM, Downie DL, Qualman S, Bentley RC, Counter CM. Genetic modeling of human rhabdomyosarcoma. *Cancer Res* **2005**;65:4490–5
148. Slemmons KK, Deel MD, Lin YT, Oristian KM, Kuprasertkul N, Genadry KC, *et al.* A method to culture human alveolar rhabdomyosarcoma cell lines as rhabdospheres demonstrates an enrichment in stemness and Notch signaling. *Biol Open* **2021**;10
149. Wei X, Xiang Y, Peters DT, Marius C, Sun T, Shan R, *et al.* HiCAR is a robust and sensitive method to analyze open-chromatin-associated genome organization. *Mol Cell* **2022**;82:1225–38 e6

150. Praskova M, Khoklatchev A, Ortiz-Vega S, Avruch J. Regulation of the MST1 kinase by autophosphorylation, by the growth inhibitory proteins, RASSF1 and NORE1, and by Ras. *Biochem J* **2004**;381:453–62
151. Sengupta S, Prabha H, Levy DL. How the chromatin landscape influences nuclear morphology. *Front Cell Dev Biol* **2025**;13:1634252
152. Yan F, Powell DR, Curtis DJ, Wong NC. From reads to insight: a hitchhiker's guide to ATAC-seq data analysis. *Genome Biol* **2020**;21:22
153. The Gene Ontology C. Expansion of the Gene Ontology knowledgebase and resources. *Nucleic Acids Res* **2017**;45:D331–D8
154. Illendula A, Gilmour J, Grembecka J, Tirumala VSS, Boulton A, Kuntimaddi A, *et al.* Small Molecule Inhibitor of CBFbeta-RUNX Binding for RUNX Transcription Factor Driven Cancers. *EBioMedicine* **2016**;8:117–31
155. Chen C, Dorado Garcia H, Scheer M, Henssen AG. Current and Future Treatment Strategies for Rhabdomyosarcoma. *Front Oncol* **2019**;9:1458
156. Pomella S, Cassandri M, D'Archivio L, Porrazzo A, Cossetti C, Phelps D, *et al.* MYOD-SKP2 axis boosts tumorigenesis in fusion negative rhabdomyosarcoma by preventing differentiation through p57(Kip2) targeting. *Nat Commun* **2023**;14:8373
157. Pertea M, Kim D, Pertea GM, Leek JT, Salzberg SL. Transcript-level expression analysis of RNA-seq experiments with HISAT, StringTie and Ballgown. *Nat Protoc* **2016**;11:1650–67
158. Bray NL, Pimentel H, Melsted P, Pachter L. Near-optimal probabilistic RNA-seq quantification. *Nat Biotechnol* **2016**;34:525–7
159. Green D, Eyre H, Singh A, Taylor JT, Chu J, Jeys L, *et al.* Targeting the MAPK7/MMP9 axis for metastasis in primary bone cancer. *Oncogene* **2020**;39:5553–69
160. Love MI, Huber W, Anders S. Moderated estimation of fold change and dispersion for RNA-seq data with DESeq2. *Genome Biol* **2014**;15:550
161. Singh A, Mohorianu I, Green D, Dalmay T, Dasgupta I, Mukherjee SK. Artificially induced phased siRNAs promote virus resistance in transgenic plants. *Virology* **2019**;537:208–15

162. Tattersall L, Shah KM, Lath DL, Singh A, Down JM, De Marchi E, *et al.* The P2RX7B splice variant modulates osteosarcoma cell behaviour and metastatic properties. *J Bone Oncol* **2021**;31:100398
163. Prufer K, Stenzel U, Dannemann M, Green RE, Lachmann M, Kelso J. PatMaN: rapid alignment of short sequences to large databases. *Bioinformatics* **2008**;24:1530–1
164. Kozomara A, Griffiths-Jones S. miRBase: annotating high confidence microRNAs using deep sequencing data. *Nucleic Acids Res* **2014**;42:D68–73
165. Billmeier M, Green D, Hall AE, Turnbull C, Singh A, Xu P, *et al.* Mechanistic insights into non-coding Y RNA processing. *RNA Biol* **2022**;19:468–80
166. Ghibaudi M, Boido M, Green D, Signorino E, Berto GE, Pourshayesteh S, *et al.* miR-7b-3p Exerts a Dual Role After Spinal Cord Injury, by Supporting Plasticity and Neuroprotection at Cortical Level. *Front Mol Biosci* **2021**;8:618869
167. Green D, Singh A, Sanghera J, Jeys L, Sumathi V, Dalmay T, *et al.* Maternally expressed, paternally imprinted, embryonic non-coding RNA are expressed in osteosarcoma, Ewing sarcoma and spindle cell sarcoma. *Pathology* **2019**;51:113–6
168. Shaw B, Burrell CL, Green D, Navarro-Martinez A, Scott D, Daroszewska A, *et al.* Molecular insights into an ancient form of Paget's disease of bone. *Proc Natl Acad Sci U S A* **2019**;116:10463–72
169. Ritchie ME, Phipson B, Wu D, Hu Y, Law CW, Shi W, *et al.* limma powers differential expression analyses for RNA-sequencing and microarray studies. *Nucleic Acids Res* **2015**;43:e47
170. Hanahan D. Hallmarks of Cancer: New Dimensions. *Cancer Discov* **2022**;12:31–46
171. Tanzarella S, Lionello I, Valentini B, Russo V, Lollini PL, Traversari C. Rhabdomyosarcomas are potential target of MAGE-specific immunotherapies. *Cancer Immunol Immunother* **2004**;53:519–24
172. Hwang GH, Pazyra-Murphy MF, Seo HS, Dhe-Paganon S, Stopka SA, DiPiazza M, *et al.* A Benzarone Derivative Inhibits EYA to Suppress Tumor Growth in SHH Medulloblastoma. *Cancer Res* **2024**;84:872–86
173. Hsu JY, Danis EP, Nance S, O'Brien JH, Gustafson AL, Wessells VM, *et al.* SIX1 reprograms myogenic transcription factors to maintain the rhabdomyosarcoma undifferentiated state. *Cell Rep* **2022**;38:110323

174. Martin JW, Zielenska M, Stein GS, van Wijnen AJ, Squire JA. The Role of RUNX2 in Osteosarcoma Oncogenesis. *Sarcoma* **2011**;2011:282745
175. Depmap B. DepMap23Q4 Public. Figshare+.Dataset. ed2023.
176. Wei Y, Qin Q, Yan C, Hayes MN, Garcia SP, Xi H, *et al.* Single-cell analysis and functional characterization uncover the stem cell hierarchies and developmental origins of rhabdomyosarcoma. *Nat Cancer* **2022**;3:961–75
177. Liao GB, Li XZ, Zeng S, Liu C, Yang SM, Yang L, *et al.* Regulation of the master regulator FOXM1 in cancer. *Cell Commun Signal* **2018**;16:57
178. Kuda M, Kohashi K, Yamada Y, Maekawa A, Kinoshita Y, Nakatsura T, *et al.* FOXM1 expression in rhabdomyosarcoma: a novel prognostic factor and therapeutic target. *Tumour Biol* **2016**;37:5213–23
179. Bull EC, Singh A, Harden AM, Soanes K, Habash H, Toracchio L, *et al.* Targeting metastasis in paediatric bone sarcomas. *Mol Cancer* **2025**;24:153
180. Zhang Y, Xie RL, Croce CM, Stein JL, Lian JB, van Wijnen AJ, *et al.* A program of microRNAs controls osteogenic lineage progression by targeting transcription factor Runx2. *Proc Natl Acad Sci U S A* **2011**;108:9863–8
181. Ebauer M, Wachtel M, Niggli FK, Schafer BW. Comparative expression profiling identifies an in vivo target gene signature with TFAP2B as a mediator of the survival function of PAX3/FKHR. *Oncogene* **2007**;26:7267–81
182. Nomura K, Kimira Y, Osawa Y, Kataoka-Matsushita A, Takao K, Sugita Y, *et al.* Stimulation of the Runx2 P1 promoter by collagen-derived dipeptide prolyl-hydroxyproline bound to Foxg1 and Foxo1 in osteoblasts. *Biosci Rep* **2021**;41
183. Tuo Z, Zhang Y, Wang X, Dai S, Liu K, Xia D, *et al.* RUNX1 is a promising prognostic biomarker and related to immune infiltrates of cancer-associated fibroblasts in human cancers. *BMC Cancer* **2022**;22:523
184. Sood R, Kamikubo Y, Liu P. Role of RUNX1 in hematological malignancies. *Blood* **2017**;129:2070–82
185. Kubota S, Tokunaga K, Umezu T, Yokomizo-Nakano T, Sun Y, Oshima M, *et al.* Lineage-specific RUNX2 super-enhancer activates MYC and promotes the development of blastic plasmacytoid dendritic cell neoplasm. *Nat Commun* **2019**;10:1653
186. Sustic T, Bosdriesz E, van Wageningen S, Wessels LFA, Bernards R. RUNX2/CBFB modulates the response to MEK inhibitors through activation of

- receptor tyrosine kinases in KRAS-mutant colorectal cancer. *Transl Oncol* **2020**;13:201–11
187. Trust BCR. 2023 Revolutionary new bone cancer drug identified. Accessed 2025.
188. Alegre F, Ormonde AR, Godinez DR, Illendula A, Bushweller JH, Wittenburg LA. The interaction between RUNX2 and core binding factor beta as a potential therapeutic target in canine osteosarcoma. *Vet Comp Oncol* **2020**;18:52–63
189. Gayatri MB, Kancha RK, Behera A, Patchva D, Velugonda N, Gundeti S, *et al.* AMPK-induced novel phosphorylation of RUNX1 inhibits STAT3 activation and overcome imatinib resistance in chronic myelogenous leukemia (CML) subjects. *Cell Death Discov* **2023**;9:401
190. Institute N. 2024 Clinical trial researching therapy for RUNX1 mutations. Accessed 2025.
191. Tuddenham L, Wheeler G, Ntounia-Fousara S, Waters J, Hajihosseini MK, Clark I, *et al.* The cartilage specific microRNA-140 targets histone deacetylase 4 in mouse cells. *FEBS Lett* **2006**;580:4214–7
192. Greither T, Koser F, Holzhausen HJ, Guttler A, Wurl P, Kappler M, *et al.* MiR-155-5p and MiR-203a-3p Are Prognostic Factors in Soft Tissue Sarcoma. *Cancers (Basel)* **2020**;12
193. Hinson AR, Jones R, Crose LE, Belyea BC, Barr FG, Linardic CM. Human rhabdomyosarcoma cell lines for rhabdomyosarcoma research: utility and pitfalls. *Front Oncol* **2013**;3:183
194. Huang L, Yuan W, Li X, Liu Y, Wan R, Ma X, *et al.* CDK4/6-mediated phosphorylation of DUB3 promotes YAP1 stability and hepatocellular carcinoma progression. *Cell Death Discov* **2025**;11:212
195. Zanconato F, Battilana G, Forcato M, Filippi L, Azzolin L, Manfrin A, *et al.* Transcriptional addiction in cancer cells is mediated by YAP/TAZ through BRD4. *Nat Med* **2018**;24:1599–610
196. Paradise CR, Galvan ML, Kubrova E, Bowden S, Liu E, Carstens MF, *et al.* The epigenetic reader Brd4 is required for osteoblast differentiation. *J Cell Physiol* **2020**;235:5293–304
197. Chen YA, Lu CY, Cheng TY, Pan SH, Chen HF, Chang NS. WW Domain-Containing Proteins YAP and TAZ in the Hippo Pathway as Key Regulators in Stemness Maintenance, Tissue Homeostasis, and Tumorigenesis. *Front Oncol* **2019**;9:60

198. Jeong MG, Kim HK, Hwang ES. The essential role of TAZ in normal tissue homeostasis. *Arch Pharm Res* **2021**;44:253–62
199. Yu M, Wang J, Zhang X, Zhang H, Li C, Li J, *et al.* The mechanism of YAP/TAZ transactivation and dual targeting for cancer therapy. *Nat Commun* **2025**;16:3855
200. Kulkarni M, Tan TZ, Syed Sulaiman NB, Lamar JM, Bansal P, Cui J, *et al.* RUNX1 and RUNX3 protect against YAP-mediated EMT, stem-ness and shorter survival outcomes in breast cancer. *Oncotarget* **2018**;9:14175–92
201. Deel MD, Slemmons KK, Hinson AR, Genadry KC, Burgess BA, Crose LES, *et al.* The Transcriptional Coactivator TAZ Is a Potent Mediator of Alveolar Rhabdomyosarcoma Tumorigenesis. *Clin Cancer Res* **2018**;24:2616–30
202. Hakelien AM, Bryne JC, Harstad KG, Lorenz S, Paulsen J, Sun J, *et al.* The regulatory landscape of osteogenic differentiation. *Stem Cells* **2014**;32:2780–93
203. Nanni L, Ceri S, Logie C. Spatial patterns of CTCF sites define the anatomy of TADs and their boundaries. *Genome Biol* **2020**;21:197
204. Nguyen TH, Barr FG. Therapeutic Approaches Targeting PAX3-FOXO1 and Its Regulatory and Transcriptional Pathways in Rhabdomyosarcoma. *Molecules* **2018**;23
205. Riching KM, Mahan SD, Urh M, Daniels DL. High-Throughput Cellular Profiling of Targeted Protein Degradation Compounds using HiBiT CRISPR Cell Lines. *J Vis Exp* **2020**

Biography

Elizabeth was born and raised in Connecticut and completed her undergraduate studies at the University of Evansville in 2017. She majored in biology and received a minor in archaeology. Early in her research career, she participated in wildlife biology research with mentors Cris Hochwender, PhD and Noah Gordon, PhD. After college she worked as a middle school math and science teacher before completing a Master's degree in biomolecular sciences at Central Connecticut State University. She worked in the laboratory of Daniel Chase, PhD studying dopamine signaling and then completed a fellowship at the University of Connecticut School of Medicine in the laboratory of Caroline Dealy, PhD, studying epidermal growth factor signaling in rheumatoid arthritis. Outside of research, Elizabeth has been involved in science communication since 2018 (@elizabeththescientist), and she frequently mentors individuals interested in applying to graduate school and does public speaking and community outreach to get others interested in science. In July 2020, she began her doctoral research with the umbrella program in Department of Cellular and Molecular Biology before joining the Department of Pharmacology and Cancer Biology at Duke University School of Medicine. During her doctoral training, Elizabeth worked in the laboratory of Corinne M. Linardic, MD PhD, whose primary appointment is with the Department of Pediatrics-Hematology/Oncology at Duke Children's Hospital and Health Center. She received a certificate in Cellular and Molecular Biology and her Doctor of Philosophy from the Department of Pharmacology and Cancer Biology in September 2025.

While at Duke University School of Medicine, Elizabeth was a member of the Duke Bioscience Collaborative for Research Engagement, the Society for the Advancement of Chicanos/Hispanics and Native Americans in Science, the Duke Scholars in Oncology and Regenerative Medicine Program, the Duke Cellular and Molecular Biology and Pharmacology and Cancer Biology recruitment committees, and the Duke Pharmacology and Cancer Biology

Diversity, Equity, and Inclusion committee. She was a neuropharmacology teaching assistant and worked alongside Cynthia Kuhn, PhD.

Elizabeth was awarded a travel award as a member of the Duke Bioscience Collaborative for Research Engagement, a Precision Genomics Collaboratory Pilot Grant from the Office of Biomedical Graduate Education at Duke University School of Medicine, appointed to the Duke Cellular and Molecular Biology NIH T32 Training Grant (5T32GM142605-03) from August 2021 to August 2023, and appointed as a trainee member of the NCI/NIH FusOnC2 group. Her work was further supported by an NCI/NIH U54 grant (1U54CA231630) that was awarded to Corinne M. Linardic, MD PhD.

She completed an internship at Eli Lilly in research and development in the Department of Cardiometabolic Health and received two awards, an Eli Lilly Inspire award, and an Eli Lilly Innovate Award. As a public speaker, Elizabeth has given multiple keynote speeches and meeting presentations at domestic and international events and conferences.

Elizabeth has contributed and helped publish several academic manuscripts which can be found at <https://orcid.org/0000-0003-1296-7879>.